MUPETS

A Multi-Regime Plasma Equilibrium Transport Solver for Predicting Ambipolar Plasma Thruster Behaviour and Performance

Master of Science Thesis

Willem van Lynden

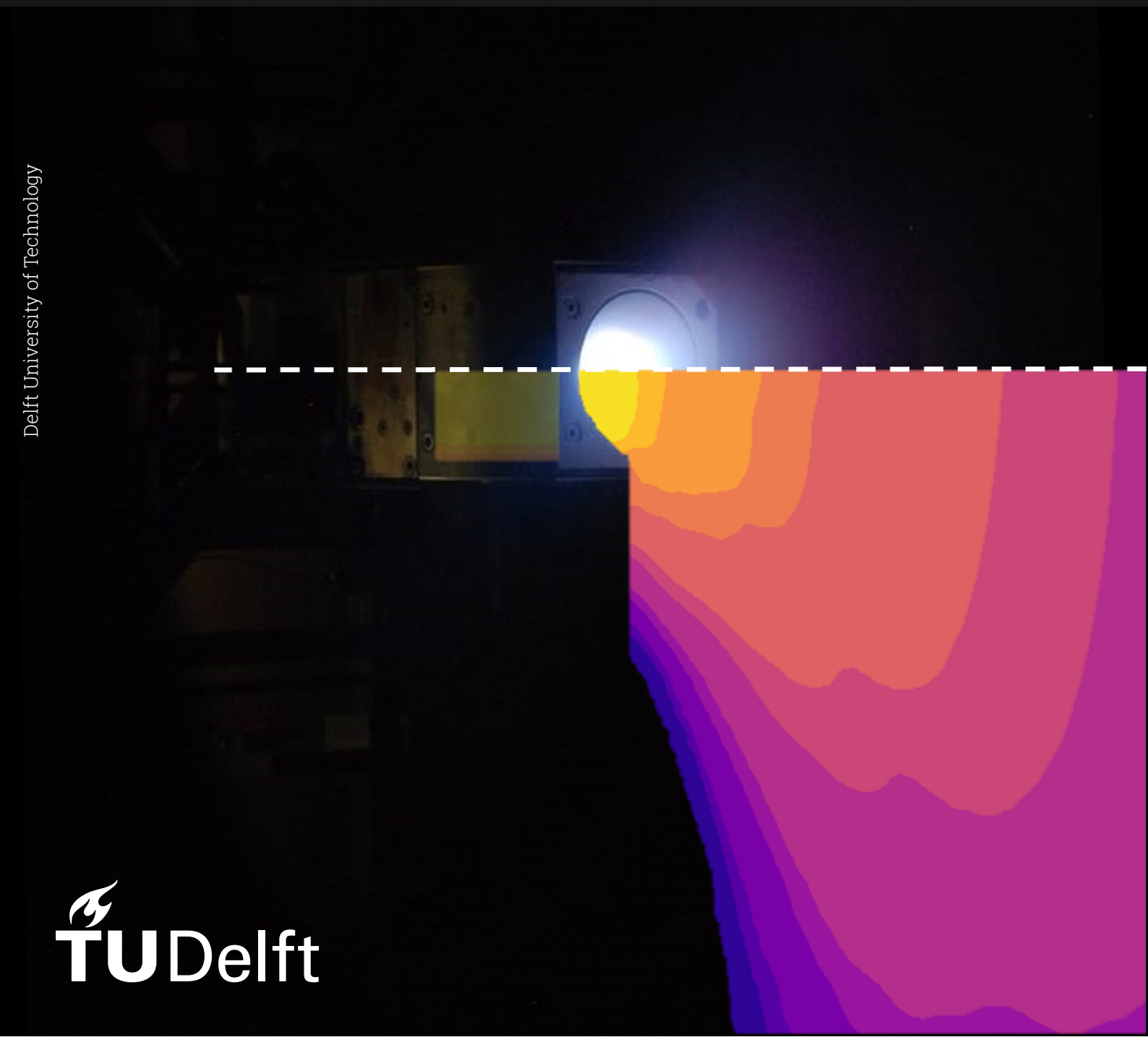

Delft University of Technology

TU Delft

MUPETS

A Multi-Regime Plasma Equilibrium Transport Solver for Predicting Ambipolar Plasma Thruster Behaviour and Performance

by

Willem van Lynden

to obtain the degree of Master of Science

at the Delft University of Technology,

to be defended publicly on Tuesday December 12, 2023 at 10:00 AM.

Student number:	4534344	
Project duration:	March 9, 2023 – Nov 28, 2023	
Thesis committee:	Dr. A. Cervone,	TU Delft, supervisor
	ir. B. Zandbergen,	TU Delft, chair
	ir. M. Naeije,	TU Delft, examiner
	Prof. F. Ponti,	University of Bologna, co-supervisor

Cover:	Laboratory ambipolar thruster and its modeled plasma density profile
Style:	TU Delft Report Style, with modifications by Daan Zwaneveld

An electronic version of this thesis is available at http://repository.tudelft.nl/.
Research data and resources of this thesis are available from the author via wvlynden@gmail.com

TU Delft

Abstract

This study addresses the challenge of accurately modeling the multi-regime plasma flow through Ambipolar Plasma Thrusters (APTs), a type of Electric Propulsion (EP) system. Despite their advantages, understanding the behavior of plasma within APTs is complex due to the presence of two different flow regimes: the fluid regime inside the thruster's source chamber and the kinetic regime inside the thruster's magnetic nozzle. To enhance the precision of APT modeling, this thesis introduces a novel coupling methodology between fluidic and kinetic solvers, resulting in the MUlti-regime Plasma Equilibrium Transport Solver (MUPETS).

MUPETS employs two models, the continuum OpenFOAM code for the fluidic regime and the Particle-in-Cell (PIC) Starfish code for the kinetic regime, coupled through a closed-loop iterative coupling scheme. This approach allows for a self-consistent prediction of plasma transport within the entire thruster domain, including the interface between the numerical domains of each model. At this interface, which often coincides with the thruster outlet, the model's iterative loop self-corrects the interfacing boundary conditions of each numerical domain, removing imposed boundary conditions such as assumed velocities. This has reduced plasma species discontinuities across the models' interface to less than 4% for electrons and less than 1% for ions. The performance of MUPETS was validated against experimental measures from a laboratory thruster at the University of Padova, showing less than a 19% difference in predicted propulsive performance.

The MUPETS code requires minimal alteration of the separate solvers, allowing for the fluid or kinetic solvers to be swapped out with higher-fidelity models or numerically better performing models as required. This flexibility enables the comparison of previously developed and validated models from literature to investigate their suitability for describing the plasma flow across the regime change. The study concludes that the developed coupling method presents an improvement to the state of multi-regime plasma flow modeling while providing similar accuracy when used for predicting the propulsive performance of APTs.

Preface

Before you lies my thesis report which explores the subjects of electric propulsion and plasma modeling. As the research done on electric propulsion at the Delft University of Technology is limited, I conducted much of my work at the universities of Bologna and Padova in Italy. Thanks to this my thesis was a tremendous adventure and experience, and enabled me to finally enter the field of electric propulsion, which I had been wanting to do for years.

I was incredibly lucky to have multiple thesis supervisors, on each of whom I could count on. I am grateful for the trust of my TU Delft supervisor Angelo Cervone, without which I would have never been able to do my thesis work abroad or chase an EP subject. Even though I was not working in Delft, he would be the first to answer and provide what I needed whenever I had questions for him. My Bologna supervisors Fabrizo Ponti and Nabil Souhair have my sincere thanks for giving me the opportunity to come work with them in the Alma Propulsion Laboratory and their general hospitality. Their trust in my work allowed me to present a paper on it at the IAC, and this thrust motivated me to continue further in research. Raoul Andriulli added to this not only his PIC expertise, but also his viewpoint as a PhD student just starting out, which gave me much insight for the next years to come. And from Padova, Mirko Magarotto gave me a reassuring expert insight into the concrete field of electric propulsion, it's modeling, and related academia, whenever I (frequently) questioned my own approach or results.

Besides these people directly involved with my thesis, I would like to thank everyone of the Stratos IV team and the DARE student society. The experiences I gathered in DARE are some of the greatest of my life and they have also proven invaluable to this thesis. I also thank all my friends who simply provided opportunities to have a short break once in a while to remain sane.

And last but certainly not least, I want to thank my family, who were okay with me going to a library to finish my literature study almost every day while we were on holiday. My brother and sister, facing the exact same challenges and fun as students, have both been a great support and point of reference regarding developments in life. And I want to thank my parents for sparking and supporting my motivation in life, and being so interested in it themselves that I can excitedly talk to them knowing that they do understand substantial parts of it, even to the degree that they enthusiastically would proofread my ramblings to help me make them make sense.

Finally, I would like to thank my grandfather, Willem. While he passed away when I started this work, his kindness and hardworking mentality has inspired me to always keep going, and be a kinder person.

Willem van Lynden
Delft, November 2023

Summary

Ambipolar Plasma Thrusters (APTs) are Electric Propulsion (EP) systems that offer many advantages over other systems, such as simplicity, flexibility, longer operational lifetime, and the ability to produce high density or hot plasmas. However, the flow and behavior of the plasma throughout this type of thruster is not yet well-understood. Because plasma's are not only extremely hot but also very reactive to any electromagnetic (EM) interference, properly testing and diagnosing thrusters is also a difficult area in the field of EP as facility effects cause results obtained on-ground to not be representative of the performance in-space. Therefore, the EP community relies heavily on the modeling of thrusters for both initial and detailed design, as well as an aid in the verification and validation of a thruster's performance[1]. This being said, due to the many strongly coupled physical phenomena occurring in a plasma, modeling such a plasma is just as difficult. Furthermore, because the plasma flow inside an APT encounters two different regimes, the fluid regime inside the thruster's source chamber and the kinetic regime inside the thruster's magnetic nozzle, modeling a thruster completely has been very difficult in the past.

To improve the accuracy of APT modeling, this thesis study implements and evaluates novel coupling methodology between fluidic and kinetic solvers to find a coupled method that can predict the propulsive performance of an APT with higher accuracy than current plasma models. Two models have been employed to this end, 3D-VIRTUS [2], [3] and the PIC code Starfish [4]. The first has been employed for simulating the ionization chamber, namely the fluidic regime, while the latter tackles the plume simulation, i.e., the kinetic regime. These two models are coupled together through a closed-loop iterative coupling scheme, which allows to predict the plasma transport within the whole thruster domain in a self-consistent fashion.

Before starting the development of the coupled model, a literature study is conducted into the operation of APTs, the fundamental theory used to model plasma flow through these thrusters, and the state of APT modeling itself.
Unlike thermal rocket engines, EP systems function by accelerating gases using electrical heating and/or electric and magnetic forces. APTs specifically generate and heat an ambipolar plasma through electromagnetic (EM) wave power coupled in a magnetic field. The two most developed types of APTs are the Helicon Plasma Thruster (HPT) and the Electron Cyclotron Resonance Thruster (ECRT).
An APT generally consists of a dielectric chamber, a propellant gas injection system, an EM wave antenna externally wrapped around the chamber, often in the radio-frequency (RF) or microwave frequency range, and magnetic coils or permanent magnets that create a magnetic field along the longitudinal axis of the chamber. The EM waves generate a high-density plasma, which is contained by the magnetic field inside the chamber. This plasma is then exhausted at chamber outlet, where it is accelerated by a diverging magnetic field to enhance thrust. The dielectric chamber in which the plasma is created is referred to as the source chamber and the area outside where the magnetic field diverges, is referred to as the magnetic nozzle.
The created plasma consists of neutral particles, ions and electrons. These are referred to as the plasma species, each having different characteristics: neutrals are heavy and without charge, ions are heavy with positive charge and electrons are light with negative charge. Inside an APT the plasma density, measured in particles per volume, ranges from $1 \times 10^{20}\,\mathrm{m}^{-3}$ in the source chamber to $1 \times 10^{16}\,\mathrm{m}^{-3}$ in the magnetic nozzle. It's temperature generally falls somewhere in the $1 \times 10^{4}\,\mathrm{K}$ to $1 \times 10^{5}\,\mathrm{K}$ range.
APTs can use a variety of propellants, including xenon, argon, iodine, hydrogen, nitrogen, methane, ammonia, and nitrous oxide. The choice of propellant can greatly enhance mission adaptability and operational freedom. In terms of propulsion, APTs, like all EP systems are characterized by low-thrust in the mN range and high-specific impulse (I_{sp}). Depending on the propellant, experimental specific impulse values between $3000\,\mathrm{s}$[5] and $5000\,\mathrm{s}$[6] have been measured. Although APTs are simpler in design, generally will have a longer lifetime, and can operate with a much larger propellant-range compared to traditional methods of EP,they are also characterized by a lower thrust efficiency. Experimental mea-

surements of thrust efficiency of operational thrusters have mostly remained under 6%[7]. However, recent high-power experiments have approached 30%[8].

To predict the performance of APTs and understand their behavior such that better thrusters can be made, the plasma flow through the thruster must be accurately modeled. This means that a dynamic theory is required to describe the state of a system in time and predict its future state. Mathematical theories for fluids and plasmas are categorized into different levels of accuracy. Of importance for this thesis work are the kinetic and fluid theories. Of these two, the kinetic theory is more accurate. This uses a Probability Density Function (PDF) to provide the particle number density in the six-dimensional phase-space of a given plasma species at a given time. Less accurate but more computationally efficient for high density plasmas is plasma fluid theory. When frequent collisions in the plasma keep the PDF in local regions close to the Maxwellian distribution, these regions have the properties of a system in thermodynamic equilibrium and follow continuum dynamics. A more accurate variation of this mathematical theory is multi-fluid theory, which accounts for the different behavior of positively and negatively charged species.
Within a plasma system, the plasma can exist in different states across time and space. Different levels of theory are more suitable to apply to different states; while kinetic theory is the most accurate, it is inefficient to apply to a high density region where a fluid theory would suffice. The 'regimes' of the plasma flow denote whether the flow can be described as a fluid (continuum) flow or if it can only be adequately described through kinetic theory. The transition from the fluid to kinetic regime is driven by the rarefaction of the plasma and a separation of charge. However, the exact transition in plasma is not yet well-understood, and there is no current consensus in literature regarding a consistent theory for the physics at play describing the transition, its specific criteria, or a numerical solution for modeling what happens.

Solvers that model the behavior of APTs can be divided based on the fundamental theory that they apply to the plasma flow throughout the thruster. Of relevance for this work are therefore the fluid solvers and the kinetic solvers. Specifically this work focuses on so-called multi-regime solvers, solvers that couple fluid and kinetic solvers together to enable the modeling of plasma flow which undergoes a regime change.
The state of the art in APT Multi-regime solvers has specifically been analyzed to define the most severe limitations in the coupling of different models across the different plasma flow regimes experienced in an APT. Using the numerical suite developed at the universities of Padova and Bologna by Magarotto *et al.* (2021)[9] as a baseline, four main limitations were found: the spatial profiles of plasma properties are simplified and made uniform when transferring these between domains, continuity of plasma species is not upheld between models, the numerical domains do not reflect the plasma flow regimes accurately and the coupling between plasma flow and EM power is not consistent between models. Out of these four, this thesis work focuses on the development of the physical framework, methodology, and numerical implementation to resolve the first three limitations. The first three all concern varying levels of flow theory, while the last limitation also involves EM-power coupling which lies outside the scope of this work.
Removing or reducing these limitations should thus result in a more accurate multi-regime model for APT thrusters. To this end, the following three improvements are proposed to each address one of the three respective limitations. First, the coupling of plasma profiles between the separate model domains should be conducted with higher spatial-fidelity, respecting radial variance rather than assuming uniform profiles. Second, the continuity of all species should be achieved through a corrective iterative loop. Third, the numerical domains must be redistributed according to physical indications of regime-change.

Following the literature study, it was chosen to base the new multi-regime coupled model on the numerical suite developed by Magarotto *et al.* (2021). Therefore, the chosen fluid solver is based on the 3D-VIRTUS code[2] and the Particle-In-Cell (PIC) kinetic solver on the Starfish code[4], both utilised in the baseline numerical suite.
A step wise approach has been taken to implement the intended coupling improvements into a single coupled solver, the MUlti-regime Plasma Equilibrium Transport Solver (MUPETS). Step 0 concerns the higher-fidelity coupling of spatial-variance in the plasma properties which are passed between the models. Step 1 concerns the implementation of new, coupled boundary conditions (BCs) to remove imposed conditions at the models domain interface such as the Bohm criterion, utilizing an iterative loop to do so. Due to the long run time of the PIC code, each iteration takes roughly 5 days. Step 2

then would implement the mapping of the actual physical regimes in the thruster as denoted by the local Knudsen value, such that the numerical domains could be updated between iterations according to the updated location of the respective regimes. This last step however was not possible to implement in the time frame of the thesis work, and is left for future work. Considering Step 0 and Step 1, two approaches to coupling the numerical domains for these steps were found. The first approach involved directly coupling the numerical domains at a single domain interface, whereas the second approach included an overlap of the numerical domains, splitting the coupling over two sub-interfaces.

To verify the performance of the physical methodology and its numerical implementation, a generic thruster case was simulated with varying magnetic fields applied. These included: no magnetic field, a uniform magnetic field in the source chamber and a realistically diverging magnetic field in the magnetic nozzle and a realistic magnetic field throughout the entire thruster. During the verification, it was found that of the two numerical domain coupling approaches, only the approach of direct domain coupling could be successfully verified, the domain overlap approach failed to provide plasma profiles respecting the fundamental continuity equation. The axial and 2D plasma profiles as predicted by Step 1 accurately demonstrated the same trends predicted by theory and observed in other high-performance models. The discontinuity of the electron density at the source outlet, observed in the baseline numerical suite[9], was reduced from 7% to 4%. The model generally converges after two iterations when using a convergence criteria of electron density remaining within 10% between iterations, which corresponds to the general electron current measurement uncertainty in APT experiments[10], [11].

Besides verification, the performance of MUPETS, with the direct numerical domain coupling approach implemented, has been validated through comparison of the predicted propulsive performance with experimental measures of a laboratory thruster at the university of Padova. Due to time restrictions, this thruster was only modeled with an ideal, uniform, magnetic field inside the source section and a realistically diverging magnetic field inside the magnetic field section.
With this simplified case, the predicted propulsive performance differed less than 19% from the experimentally measured performance, showing an improvement over previous results[9]. Furthermore, a preliminary parameter sweep was conducted for the power deposited into the plasma to investigate the propulsive envelope of the thruster. However, when compared to real experimental values, the model's performance was overestimated due to the use of a uniform magnetic field and the neglect of neutral thrust. When applying a preliminary correction to the predicted thrust values it was found that while there was little change at the lower limit of the considered power range ($15\,\mathrm{W}$), at the upper limit ($57\,\mathrm{W}$) the thrust could be overestimated by 84%. Future work should include running this case to determine the actual performance prediction and identify areas for model improvement.
The conducted parameter sweep found a near-linear increase in thrust, specific impulse and propulsive efficiencies with increasing power in the simulated low-power range.

Analyzing these results, it is concluded that the resulting coupling method, which consists of the higher-fidelity passing of plasma properties across a single domain interface inside a self-correcting iterative loop presents an improvement to the state of modeling APTs, such as Helicon Plasma Thrusters (HPTs), Electron Cyclotron Resonance Thrusters (ECRTs), microwave thrusters, and in general, multi-regime plasma flow problems. Furthermore, as the MUPETS code requires minimal alteration of the separate solvers themselves, the fluid or kinetic solvers can be swapped out with higher-fidelity models or numerically better performing models as required, without altering the required physical methodology. Due to this modality, many previously developed and validated models from literature could also be compared in this framework to investigate their suitability for describing the plasma flow across the regime change.

Contents

List of Figures

List of Tables

Nomenclature

Abbreviations

Abbreviation	Definition
APT	Ambipolar Plasma Thruster
BC	Boundary Condition
DD	Drift Diffusion
ECRT	Electron Cyclotron Resonance Thruster
EP	Electric Propulsion
EM	Electro Magnetic
GIT	Gridded Ion Thruster
HET	Hall Effect Thruster
HPT	Helicon Plasma Thruster
MUPETS	MUlti-regime Plasma Equilibrium Transport Solver
PDF	Particle Distribution Function
RF	Radio-Frequency
VDF	Velocity Distribution Function

Symbols

Symbol	Definition	Unit
a	Acceleration	$[ms^{-2}]$
B	Magnetic field	$[T]$
D	Diffusion coefficient	$[m^2s^{-1}]$
D_W	Plasma drag	$[N]$
E	Electric field	$[Vm^{-1}]$
e	Elementary charge	$[C]$
e_I	Ionization potential	$[J]$
e_L	Thruster energy losses	$[J]$
F	Force	$[N]$
f	Particle distribution function	$[-]$
g	Plasma parameter	$[-]$
g_0	Gravitational standard at Earth	$[ms^{-2}]$
I_{sp}	Specific impulse	$[s]$
J_θ	Azimuthal current	$[Cm^{-2}s]$
K_n	Knudsen number	$[-]$
k_B	Boltzmann constant	$[m^2kgs^{-2}K^{-1}]$
L	Characteristic length scale	$[m]$
M_W	Molecular mass	$[u]$
M_i	Ion mass	$[kg]$
m	Species mass	$[kg]$
m_e	electron mass	$[kg]$
$\dot{m}$	mass flow rate	$[kgs^{-1}]$
N	Amount of particles	$[-]$
N_A	Avogrado constant	$[mol^{-1}]$
n	Number density	$[m^{-3}]$
P	Power	$[W]$

Symbol	Definition	Unit
q	Particle charge	[C]
R	Source chamber radius	[m]
r_c	Cyclotron radius	[m]
T	Thrust, Temperature	[N],[K]
T_e	Electron Temperature	[eV]
t	Time	[s]
v	Velocity	[ms^{-1}]
v_e	Exhaust velocity	[ms^{-1}]
V	Volume	[m^3]
x	Position in space	[m]
Γ	Particle flux	[$m^{-2}s^{-1}$]
ϵ_0	Permittivity of free space	[$m^{-3}kg^{-1}s^4A^2$]
η	Thrust efficiency	[$-$]
η_p	Production efficiency	[$-$]
η_u	Propellant utilization	[$-$]
λ	Mean free path	[m]
λ_D	Debye length	[m]
μ	Mobility coefficient	[$m^2V^{-1}S^{-1}$]
π	Pi	[$-$]
ρ	Density	[kgm^{-3}]
τ	Collision time	[s]
ϕ	Plasma potential	[V]
ω	Angular frequency	[$rads^{-1}$]

1

Introduction

Current challenges related to propulsion in space are many: With the advent of CubeSats, in order to truly enable this new and proven platform to its full potential, propulsion systems must downscale in both volume and mass to offer the same capabilities to these platforms as their larger counterparts. At the same time, propulsion systems, especially those used for attitude control purposes must be able to deliver repeated small and precise thrust increments, requiring near unlimited restarts with consistent performance.[12] Furthermore, to accommodate longer duration or distance missions in or far beyond Earth orbit, larger Delta-V requirements must be met, requiring more propellant on board of a spacecraft or more efficient propulsion systems. Finally, to further extend mission duration at destination or destination distances, propulsion system lifespan must be increased by decreasing degradation of system parts or by simplifying the propulsion system to lower risk of system failure. Electric rocket propulsion, its general performance being characterized by low thrust, high specific impulse and limited moving parts can provide an answer to said challenges. Relatively mature electric propulsion (EP) systems, such as Gridded Ion Thrusters (GIT) and Hall Effect Thrusters (HET)[13]–[15] are already commonly available on the market. These systems are, however, both complex, costly, and plagued by erosion of their anodes, limiting their useful lifetime. In comparison, the Ambipolar Plasma Thruster (APT), a newly-researched[12]–[14] type of electric thruster has an especially simple design, yielding long operational lifetimes, low costs and larger flexibility[5] as opposed to GITs and HETs. APTs are generally grouped into Helicon Plasma Thrusters (HPT)[16] and Electron Cyclotron Resonance Thrusters (ECRT)[17]. The initial investigations into HPTs were conducted by Boswell and the space plasma propulsion group at the Australian National University in the early 2000s [18]. Subsequently, HPT technology underwent further development at the University of Padova through various projects, including the European HPH.COM [19] and the Italian SAPERE/STRONG [20]. The outcomes of these two initiatives paved the way for the creation of the $50 - 150W$ REGULUS thruster [7], [21], a propulsion unit developed by T4i [22] designed for CubeSats larger than 6U and SmallSats. NASA's VASIMR rocket is another notable example of a propulsion system utilizing a Helicon source for its production stage [23], operating at high operating power($200\ kW$)[24]. Moreover, SENER Aerospacial and the University of Madrid designed a $1\ kW$ thruster within the HIPATIA project [25], [26]. Similarly, the universities of Stuttgart and Manchester have been working on an atmosphere-breathing HPT for Very Low Earth Orbits [27]. Institutions such as the Tohoku University [28], the Massachusetts Institute of Technology [29], the Michigan Institute of Technology [30], and Washington University [31] also have made significant contributions to the advancement of HPT technology.

As APTs are relatively novel compared to HETs or GITs, and the physical phenomena at play are not yet all fully understood[32], a universal methodology capable of accurately and efficiently modeling the full plasma transport throughout the entire thruster has yet to be achieved. Often the models describe only one of two sections of the HPT, either the helicon source chamber (production stage)[33], or the magnetic nozzle (acceleration stage)[34]. Models analyzing the entire flow or performance do exist[35], [36], but are often a simplified combination of the previous separate models or reduce one of the domains to a global model[33], [37]. In general, modeling efforts in electric propulsion are plagued by two

challenges. Firstly, the large amount of interlinked physics and parameters at play make it difficult to find a definitive model to use. Secondly, extremely high plasma temperatures and general plasma flow sensitivity prevent easy placement of diagnostic probes within the plasma without melting the probes or disturbing the flow. Ensuing uncertainty of data sets hinder model verification and validation.
In order to improve performance and capabilities of APTs so that they can be utilized to their full potential in enabling future long-duration, low-cost or high-reliability missions the design tools need to be strengthened by more accurate and efficient models.
The objective of this thesis is to develop and implement a set of novel coupling methods between fluid and kinetic plasma flow models to improve the accuracy of APT modeling.
This work is structured in the following manner: firstly, the research case following the stated objective of this thesis is presented in chapter 2. An introduction to the relevant plasma physics for the modeling, design and operation of electric propulsion systems is given in chapter 3. The description of various APT concepts and their working principles follows in chapter 4. A more in-depth look at the fundamental plasma flow theory used in the relevant models is given in chapter 5. chapter 6 summarizes of a literature study conducted on the state of the art of APT modeling and identifies the limitations that this thesis work sets out to improve. Finally, chapter 7 presents the development of the coupling methods leading to the novel coupled model and its numerical implementation in the MUlti-regime Plasma Equilibrium Transport Solver (MUPETS) code. After presenting the different coupling methods, chapter 8 concerns the verification and validation process, the final selected coupling method and predicted propulsive performance results obtained with this coupling method implemented in MUPETS. The thesis conclusion and remarks for future work are given in chapter 9.

2

Research Case

The research conducted in this thesis has been initiated by findings from a literature study on the current state of art and limitations in the modeling of APTs[38]. The literature study specifically focused on the modeling of plasma transport throughout the entire thruster, which is often split between fluid and kinetic models applied to separate domains. The literature study identified several limitations relating to the general fidelity and continuity of the solution, as well as problems with correct and efficient application of numerical domains as dictated by the fluid and kinetic regimes described by plasma transport theory. Several of these limitations could be reduced or removed altogether through the development of a coupled model, which is the topic of this thesis. This coupled model, called MUPETS for MUlti-regime Plasma Equilibrium Transport Solver, is developed from a preliminary coupled fluid-kinetic APT model, the 3DVIRTUS-Starfish numerical suite[9], described in section 6.6. The development and functioning of MUPETS is presented in chapter 7. This chapter describes the intended improvements to APT modeling which this thesis will focus on, the research question question of that this thesis strives to answer, and the objective of the thesis work.

2.1. Improvements to make to APT modeling

A summary of the literature study's found coupling limitations in the 3DVIRTUS-Starfish numerical suite is given in section 6.6. This thesis intends to examine multiple coupling improvements addressing these limitations, in order to develop more accurate modeling. The improvements that are considered for this are summarized below.

First, the domains to which the fluidic source and kinetic plume solvers are applied should be reconfigured to more accurately match where the respective regimes occur. Currently the domains are separated simply by the end of the source chamber section where the magnetic fields start to diverge. This is often referred to as the thruster outlet boundary. On the source chamber side of this boundary the fluid solver, and the kinetic solver is used on the outlet plume, at the other side of this boundary. However, the transition from a fluid flow to kinetic flow, even while considered instantaneous, does not necessarily occur exactly at the the thruster outlet boundary; it is actually more accurately believed to occur somewhat more downstream[39]–[41]. As detailed in section 5.3, this transition can be marked by a sharp rarefaction of the plasma together with a large potential drop. Thus, these two parameters should be considered guiding in where a more accurate transition point or region is mapped, which then determines where to employ the fluid, and where to employ the kinetic solver. As no prior studies have been performed examining the significance of any introduced error due to the setting of these geometric boundaries, this presents an opportunity for comparison.

Second, the source solver should incorporate the back-flow of electrons into the source chamber in its solution. As the plume solver utilizes a potential at infinity, downstream from the thruster to reflect low-energy electrons as described in section 7.2.1. These trapped electrons can reach the thruster outlet and travel back into the source chamber. While they are taken into account in the plume solver, they are not accounted for in the simulation of the source solver through any feedback; hence any effects they might cause inside the source chamber are lost. Updating the electron profile within the

source solver after the plume solver has run, and iteratively looping the solutions of the solvers until a convergence of the electron profiles at the thruster outlet boundary is reached, could remove the current electron profile discrepancies observed[9].
Third, the boundary conditions (BCs) at the thruster outlet for the plume solver should not assume uniformity of the plasma profile, using a value averaged over the entire boundary surface, but rather take the more precise local outputs of the source solver. Lost information on the plasma profile will be reduced, improving accuracy.
Fourth, the applicable domain for the RF-module of the source solver should be extended to a larger domain, to cover all deposited power. Currently, by cutting of the domain at the source chamber's boundaries, the model fails to consider a non-negligible amount of deposited power[42].

2.2. Research questions

The improvements to APT modeling described in section 2.1 all aim to address limitations imposed by simplified coupling of different regime models to each other. Achieving these improvements through an improved coupling methodology will therefore lead to the removal or reduction of the described limitations and subsequent inaccuracies in the model. This should lead to a more accurate model with a wider area of applicability. Thus, finding a method which can self-consistently encompass the intended coupling improvements should result in an improved multi-regime coupled model. To find this improved coupling method and develop the subsequent multi-regime coupled model, this thesis will attempt to answer the following research question (RQ), associated sub-research questions (SRQs) and their respective sub-sub-research questions:

RQ. What physically appropriate numerical coupling method between the plasma fluidic and kinetic solvers can provide more accurate results in a multi-regime APT model when compared to APT experimental results?

SRQ1. What coupling methods will or can be tested?

- 1.1 What are the most important coupling methods between fluidic and kinetic plasma models, applicable to an APT?
- 1.2 Which of these are physically appropriate?
- 1.3 How can these be made numerical?

SRQ2. How can the coupling methods be compared?

- 2.1 What metric will be used to evaluate accuracy?
- 2.2 How can the coupling methods be verified?
- 2.3 How can the resulting MUPETS code be validated?

The rest of this thesis will cover the work conducted to answer these questions.

2.3. Research objective

Through researching the previously described research questions, the main research objective of this thesis is:

> To improve the accuracy of Helicon Plasma Thruster modeling by implementing and evaluating different coupling methods between fluidic and kinetic solvers.

Tasks for reaching this objective have been identified and are summarized below.

2.3.1. Set the scope of the model subject

To start work on plasma thrusters and understand the subject which will be modeled, first one needs to familiarize themselves with some of the fundamental principles in plasma physics and what sets this field apart from regular energetic fluid or gas behavior. Explanation of the principles of plasma physics and the practices used when describing these is given in chapter 3. At the same time, the plasma's considered in thesis are limited to those relevant in electric propulsion systems, specifically APTs. To

understand the behavior of the plasma in an APT, its use for propulsion and the phenomena expected to occur inside an APT, the working principle of APTs shall be covered in chapter 4.

2.3.2. Define the theory and modeling framework

In order to accurately approach and appropriately handle the modeling of the plasma flow, it is necessary to define the theory and modeling frameworks which are used to differentiate the flow into regimes, and associated applicable models, according to relevant flow conditions. The multiple physical theories used for this and the description of the regimes considered are presented in chapter 5. The categories of model that result from the different physical theories are then covered in chapter 5 and the limitations encountered when coupling different models together are presented in section 6.6.

Implementing different coupling methods

First, the set of improvements to carry out must be chosen and ordered. This selection is covered in section 7.1. Second, theoretically possible methods to carry out said improvements are then defined. The resulting physical methodology is described in section 7.2. Third, it must be investigated how methods deemed appropriate with respect to the physical phenomena can be applied numerically. More specifically, these methods must be implemented numerically into, and interfacing with, the OpenFOAM and Starfish codes. The numerical methodology is therefore presented in section 7.3.

Evaluating different coupling methods

When implemented, the results of the coupled models must be verified and validated. This must be done before any coupling methods can be compared against the baseline models or different methods. Verification and validation of the coupling methods is conducted in chapter 8. Subsequently, of the resulting validated methods, a best coupling method shall be selected through comparison against each other and against a baseline.

3

Plasma Physics Concepts

Before the operation of any generic plasma thruster can be described and different thruster models can be identified and analysed, some basic insight into the relevant concepts and practises in the field of plasma physics is required. This chapter covers the core concepts and practices that will form the basis of descriptions of further phenomena in the rest of this thesis and introduce any fundamental conventions.

3.1. Plasma definition

Plasmas, the scientific fourth state of matter, exist in many different forms in the universe, making up most of the normal matter in the universe[43], [44]. The term ”plasma” was first coined by Tonks and Langmuir in 1929 and is taken from the Greek word for ”something moulded”. The term is used to describe ”a quasi-neutral gas of charged and neutral particles which exhibits collective behaviour”[44]. These charged particles consist of electrons and ions. However, to be classified as a plasma, three criterion must be met. These three criterion are on the plasma net-charge, the plasma parameter and the plasma frequency. They will be explained in the next three subsections.

3.1.1. Charge neutrality and Debye shielding

In the absence of external disturbances a plasma must be macroscopically neutral: Under equilibrium conditions in a volume of the plasma the net resulting electric charge is zero. In a plasma this is maintained through ’Debye shielding’: When imposing a charge in a plasma, the plasma particles of opposite charge will arrange themselves as a cloud surrounding the foreign charge to effectively shield any electrostatic fields originating from it. This shielding is achieved within a distance of the order of the Debye length λ_D.

$$\lambda_D = \left(\frac{\epsilon_0 k_B T_e}{n e^2} \right)^{\frac{1}{2}} \tag{3.1}$$

Here, ϵ_0, k_B and e are the permittivity of free space, the Boltzmann constant and the elementary charge respectively. T_e is the temperature of the electrons in the plasma in Kelvin and n is the plasma number density, portraying the amount of free electrons, or ions, in a volume of plasma. The latter two concepts and their respective important use of units will be explained in sections 3.3 and 3.4. If the characteristic dimensions L of a system are much larger than the Debye length, then whenever local concentrations of charge arise or external potentials are introduced into the system they will be shielded out through a distance smaller than L, leaving the bulk of the plasma free of large electric potentials or fields and hence maintaining a macroscopically neutral plasma. This is the first criterion. Sometimes it is split in two dependent criteria[43] but the choice is made here to only use independent criteria as in [44]. For a HPT, the typical Debye length will vary from about 10^{-7}m in the source chamber to 10^{-4}m in the magnetic nozzle[5], [45], [46]. When compared to other plasmas in the universe, this value is on the short end of the spectrum, as can be seen in figure 3.1[43], where the HPT field would be roughly placed between, and slightly overlapping with, the solar atmosphere and glow discharges, with

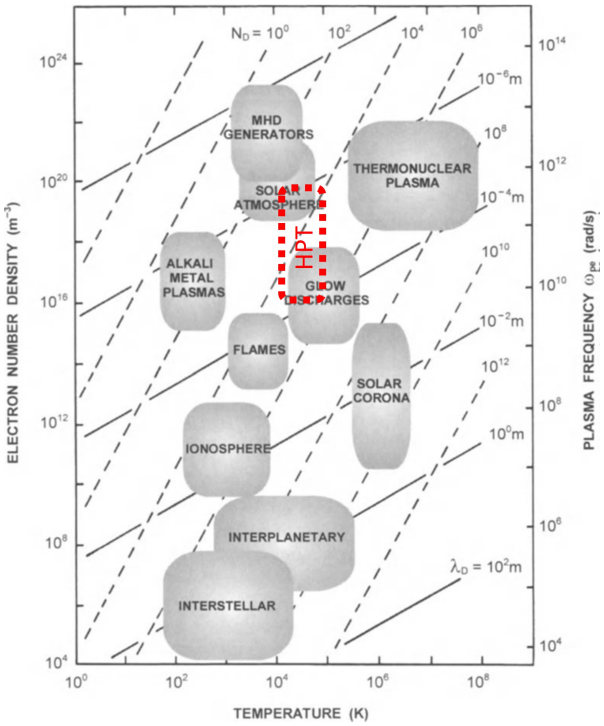

Figure 3.1: Ranges of temperature and electron density for several laboratory and cosmic plasmas and their characteristic physical parameters: Debye length λ_D, plasma frequency ω_{pe} , and number of electrons N_D in a Debye sphere. MHD: magnetohydrodynamic. The original image has been altered by the author to include in dotted red the outline of the HPT plasma area.[43]

a standard temperature in the $10^4 - 10^5 K$ range[46]. The small Debye length is due to the large electron number density associated with the HPT, typical electron densities are in the range of $10^{18} - 10^{20} m^{-3}$ in the source [5] and $10^{16} - 10^{18} m^{-3}$ in the magnetic nozzle[45].

3.1.2. Plasma parameter

A large number of electrons must be inside a Debye sphere for this collective particle shielding effect to actually work. This provides the second independent criterion.

$$n_e \lambda_D^3 >> 1 \tag{3.2}$$

The plasma parameter g is a quantity that is used to measure this condition as it is defined as the inverse of the number of simultaneously interacting particles.[47]

$$g = \frac{1}{n_e \lambda_D^3} \tag{3.3}$$

Substituting g into equation (3.2) an alternate form of the second criterion is obtained, stating that g must be much smaller than 1:

$$g << 1 \tag{3.4}$$

This form of the second criterion is referred to as the plasma approximation.

3.1.3. Plasma frequency

Finally, charged particles in a plasma must not collide with neutral particles too often, as otherwise the electrons will not behave independently anymore, but will be forced by collisions to be in complete equilibrium with the neutrals, and the plasma will be akin to a neutral gas. This forms the final and third criterion. It is formulated through τ, representing the average time for an electron between a collision with a neutral, and ω, representing the angular frequency of typical plasma oscillations. A frequency which can be used for representing the typical plasma oscillations is the electron plasma frequency,

which depends on the number density of the electrons:

$$\omega_{pe} = \left(\frac{n_e e^2}{m_e \epsilon_0} \right)^{1/2} \tag{3.5}$$

The average time between electron-neutral collisions must then be large compared to the characteristic time during which the plasma physical parameters are changing[43]. As the plasma frequency thus scales with the root of the electron density, looking at figure 3.1 one can see the HPT plasma frequency should be relatively high, as is its density, and generally will fall in the range of $10^{10} - 10^{12}$ rad/s.
The three criteria for a plasma can then be formulated as:

1. $\lambda_D << L$
2. $g << 1$
3. $\omega\tau < 1$

3.2. Larmor radius and magnetisation

In a plasma under a uniform straight magnetic field of strength B, both the ions and electrons will gyrate about the magnetic field lines, causing a helical motion. The radius of the circular orbit that they draw on the orthogonal plane to the magnetic field line is called the Larmor, gyro- or cyclotron radius r_c and is given by:

$$r_c = \frac{m v_\perp}{eB} \tag{3.6}$$

where m is the mass of the charged species and $v_\perp$ its velocity component perpendicular to the direction of B. When r_c is larger than the characteristic length L of a system under consideration, a particle is called 'unmagnetised' as opposed to being magnetised' if it has a smaller Larmor radius instead. An magnetised particle will follow the path of magnetic lines as it experiences a stronger radial acceleration correcting the particle's helical trajectory, also if they diverge, while an unmagnetised particle's direction of motion remains relatively unaffected as it's heavier mass results in a much smaller acceleration. For an HPT, this is the case for the heavy ions and neutrals, which will travel in near straight-lines within the limits of the system and thus not follow the field lines while these lines diverge, while the much lighter electrons, having a small Larmor radius, will follow the diverging lines closely.

3.3. Plasma density and quantities

A plasma consists of many different particles at many locations with different velocities. Hence, in Plasma physics, use is commonly made of a particle distribution function (PDF) $f(\mathbf{x}, \mathbf{v}, t)$ of each distinct particle such as neutrals, electrons and ions. To obtain the local number density n of a species, the PDF is averaged over the velocity space.

$$n(\mathbf{x}, t) = \int f(\mathbf{x}, \mathbf{v}, t) d\mathbf{v} \tag{3.7}$$

n is a much used quantity throughout the field of plasma physics as is already shown in the previous sections. It is often referred to as simply the density, and it's important to note its unit is m^{-3}.
To then obtain the value of a particle parameter G in position **x** at time t, averaged over the ensemble of particles, the value of G for a specific value of **v** is multiplied by the number of particles with that velocity **v**, and then divided by the total number density of particles:

$$\langle G \rangle = \frac{\int G(\mathbf{v}) f(\mathbf{v}) d\mathbf{v}}{\int f(\mathbf{v}) d\mathbf{v}} \tag{3.8}$$

An HPT is characterised by it's ability to produce a high density plasma in the source chamber, varying between 10^{18} to $10^{20} m^{-3}$ in the source[5]. As seen in figure 3.1, this puts the HPT source plasma in the region bridging high density glow discharges to low density thermonuclear plasma.

3.4. Plasma energy and temperature

In a plasma in thermal equilibrium, associated with many collisions, the PDF is in the form of the Maxwellian distribution[44], [47]. In the i-dimensional ($i = 1, 2, 3$) form this PDF is given by

$$f(u) = n \left(\frac{m}{2\pi k_B T} \right)^{\frac{i}{2}} exp \left(-\frac{1}{2} \frac{mv^2}{k_B T} \right) \tag{3.9}$$

As seen this distribution depends on the plasma temperature T, it defines the width of the distribution. When the particle kinetic energy E_k is chosen as parameter G and it is averaged over the plasma, the average energy is obtained

$$\langle E_k \rangle = \frac{1}{2} k_B T \cdot i \tag{3.10}$$

where i is the number of velocity dimensions considered in the system being 1,2 or 3. This energy depends purely on the plasma temperature and hence is often also referred to as the thermal energy of the plasma. Due to this correlation between temperature and energy, the unit for temperature used in plasma physics is the electron volt, eV. The electron volt as a unit of temperature is related to joules and kelvin as follows:

$$1\,\mathrm{eV} = \frac{1.6 \times 10^{-9}\,\mathrm{J}}{k_B} = 11\,600\,\mathrm{K} \tag{3.11}$$

Thus, although mentioned earlier the range of the HPT plasma temperature is in the $10^4 - 10^5 K$ range, from now on this is referred to as the $10^0 - 10^1 eV$ range[46]. The HPT plasma temperature falls roughly in the middle of the plasma range as seen in figure 3.1.

3.5. Species

This thesis considers any plasma to consist of 3 types of particle species: ions, electrons and neutrals. Ions are heavy, charged particles, often carrying a positive charge though they can carry a negative charge as well. Electrons are light, single negatively charged particles. Neutrals are also heavy particles but they do not carry any charge, they can however be in either the ground state or in many different excited states. To ease derivation of theory and computational cost this thesis shall assume that ions are always single positive ions and neutrals are assumed to be in the ground state unless stated else-wise. The types of collisions required to create double charged or negative ions are much fewer, and less likely to occur, than the collisions creating single-positive ions, including the reactions creating single-positive ions from negative or double charged ions[48]. Due to this, double-charged or negative-charged ions make up a negligible amount of the plasma population, [49] and are therefore neglected. The properties of the ion, electron and neutral species are commonly distinguished by the subscripts i, e and n respectively. Sometimes the neutrals will be denoted by subscripts 0 or g, $1Sr$, $1Sm$ and $2P$ instead. The latter four for example are used when considering excited neutral species separately for a more detailed model[49].

4

Ambipolar Plasma Thrusters

Unlike a thermal rocket engine, where the thrust is obtained through expansion of a chemically heated propellant, the functioning of any electric propulsion relies on ”the acceleration of gases [...] by electrical heating and/or by electric and magnetic body forces” as stated by Jahn(1968)[12]. Many EP thrusters use a cathode to generate plasma and neutralize their exhaust. The APT does not utilize a cathode for its working but rather generates and heats an ambipolar plasma through EM-wave power coupled in a magnetic field. The EM-waves used can be in the radio-wave frequency (RF) range or for example in the micro-wave range. Often the thrusters use a magnetic nozzle for accelerating the energetic plasma into the axial direction to produce enhanced thrust. The two most developed types of of APT to date are the Helicon Plasma Thruster (HPT) and the Electron Cyclotron Resonance Thruster (ECRT). Both utilize RF waves and a Magnetic nozzle. The HPT couples the EM power into the plasma through helicon waves, hence the name, creating a high density plasma in the order of $n_e, n_i \approx 10^{20}$[46]. An ECRT instead couples the power through a high-frequency EM field with the same frequency as the electron cyclotron resonance frequency, $\omega = \frac{eB}{m_e}$, causing resonance heating[50].

4.1. Working Principle

Due to its simple design, the HPT shall be used to further explain the working principles and general components of APTs. The coupling methods and the resulting coupled model developed in this thesis work shall however be applicable for all types of APTs. Much like a regular thermal rocket engine, the HPT can be divided in two sections, the chamber and the nozzle. A schematic drawing of a HPT, the stages and their connection to a propellant storage tank can be seen in figure 4.1[51].

The HPT contains a dielectric chamber, propellant gas injection system, radio-frequency (RF) antenna externally wrapped around the chamber and magnetic coils or permanent-magnets that create a magnetic field along the longitudinal axis of the chamber[52]. The chamber is not meant for combustion, but for containing the introduced propellant gas while the antenna surrounding it ionizes the gas and deposits electromagnetic (EM) power into it through RF waves, in order to develop the energetic plasma[2]. More specifically, the antenna design generates the so-called helicon wave and a secondary Trivelpiece-Gould wave which create a high-density plasma at comparatively low power[46], [53]. The magnetic field is present to i) contain the plasma within the source chamber, ii) drive the power coupling of the RF waves into the plasma[54] and iii) allow the plasma to expand when it leaves the source, where the magnetic field diverges as a so-called magnetic nozzle[55]. When the plasma is created in the source chamber, it can only expand out of the chamber on one open end, opposite to where the propellant gas was injected, much like a combustion chamber. At this open end, the flow is accelerated by a diverging magnetic field[56], allowing the flow to expand, much like the diverging part of a thermal rocket engine. The combined action imposed on the plasma by the chamber and the magnetic field pressure in the magnetic nozzle then add to the total momentum of the plasma flow, creating the thrust that the HPT exerts[57]. This process is illustrated in figures 4.2a and 4.2b, taken from Takahashi(2019).

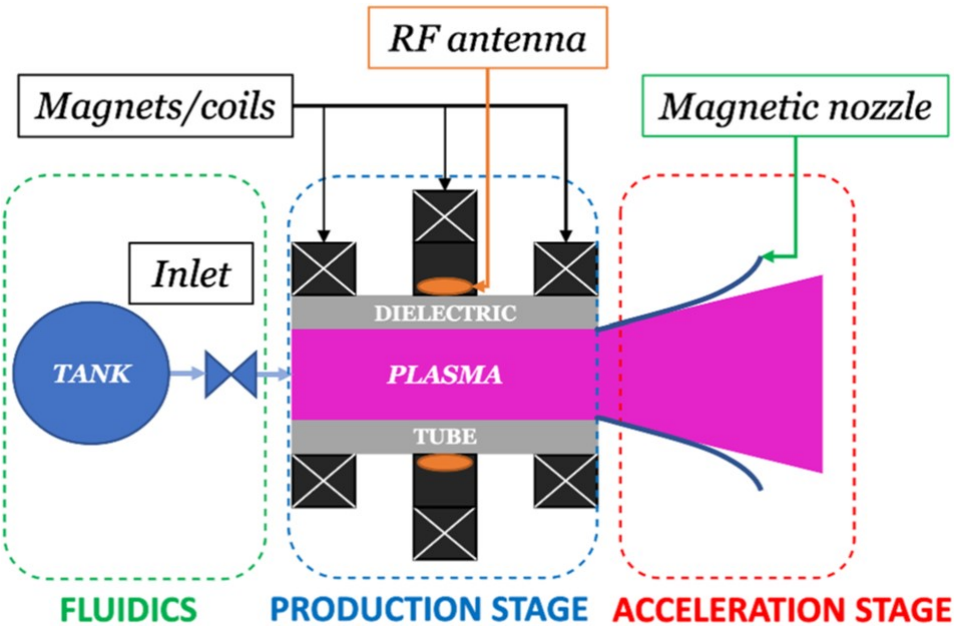

Figure 4.1: Schematics of a Helicon Plasma Thruster[51]

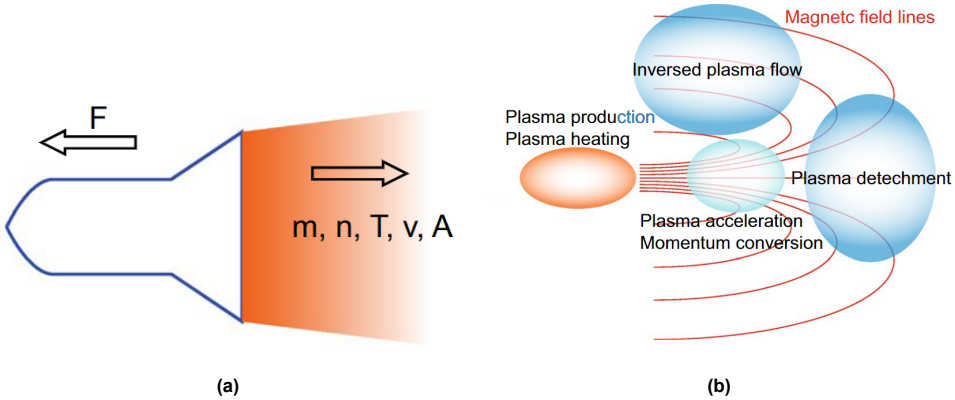

Figure 4.2: a Physical picture of the thrust imparted by the momentum flux exhausted from the rocket. b Physical issues in the RF magnetic nozzle plasma thrusters[5]

4.2. APT advantages over other thrusters

Several advantages of APTs over contemporary methods of EP can be proposed:

- Simpler design with fewer parts removes limitations on lifetime caused by erosion and reduces risk of parts failure[58]. For example, traditional EP thrusters require cathodes and grids to accelerate and neutralize the expulsed plasma to prevent the spacecraft from accumulating charge. APTs exhaust a net-neutral ambipolar plasma; the outgoing flux of the plume contains a global equal amount of negative and positive particles, removing the need for neutralizing the exhaust plume. Removing these erosion-prone parts virtually extends the lifetime indefinitely[5]
- APTs can operate in a wide range of design and operational parameters[37]. This enhances the opportunity to optimize designs for different mission requirements[14]. Specifically, a large range of propellants can be used[49], [59] and it should be possible to change between certain propellants 'on the go' by changing the propellant feed and operating pressure only[60]. This greatly enhances mission adaptability, allowing the use of secondary backup propellants which can be byproducts of other processes in the spacecraft or can be swapped between other spacecraft use and propulsion system use if an emergency arises[33].

- HPTs specifically produce high density plasma at relatively low power [44], [53], aiding thrust.
- ECRTs instead reach a high plasma temperature[44], also aiding thrust.

A drawback of current APTs is the low thruster efficiency, with the modeled HPT thruster efficiency falling between 20 to 30%[52], [57], [61]. Experimental measurements however, have mostly remained under 6%[7] in the sub kW power range, although high power experiments have indeed approached 30%[8], [62]. HETs and GITs on the other hand, although held back by limited lifetime and other drawbacks, are characterized by much higher operational efficiencies. These have reached above 60% and 70% respectively[13].

4.3. Propulsive Performance

The performance of a thruster can be measured by its thrust level, specific impulse, power consumption and associated efficiencies. A rocket produces thrust by expulsing a gas or fluid, creating a total momentum flux. For operations in the vacuum of space, which form the applicable area of EP thrusters, the total thrust of any rocket is given by the total momentum flux of the exhausted propellant, integrated over the exhaust cross section A. The momentum flux is the sum of the static pressure p_I and dynamic pressure $m_I n_I u_{Iz}^2$ of each species $I = i, e, 0$ of the exhausted propellant:

$$F = \sum_{I=i,e,0} \int_A (p_I + m_I n_I u_{Iz}^2) dA \tag{4.1}$$

When taking the properties of the exhausted propellant flow as one single exhaust flow, the equation can be written with the exhaust area A_{ex}, exhaust pressure p_{ex}, exhaust mass flow rate $\dot{m}_{ex}$ and exhaust velocity, or jet velocity, v_{ex}. This can then be further simplified through the definition of an equivalent exhaust velocity $v_{eq} = v_{ex} + \frac{p_{ex} A_{ex}}{\dot{m}_{ex}}$ as seen in equation (4.2)

$$\begin{aligned} F &= A_{ex} p_{ex} + \dot{m}_{ex} v_{ex} \\ &= \dot{m}_{ex} v_{eq} \end{aligned} \tag{4.2}$$

The specific impulse I_{sp} is the total impulse delivered by the system I, divided by the weight of the propellant used to generate this total impulse. It is given by:

$$I_{sp} = \frac{I}{g_0 m_p} = \frac{\int F dt}{g_0 \int \dot{m} dt} \tag{4.3}$$

Here m_p is the total propellant used and g_0 denotes the gravitational standard at Earth, which remain constant, even when the system considered is utilized elsewhere in the universe. In the case that v_{eq} is kept constant, for example when operating the thruster in steady state without throttling, equation (4.3) can be further simplified through substitution of equation (4.2) and can then be related directly to the thrust:

$$I_{sp} = \frac{F}{\dot{m} g_0} \tag{4.4}$$

Thus, to compute the propulsive performance, it is key to find the thrust of the system.
The pressure for each species is simply calculated through the ideal gas law $p = n k_B T$. As $T_e >> T_i, T_0$, the pressure terms of the heavy species are neglected. At the same time, the momentum term of the electrons is neglected due to the much lower mass of the electrons, $m_e << m_i, m_0$.
Furthermore, as the neutral particles do not gain any energy from the electromagnetic fields, their momentum and pressure do not increase throughout the thruster unless a physical nozzle is included. Although neutral density in APTs is often at least one order of magnitude larger than the plasma density, the ionization ratio $\frac{n_p}{n_0}$ can be expected to lie at least above 10%[32]. Considering that the general plasma temperature is at least two orders of magnitude above that of the neutral particles (room temperature) as shown in figure 3.1 the pressure term of the plasma thrust in equation (4.1) shall still be one order of magnitude higher than that of the neutral pressure term. For the momentum term, the neutrals are generally considered to have the sonic velocity at the outlet[57] and the Bohm speed, $v_B = \sqrt{\frac{qT_e}{M_i}}$, for the plasma particles at the outlet[46]. The Bohm speed lies roughly one order of magnitude[39]

above that of the regular sonic speed, thus also causing the plasma momentum term in equation (4.1) to be at least one order of magnitude larger than that of the neutral momentum term. Therefore, for APTs in general, the neutral thrust shall at least be one order of magnitude smaller than that of the plasma thrust, and is neglected in the further derivation of the thrust.
When assuming cold heavy species with negligible temperature and thus negligible static pressure, and negligible electron inertia due to their low mass, the thrust given by equation (4.1) can be simplified to:

$$F = \int_A (p_e + m_i n_i u_{iz}^2) dA \tag{4.5}$$

Considering that the plasma axial momentum flux is driven by the ions and electrons, the thrust can be further derived from the ion and electron momentum equations. In steady state for $I = i, e$, these are:

$$m_I \nabla (n_I \mathbf{v}_I \mathbf{v}_I) = q_I n_I (\mathbf{E} + \mathbf{v}_I \times \mathbf{B}) - \nabla p_I \tag{4.6}$$

When again assuming cold ions with negligible temperature and thus negligible static pressure, negligible electron inertia due to their low mass, and also assuming negligible radial ion inertia as the ions are considered unmagnetised, and quasi-neutrality ($n_e \approx n_i = n_p$), the momentum equations in an axi-symmetric cylindrical coordinate system become[5]:

$$-e n_p (E_r + v_{e\theta} B_z) = \frac{\partial p_e}{\partial r} \tag{4.7}$$

$$-e n_p (E_z + v_{e\theta} B_r) = \frac{\partial p_e}{\partial z} \tag{4.8}$$

$$e n_p (E_r + v_{i\theta} B_z) = 0 \tag{4.9}$$

$$e n_p (E_z - v_{i\theta} B_r) = \frac{1}{r} \frac{\partial}{\partial r} (r m_i n_p v_{ir} v_{iz}) + \frac{\partial}{\partial z} (m_i n_p v_{iz}^2) \tag{4.10}$$

Combining equations (4.8) and (4.10) to remove E_z gives:

$$e n_p (v_{e\theta} - v_{i\theta}) B_r - \frac{1}{r} \frac{\partial}{\partial r} (r m_i n_p v_{ir} v_{iz}) = \frac{\partial}{\partial z} (p_e + m_i n_p v_{iz}^2) \tag{4.11}$$

Note that the axial derivative of the momentum flux is obtained on the right hand side (RHS). The first time on the left hand side (LHS) is the axial Lorentz force generated from the combination of a radial magnetic field B_r and the azimuthal current $J = e n_p (v_{e\theta} - v_{i\theta})$. As shown in figure 4.3, inside the the axial magnetic field, the charged particles will gyrate due the Lorentz force while moving in the axial direction[44], creating an azimuthal current. When the magnetic field diverges and has some radial outward component, this then also provides an axial component to the Lorentz force F_z, as the charged particles have a azimuthal movement besides their axial movement. The second term on the LHS refers to axial momentum losses of ions hitting the source walls.
Substituting in equations (4.7) and (4.9) into the azimuthal current, placing the result in equation (4.5) and integrating over the azimuthal angle θ yields the following equation:

$$F_{thrust} = F_{cham} + F_{mag} + F_{loss} \tag{4.12}$$

$$F_{cham} = 2\pi \int_{r_s} r p_{e0} dr \tag{4.13}$$

$$F_{mag} = -2\pi \int_z \int_{r_p} r \frac{B_r}{B_z} \frac{\partial p_e}{\partial r} dr dz \tag{4.14}$$

$$F_{loss} = -2\pi \int_z \int_{r_p} \frac{\partial}{\partial r} (r m_i n_p u_r u_z) dr dz \tag{4.15}$$

F_{cham} originates from the integration constant and as shown in figure 4.3 it represents the static electron pressure pushing against the back plate inside the source, using the maximum source pressure p_{e0}. It thus forms the basic, initial source chamber thrust.
F_{mag} is the volume integral of the Lorentz force F_z due to the radial magnetic field B_r and the azimuthal current, which is given by $e n_p (v_{e\theta} - v_{i\theta}) = \frac{1}{B_z} \frac{\partial p_e}{\partial r}$. The F_z component for a single point in space is

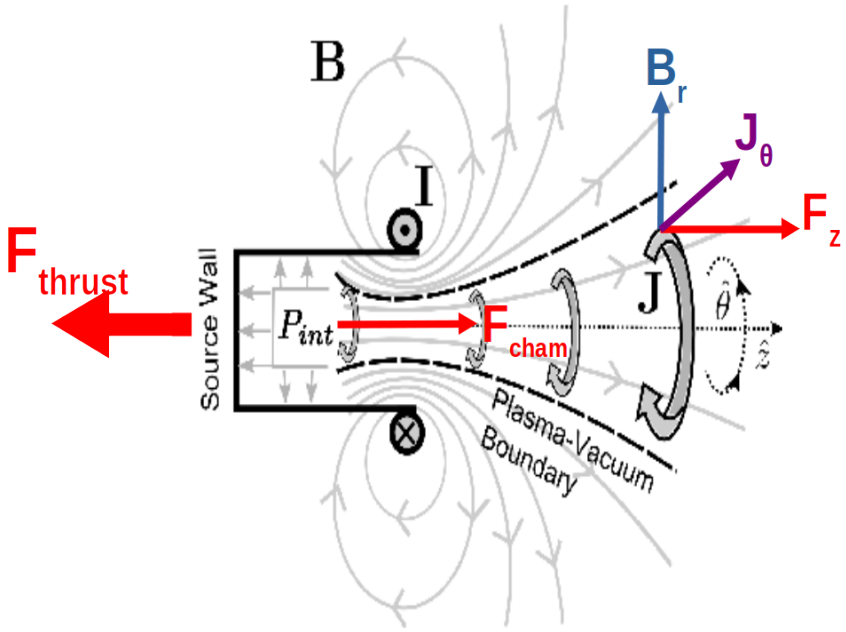

Figure 4.3: Physical picture of the thrust imparted by the plasma exhausted from the rocket[63] with B the magnetic field, I the coil current of electromagnet and J the azimuthal current of charged particles. The total plasma thrust F_{thrust} is a result of the chamber pressure imparted plasma thrust F_{cham} and the diverging magnetic field pressure generated by the Lorentz force on the charged azimuthal currents in the nozzle, which amounts to F_z when integrated over the nozzle volume.

shown in figure 4.3 as well. This phenomena converts the remaining radial electron pressure into axial plasma momentum, thus increasing the axial momentum flux. The total thrust of an APT can increased by roughly $40 - 70\%$[52], [57] through the effect of the diverging magnetic nozzle. This is purely a conversion of internal particle energy to kinetic axial energy, as no work can be done by the Lorentz force due to its orthogonal direction to the particle's velocity.
F_{loss} is the ion axial momentum lost to the source walls. It is common in thruster modeling to assume this loss to be negligible due to the magnetic shielding of the walls in the source chamber[55]–[57], this assumption will be kept in place during this thesis work.

Besides the thrust and specific impulse, three efficiencies denoting the thruster's use of propellant and power complete the characterization of the propulsive performance. The production efficiency η_p and propellant utilization η_u characterize the efficiency of use of the plasma for propulsion. They are denoted as the ratio of ion mass flow out of the chamber exit over the entire mass flow of ions created through ionization and the ratio of ion mass flow out of the chamber exit over the injected propellant mass flow respectively:

$$\eta_p = \frac{\dot{m}_{i_{exit}}}{\dot{m}_{i_{created}}} \tag{4.16}$$

$$\eta_u = \frac{\dot{m}_{i_{exit}}}{\dot{m}} \tag{4.17}$$

The thrust efficiency η gives the ratio of the output mechanical jet power to the required input power:

$$\eta = \frac{P_{jet}}{P_{in}} = \frac{F^2}{2\dot{m}P_{in}} = \frac{\frac{1}{2}\frac{M_W}{N_A}v_e^2}{\frac{1}{2}\frac{M_W}{N_A}v_e^2 + e_I + e_L} \tag{4.18}$$

Where P_{in} represents the input power to the thruster, M_W is the molecular mass of the propellant and N_A is the Avogadro constant. Furthermore, e_I is the ionization potential and e_L represents all other losses of energy within the thruster system. Even if the losses inside the source chamber to the side-walls are made negligible due to a very strong axial magnetic field screening, only half of the plasma will leave the chamber and carry the ions momentum with it, resulting in a maximum production efficiency of 50%. The other half of the total ion momentum is lost at the back-wall. This can be prevented by also screening the back-wall with a magnetic field, requiring a more special complex configuration of

the magnetic circuit, and would lead to almost a 100% production efficiency[52]. Simple model designs often omit this back-wall screening. As the amount of thrust due to the neutral gas is considered near-negligible[57], it is preferred to have a propellant utilization nearing unity to also obtain a better thrust efficiency, as less of the potential energetic thrust is wasted per unit of mass flow.

4.4. Propellant

The HPT is able to perform with many different propellants and is able to switch between propellants within the same design, changing only the operating pressure[60]. Some of the tested and proven propellants include: xenon[6], [64], argon[6], [65], iodine[7], hydrogen[6], nitrogen[6], [60], methane, ammonia and nitrous oxide[60].
equations (4.2) and (4.4) show that if one wishes to increase both the thrust and specific impulse, the equivalent exhaust velocity must be increased. For chemical rockets, the energy available for thrust generation is limited by the chemical bonds inside the chosen propellant which limits the maximum achievable equivalent exhaust velocity to 5500m/s[13]. Therefore, is preferable for chemical propulsion systems to use a propellant with light molecular mass so that a high equivalent exhaust velocity can be achieved with the same amount of input energy. By contrast, in electric rockets the propellant is accelerated to the equivalent exhaust velocity v_{eq} with energy originating not from the propellant itself but from an external source such as a solar panel, battery or power cell. Due to this, electric rockets can use higher energy power sources enabling them to obtain much higher exhaust velocities and specific impulses than chemical rockets.

It can be seen from equation (4.18) that for EP applications the only propellant characteristics influencing thrust efficiency are the molecular mass and ionization potential. Additionally, a propellant with a high molecular mass will have fewer particles per unit of mass to be ionized. Combined this with a low ionization potential such a propellant will then require less power per kg of propellant to ionize, while still providing a high thrust efficiency. Thus a propellant consisting of molecules with high molecular mass and low ionization potential is preferred. Generally the choice is further limited to mono-atomic propellants as molecular propellants need to be broken up first in fragments before ionization and will take up wasted energy in rotational and vibrational modes during ionization[66]. Finally, a high cross section is also preferred, as that will result in more collisions, increasing the degree of ionization of the propellant while in the source chamber[13]. Besides these propulsive aspects, the choice will also be influenced by additional considerations such as ease and density of storage and temperature management as well as toxicity, radio-activeness and cost. Propellant management is important as regardless of its storage state, the propellant must be in a gaseous form when entering the HPT source chamber such that the RF power can be deposited into it and it can expand freely[7].

table 4.1 shows a range of propellants that has been used in various EP applications and the associated performances, collected by Mazouffre(2016). From this, it can be seen why xenon is currently the industry standard: it has a high molecular mass and low ionization potential, low toxicity and can be stored as a high-density liquid or supercritical gas. At the same time, Mazzoufre(2016) identified three other promising propellants. First, krypton has a high attainable specific impulse but lower storage density and cross section. Second, bismuth possesses a high mass and storage density as well as low cost and ionization energy but has the caveat of needing to be maintained at a high temperature to prevent condensation. Third, iodine which, despite being a molecular propellant, has an equal thrust efficiency to xenon due to its low ionization potential, low disassociation energy of 1.57 eV and high cross section and mass. Additional considerations are the higher storage density of iodine and its much lower cost, against the drawback that it is a highly reactive substance and therefore requires additional design considerations[13]. Finally, argon is also frequently considered for use in EP, stemming from its wide applications in other areas in the plasma research field as it is far cheaper than xenon. However it is also lighter, has a smaller cross section and a higher ionization potential. This all causes the degree of ionization being much lower than xenon (30%-40% as opposed to 90%)[67], resulting in a poor propellant utilization. As it is much cheaper, research is being conducted into improving its performance for EP purposes[67], [68]. Alkali metals such as Lithium and Caesium, boasting high molecular mass and low ionization energy are also considered but face drawbacks due to the ease of condensation[69]. Finally, for very high specific impulses, hydrogen is of interest due to it possessing the lowest molecular mass possible. For example, tests with a Magnetoplasmadynamic thruster with

Table 4.1: Properties of various propellants for electric propulsion[13]. E_I refers to ionisation potential.

Propellant	Mass (amu)	E_I (eV)	State	Vapor pressure (Pa)	Melting/ boiling point ($^\circ C$)	Toxicity	Cost
He	4.0	24.6	Gaseous	-	-272/-269	Low	Low
Li	6.9	5.4	Solid	10^{-6} (500K)	180/1342	Medium	Low
Ar	39.9	15.8	Gaseous	-	-189/-186	Low	Low
Kr	83.9	14.0	Gaseous	-	-157/-153	Low	High
Xe	131.3	12.1	Gaseous	-	-112/-108	Low	Very high
Cs	132.9	3.9	Liquid	3×10^{-4}(300K)	29/685	Low	Very high
Hg	200.6	10.4	Liquid	0.4 (300K)	-39/357	High	Low
Bi	209.0	7.3	Solid	0.5 (900K)	271/1564	Medium	Low
I_2 (I)	253.8 (126.9)	9.4 (10.4)	Solid	40 (300K)	114/184	Medium	Low

a cathode have measured an I_{sp} of 10,000s[70].

The previous propellant considerations hold for all electric propulsive systems in general. An APT then distinguishes itself from other EP systems in that it should be able to handle all of the aforementioned propellants due to its simplicity and cathodeless design. The advantages of the aforementioned flexibility in propellant operation are as follows: first, it allows for more freedom in design. Considering the density and performance of different propellants, the propulsive performance can be maximized as described above. Being able to utilize other propellants than the commonly chosen and well-performing xenon also decreases the cost of operation, and increases the operational availability of the thrusters. Furthermore, as multiple propellants can be chosen from, one can consider propellants which are safer and easier to handle on ground. Finally, the ability to switch propellants 'on the go' allows a large degree of operational freedom while in-space. This can range from less restrictive limitations on potential in-space-refueling, to extended lifetime as different types of propellant are used in different order. Substances in the spacecraft with a non-propellant primary purpose, in cases of emergency, or after having served their initial purpose, can be used for propulsive needs. Likewise, substances which result as a byproduct of another process could also be used as propellants. Conversely, some propellant substances can be used for non-propellant applications on board too, routinely or in cases of emergency. For example, hydrogen, besides its functioning as an energy-carrier, can be produced as a by-product when creating oxygen on-board from water, but it can also be a required substance for the creation of water instead.

4.5. Current HPT performance

Characterizing the performance first in terms of thrust and specific impulse, the achieved thrust levels of HPTs generally falls in the mN range, while the specific impulse varies between a few hundred seconds to a few thousands of seconds[5]. Taking argon as a propellant,the maximum obtainable specific impulse (Isp) of HPTs has been modeled to fall in the range of 1000 to about 3000 s[52], [61]. Experimentally, the highest Isp measured for argon has indeed been $3256\,\mathrm{s}$[5]. Commercially available thrusters have, as expected, demonstrated a lower specific impulse and thrust of $600\,\mathrm{s}$ and $0.60\,\mathrm{mN}$ at $50\,\mathrm{W}$ of power[7]. An Isp of $5000\,\mathrm{s}$ has been reported by the High Power Helicon plasma thruster under development by MSNW and the University of Washington when operating at high power levels of 20-50 kW with hydrogen[6]. Going further into the high power level of HPTs, NASA is developing a special combination of HPT and ECRT, the VASIMR engine, which aims at a thrust level of 6 N and Isp of $2000\,\mathrm{s}$, requiring a comparatively very high power input of 200 kW, having reached a maximum of 4.4N with a power input between 100-150 kW so far[71]. It is important to realize that these high power levels are currently not realistic to accommodate on ordinary spacecraft designs, requiring very large power plants or solar panels on the scale of the International Space Station, or novel solutions[14]. For this reason, this review focuses primarily on low power HPTs, which are more readily powered in space.
Currently achieved performances for efficiencies have production efficiency nearing 100% but propellant utilization remaining around 20%[40]. Experimental measurements of thrust efficiency of operational thrusters have mostly remained under 6%[7]. Multiple models have shown the main reason for this poor thrust efficiency to be due to large wall and ionisation losses inside the source chamber, having modeled maximum theoretical efficiencies between 20% and 30%[40], [52], [57], [61]. Recently, a maximum thrust efficiency has approached 30%[8] at a high power of $6\,\mathrm{kW}$.

5

Theory and Regimes

This chapter provides a more in-depth look at the fundamental plasma flow theory used in relevant models for EP thruster behavior. To be able to describe the state of a system in time, such as a plasma in transport, and to predict its state in the future by describing the change over time, a dynamic theory is required. Different levels of theory exist, starting from first principles for low level theories and becoming more ever more simple in high level theories, meaning that approximations are made in order to simplify associated calculations under certain circumstances. There are, however, different types of circumstances influencing the behavior of a flow to such a degree, that a precise dynamic theory becomes too complex to solve, and a simplified theory may no longer apply. It is thus important that the application of a specific level of theory on a phenomena to be modeled is justified to the behavior, or circumstances, of the studied physical phenomena. These levels of theories and the associated circumstances, referred to as regimes, will be covered in this chapter. First the applicable levels of mathematical theory governing different models will be covered in section 5.1 to substantiate how the models covered in chapter 6 approach the plasma. section 5.2 defines the regimes in an APT in which the specific levels of theory hold. section 5.3 concludes with the important phenomena of regime transition experienced within an APT.

5.1. Definition of Underlying Mathematical Theory Levels

A dynamic theory should prescribe the state of the system through a set of variables, including equations for the time derivatives of said variables[47]. For general plasma transport Choudhuri(1998) categorises mathematical theories for fluids and plasmas into three main levels seen in table 5.1. Depending on the level of theory that one uses, a system of N particles can be considered either as a collection of N distinct particles, or as a continua. The appropriate level to be used depends on specific criteria. Choudhuri(1998) describes the associated criteria for moving between levels. Only the criteria for the Plasma versions Level 2 and Level 3 will be considered here, as they apply to the most relevant plasma models, being those of plasma kinetic (distribution function) models and plasma fluid (continuum) models. In later chapters, the plasma designation will often be omitted and the neutral models themselves will not be covered here for brevity. They are described separately by Choudhuri(1998) and are other textbooks in the field of general (fluid) dynamical modeling.

It is important to note that compared to the theoretical mathematical models for the neutral fluids, fully satisfactory theoretical mathematical models of the plasmas that are applicable to all situations have not yet been achieved due to the significant challenges of incorporating into the equations of motion both the non-straight motion between collisions of the particles under magnetic fields and externally and internally imposed electric fields. An additional challenge is that plasmas are not in complete thermodynamic equilibrium when spatially inhomogenous. Therefore, additional assumptions need to be made, as described by Choudhuri(1998).

Table 5.1: Different levels of theory for neutral fluids and plasmas[47]

Neutral fluids		
Level	Description of state	Dynamical equations
0: N quantum particles	$\phi(\mathbf{x}_1, ..., \mathbf{x}_N)$	Schrödinger's eqn.
1: N classical particles	$(\mathbf{x}_1, ..., \mathbf{x}_N, \mathbf{v}, ..., \mathbf{v}_N)$	Newton's laws
2: Distribution function (Kinetic model)	f(**x**,**v**,t)	Boltzmann eqn.
3: Continuum (fluid) model	$\rho(\mathbf{x}), T(\mathbf{x}), v(\mathbf{x})$	Hydrodynamic eqns.
Plasmas (Levels 0 and 1 same as above)		
Level	Description of state	Dynamical equations
2: Distribution function (Kinetic model)	f(**x**,**v**,t)	Vlasov eqn.
$2\frac{1}{2}$: Two-fluid model	-	-
3: One-fluid model	$\rho(\mathbf{x}), T(\mathbf{x}), v(\mathbf{x}), \mathbf{B}(\mathbf{x})$	Magneto-hydrodynamic eqns.

The governing equations of these levels and their derivations are readily shown from different starting points in textbooks on plasma physics such as those by Bittencourt(2004), Choudhuri(1998), Chen(2016) and Lieberman(2005) but the higher levels cannot be represented by one unique model for all situations per level. However, there is a general consensus on the ranges in which to apply the specific subsets of these models[43]–[45], [47]. Furthermore, Crestetto, Deluzet & Doyen(2020) have defined a clear bridging framework between the kinetic plasma description and low-frequency single-fluid models starting from formulations of the Vlasov equation and ending with the magnetohydrodynamic (MHD) equations, between which multiple hybrid levels are defined. Their work also identifies a set of parameters that explain the transition between theory levels[72]. For brevity, the derivations will not be repeated here, only the governing equations relevant to subsequent HPT models will be given during their description. First the relevant levels will be described in more detail.

5.1.1. Level 2: Plasma Kinetic theory

Level 2 is utilized when N is too large for realistically solving all the individual equations of motion (EOMs) for each particle. It consist of statistical mechanics approaches and Lagrangian approaches. Both require a PDF $f(\mathbf{x}, \mathbf{v}, t)$ to provide the particle number density n in the six-dimensional phase-space at time t, the former describing the evolution of the PDF directly and the latter describing the motion of grouped macro-particles in order to construct the PDF. Hence the kinetic theory loses the information on individual particles and instead describes a generalised distribution or information of grouped particles.

The statistical mechanics approach in general uses the Vlasov equation as the dynamical equation, which is an adapted version of the Boltzmann equation for a neutral kinetic gas model. The Boltzmann equation describes in a neutral gas model the change of the PDF $f(\mathbf{x}, \mathbf{v}, t)$ in time, space and velocity[43]:

$$\frac{\partial f_k}{\partial t} + \mathbf{v} \cdot \nabla_x f_k + \mathbf{a} \cdot \nabla_u f_k = \left(\frac{\partial f_k}{\partial t} \right)_{coll} \tag{5.1}$$

Where **a** is the acceleration of species k, being the result of $\mathbf{a} = \frac{F_k}{m_k}$ where F is the force acting on the particles of species k. $\left(\frac{\partial f_k}{\partial t}\right)_{coll}$ is the time rate of change of the PDF due to collisions and can be represented by multiple models such as the *Krook*, *Boltzmann collision integral* or *Fokker-Planck* models[43], [44]. The Vlasov equation generally neglects the binary collisions accounted for in the Boltzmann equation and instead considers collisions due to the Coulomb force. It can however consider these collisions through a relaxation to the thermodynamic-equilibrium, referred to as the *Vlasov-Bhatnager-Gross-Krook* or *Vlasov-BGK* model. The general form is given by:

$$\frac{\partial f_k}{\partial t} + \mathbf{v} \cdot \nabla_x f_k + \frac{q}{m_k}(E + \mathbf{v} \times \mathbf{B}) \cdot \nabla_u f_k = Q_k \tag{5.2}$$

where Q_k is a collision operator, for example the Bhatnager-Gross-Krook operator thus used to account for a collisional process, even for non- or weakly- collisional processes[72]. Relaxation from a non-equilibrium to a thermodynamic equilibrium state through collisions of particles, in which thermal energy

is spread throughout the particles by kinetic energy exchange, is often neglected. These models can then describe perturbations in the plasma on timescales shorter than the relaxation, but not describe any relaxation behavior back towards the equilibrium state. They still allow analysis of the downstream ion and electron heat fluxes and the response to non-Maxwellian PDF when applied to a plasma plume, which is not possible with higher levels[4]. Should non-Coulomb collisions be deemed important, the more complicated models such as the Vlasov-BGK with a non-zero collision operator are required. The criteria for Level 2 for plasmas are the following[47]:

- The system has many particles moving under the Coulomb force, producing mostly small deflections in the trajectories. The Vlasov equation instead of the Boltzmann equation is then used.
- The volume of the system should be close to neutral charge.

An other approach to kinetic theory is presented by Lagrangian methods where each particle is tracked. For the case of modeling HPTs, this is represented by the Particle-in-Cell method. As tracking each individual particle would be too complex, the particles are instead grouped into macro-particles. These macro-particles consist of distinct particles which are expected to behave in the same manner. Ideally, they accurately represent only particles with the same properties, but due to the heavy associated computational costs, macro-particles might include other particles that are deemed similar enough to simplify the equations. The EOMs of these macro-particles under the influence of an electromagnetic field are then solved. Collisions can be accurately accounted for by the inclusion of Monte-Carlo methods[4]. The PDFs are calculated from the resulting bulk plasma particle model at all locations and are then used to average any macroscopic properties of the plasma flow not obtained directly from the bulk[73]. By foregoing the statistical mechanics approach the PIC-method can in theory present a much more appropriate theory of modeling the physics, although it is prone to simplification by grouping larger groups of separate particles into macro-particles due to the complexity of solving for all (or nearly all) N single particles, which is the reason for the existence of Level 2 and 3 in the first place.

5.1.2. Level 3: Plasma fluid theory

While level 2 descriptions are more precise in representing the physics of various phenomena, solving the kinetic equations when many collisions occur, which is the case at thermodynamic equilibrium, is associated with high computational costs, often leading to simplified Level 3 models being preferred. Level 3 is utilized by describing the state of the plasma with 4 variables everywhere throughout the plasma: two thermodynamic variables, $\rho(\mathbf{x})$ and $T(\mathbf{x})$, $\mathbf{v}(\mathbf{x})$ to impose approximate thermodynamic equilibrium to the fluid, and $\mathbf{B}(\mathbf{x})$ to account for the embedded magnetic fields in plasma. The accompanying set of equations, which is an altered version of the fluid hydrodynamic equations for continuity, momentum, and energy, imposed by the addition of $\mathbf{B}(\mathbf{x})$ is referred to as the MHD equations. As it does not neglect binary collisions, rather assuming them to be large[72], the (near) Maxwellian distribution is maintained in equilibrium and a relaxation to this thermodynamic equilibrium can be described by the MHD equations.
The criteria for Level 3 for plasmas are[47], [72]:

- Frequent collisions keep the PDF $f(\mathbf{x}, \mathbf{v}, t)$ in local regions close to the Maxwellian distribution, meaning that these local regions have the properties of a system in thermodynamic equilibrium. This is similar to how in a neutral gas the hydrodynamic model applies when the PDFs are close to Maxwellian. The frequent collisions are obtained by ensuring the gyroradius r_L of a charged particle, and the mean free path λ of a neutral particle are smaller than the length scale L (equal to the vanishing of the Knudsen number).
- Furthermore, the length scales should be longer than the Debye length and time scales larger than the inverse of the plasma frequency to neglect charge separation and EM wave propagation in the plasma. Such a system is known as a fluid, or for plasma, a magnetofluid.

5.1.3. Level $2\frac{1}{2}$: Two-fluid theory

For the case in which internal electric fields in the plasma are significant and will cause a difference in the behaviour of positively and negatively charged particles, associated with time scales marginally larger than the inverse of the plasma frequency, Level $2\frac{1}{2}$ exists[44], [47]. This considers the flow as two or more fluids, often split between heavy or light species as well as their charge. These are linked through the charge potential they cause by their respective currents[52]. Beyond this the dynamics are

generally those of a 1-fluid model, with plasma chemistry reactions acting as source and sink terms for each fluids particle density.

5.2. Regimes

During the transport of the plasma in a HPT from its location of production to the ambient space far away from the thruster, the plasma flow undergoes multiple changes in its characteristics and scale. Some of these changes to its properties, or changes in the scale at which the plasma is observed, are so significant that the dominant physics influencing the behavior of the plasma also changes, requiring a change in the dynamic theory with which the plasma is best described. Hence the theories are classified to be valid in different 'regimes', depending on the different circumstances of the flow. Relevant for the modeling of a thruster are the 'fluid' and 'kinetic' regime. In fluid dynamics, fluid mechanics are used in the fluid regime and statistical methods are used in the kinetic regime. These regimes are linked to criteria set upon the circumstances that the plasma finds itself in as described in section 5.1, and can occur at any spatial location as long as those circumstances are met. Only one regime can be present at each point in space and time, as the regime is defined by whichever physical behaviour is dominant over the others at that point in time and space. A plasma can be in a certain regime in one or more regions of a system, and in another regime in other regions of said system. During steady-state operation of a thruster, it is expected that the regions in which the plasma is in a certain regime, do not change with time.
Within fluid dynamics, one can classically differentiate between these regimes by determining how rarefied the flow is with the Knudsen number K_n. It is given by the ratio of the molecular mean free path length λ to characteristic length scale L or by the inverse of the number of collisions during a typical time. A K_n that is approaching 1 implies that the fluid continuum assumption is not valid, denoting a shift into the kinetic regime and requiring its associated theories. In fluid dynamics, the transition from a low Knudsen number regime to Knudsen number near to or greater than 1 is a complex field of study and fluid assumptions can already be said to stop being entirely valid in the range of $K_n \approx 0.01 - 0.1$. For plasma physics where the fluid dynamics models require inclusion of long distance Coulomb forces, this is even more-so the case. Here the Knudsen number can be based upon the ion collisions[72] but is not necessarily enough as a sole criterion for determining a change in regime.
The applicable criteria for the fluid and kinetic regime are described in [47], [72] and have been summarised in section 5.1

5.3. Transition Between Regimes

Inside the source chamber section of the APT the plasma is most commonly taken to be in the fluid regime, due to the large amount of physical binary collisions between the particles maintaining a (near) thermal equilibrium. Later, inside the magnetic nozzle section, two phenomena occur which make the validity of a full-fluid model difficult at best to maintain and have caused many authors to suggest kinetic models for the magnetic nozzle section[4]. These two phenomena are the rarefaction of the plasma and a separation of charge.
Firstly, after exiting the enclosed source chamber on the open end, the plasma can suddenly expand into free space, although still being constrained by the diverging magnetic field. The resulting rapid expansion causes the flow to become rarefied, its density dropping between one and two orders of magnitude compared to what it was in the source chamber[2]. This affects the Knudsen number as denoted section 5.2, meaning the mean free path of motion increases to such a degree that it becomes comparable to the characteristic length of the system, resulting in very few non-Coulomb collisions and thus presenting one criteria for a kinetic model over the fluid model.
Secondly, a separation of charge takes place perpendicular to the axial flow direction, denoted by a large potential drop: ions with their much larger inertia are much less magnetized than electrons, to the point that many models consider them as unmagnetised particles[9], [74]. The order of magnetization here is given by the ratio of a characteristic length L, taken to be that of the nozzle, to the particle's cyclotron radius, which is given by equation (3.6). In effect, the electrons, being very magnetized, will tend to follow the diverging magnetic field lines while the ions stay on their own course, unguided by the field lines. This course will be largely axial with some radial regular diffusion occurring as well. This causes the ion's number density to decrease locally along the beam much slower than that of the electrons and hence a separation of charge occurs shortly after the magnetic field starts to diverge.

Hence, after the potential drop, there is neither a local thermodynamic equilibrium nor a quasi-neutrality that holds, thus removing the criterion for a (full) fluid model and necessitating a kinetic model for the plasma flow. Even further downstream, the plasma expansion will be driven by thermal pressure and ambipolar diffusion[9]. Therefore, the transition to a rarefied plasma and the occurrence of a potential drop, are the strongest candidates so far for defining the transition from the fluid to kinetic regime. This transition does not occur necessarily at the boundary between these sections, it occurs wherever the circumstances of the state of the plasma cause the criteria of the fluid regime to no longer be met, and instead, the criteria of the kinetic regime to hold. The exact transition in plasma, if driven by the aforementioned rarefaction and charge separation is, however, not yet well-understood, and there is no current consensus in literature regarding either a consistent theory for the physics at play describing the transition, its specific criteria, or a numerical solution for modeling what happens. Promisingly, the work of Singh(2011) and Crestetto, Deluzet & Doyen(2020) recently provided insight into the physics at play[41] and many intermediate models and criteria to bridge this transition[72].

6

Ambipolar thruster modeling

By choosing a theory level appropriate to the regime hypothesized or measured in a section of an APT, specific models can be constructed. They can implement this theory through analytical or numerical means. It is not realistic in scope to describe, analyze and evaluate each and every model in the field of EP modeling. Therefore this chapter summarizes the findings of a preceding literature study which investigated the state of the art in the modeling of multi-regime APT[38]. Specific attention will be given to limitations found in relevant models: the coupling methods considered further on in this thesis strive to reduce these limitations.

6.1. Different models as divided by applicable section

Almost all models currently in use are meant to be applied only to a specific section of the thruster and not to the thruster as a whole. To predict the performance of the whole thruster, a global model is often used as stand-in for the missing section, or another model is used separately. The most common reason for this approach is pragmatic: as the plasma density from source to plume drops from $n \approx 10^{20}$ to $n \approx 10^{18}$, employing a kinetic approach in the very high density region of the source chamber brings with it too heavy a computational cost, whilst a fluid model would suffice. A few special hybrid models do exist however, which model the entire thruster with separate models for the heavy and light species[40]. Another possible approach to model the entire thruster faithfully, while efficiently making use of the fluid regime in the source chamber, is to couple a fluid model applied to the fluid regime together with a kinetic model applied to the kinetic regime. Early work on this has been conducted by the universities of Bologna and Padova[9].

It is important to realize that while models of a certain level are often consistently applied to a defined section of the geometric domain of the thruster, relating the fluid regime to the source chamber and the kinetic regime to the magnetic nozzle, is an oversimplification. The terms source chamber and magnetic nozzle only refer to geometrical sections, and do not necessarily correspond exactly one-to-one to with the appropriate physics regime in these sections. For example, fluid behavior, according to Choudhuri's(1998) Level 3 criteria from table 5.1, is still possible in the area of the diverging magnetic field that is in the very close neighborhood of the throat boundary, as shown in figure 6.1. This is because the regime transition simply depends on a combination of criteria not solely equal to the exact location of the geometric throat, described in more detail in section 5.3. While it is believed that staying faithful to the regimes' actual locations should provide a more accurate model of the phenomena occurring, the degree to which neglecting the realistic locations of these regimes near the transition point, and instead utilizing the geometric boundaries between sections instead, has not yet been studied sufficiently. It is unknown how this affects the simulation output accuracy when compared to real test data.

6.2. Fluid models

Fluid APT models describe the plasma as a continuum, in terms of the continuity, momentum and energy equations, most often including Poisson's equation for the potential in the plasma. These models

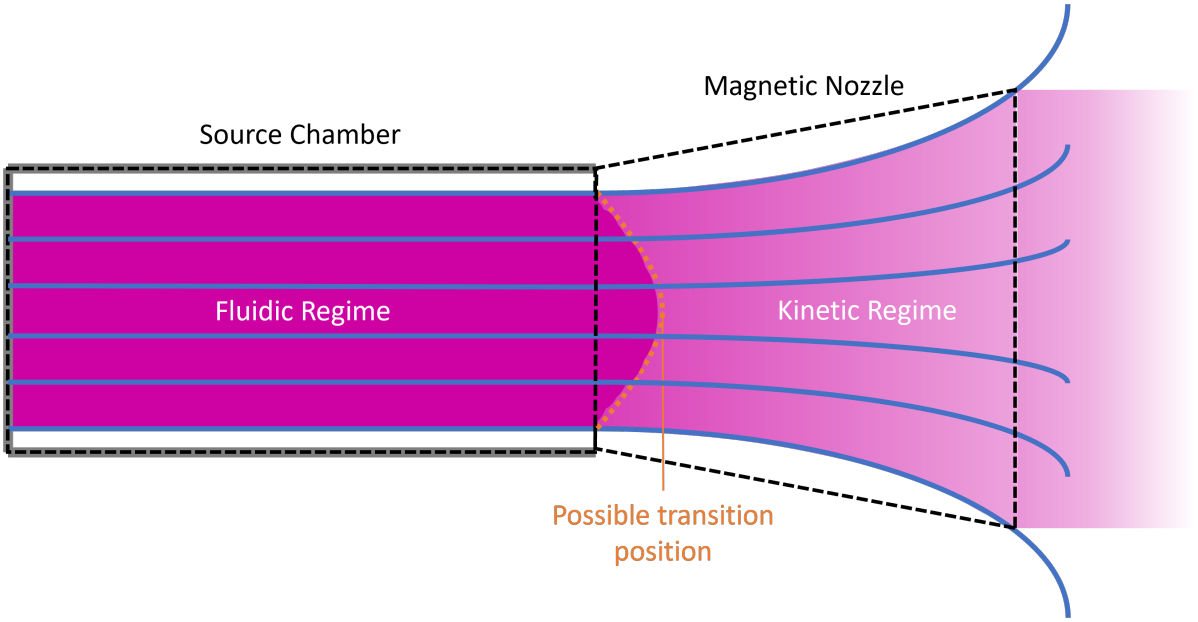

Figure 6.1: The fluid regime or domain does not necessarily exactly fit to the geometric domain of the source chamber. Author's own work

assume that due to many local collisions, local thermodynamic equilibrium exists, giving a Maxwellian PDF to all particles. Furthermore, ions are often assumed cold while electrons are considered isothermal to simplify the energy equation. Fluid models can range from analytical or simple semi-analytical for preliminary analysis of the whole thruster[57], to more complex numerical codes[2], [3], [51], [75]. The more complex numerical models can be 2D or 3D and give higher-fidelity results and better insight in the plasma transport through the APT source chamber. These models can include a coupling to EM models[42], [76] to accurately compute the deposited power profile from the surrounding antenna, and if not coupled they assume a deposited power density profile or total deposited power. They are generally only applied to the source chamber of the thruster as the plasma flow enters the kinetic regime outside the source chamber. A frequent fundamental assumption for these models is that the Bohm criterion[44] holds at the outlet of the source chamber, imposing an assumed sonic throat velocity there[77].

6.3. Kinetic HPT models

The kinetic APT models do not assume PDFs for the species. Instead they uniquely construct the PDF, allowing for non-Maxwellian PDFs and are thus able to model non-local equilibrium plasma behaviour, which is prevalent in the rarefied plume of the plasma flow inside the magnetic nozzle[34]. Two approaches to kinetic models exist. The first uses the Vlasov equation which solves the evolution of the PDF in time and space[72]. After this the PDF is integrated to obtain macroscopic properties of the plasma as explained in chapter 3. The second directly solves the equations of motion (EOMs) of macro-particles, consisting of groupings of single particles[4]. The resulting distribution and evolution of these macro-particles are then used to construct the PDFs which are again used to obtain macroscopic properties. The kinetic approach is dependent on fewer assumptions than the fluid approach, although interface assumptions such as sonic conditions at the throat often persist[4]. For using the Vlasov equation, it is generally assumed that collisions are only long-distance in nature, unless an operator is included to also account for normal collisions, such as the Bhatnager-Gross-Krook operator[72]. The PIC method often accounts for non-Coulomb collisions through Monte-Carlo methods, resulting in a very accurate model with very few problematic assumptions. However, PIC results often include much numerical noise, which requires time-averaging to filter out. While yielding more accurate models, applying kinetic theory to the plasma flow results in much larger computational costs when the number of particles and their collisions increase. Inside the source chamber this makes applying the kinetic model for all particles unpractical[9], [40].

Table 6.1: Relative expectations of presented models performance. Note: 3DV, 3DV-Sfsh and MS stand for 3D-VIRTUS, 3D-VIRTUS-Starfish and Martinez-Sanchez respectively

Applicable area	Model	Dynamical Theory	Accuracy	Computational Cost	Benefits	Limitations
Full thruster	Lafleur[57]	fluid	Low	Low	Simple preliminary analysis	Oversimplifies entire thruster to a 1D fluid
	3DV-Sfsh[9]	fluid-Kinetic coupled	Medium-High	High	Good results, appropriate regimes	Long run time and sub-optimal coupling
	HYPHEN[40]	fluid-Kinetic hybrid	Medium-High	Medium-High	Good results at low cost	Considers electrons as fluid in rarefied plume
Source chamber	Lafleur[57]	fluid	Medium	Low	Simple preliminary analysis	Simplifies plasma as 1D and fluid everywhere
	3DV[2]	fluid	High	Medium	2D-axisymmetric, RF power coupling	Assumes all particles to be fluid everywhere
Magnetic nozzle	Lafleur[57]	fluid	Low	Low	Simple preliminary analysis	Considers entire rarefied plume fluid
	MS[36]	Kinetic-statistical	Medium	Medium	Low computational-cost kinetic model	Neglects particle EOMs, solves PDF instead
	Starfish[4]	Kinetic-PICC	High	High	considers distinct macro-particle EOMs	Large computational cost or simplify macro-particles more

6.4. Hybrid and coupled multi-regime APT models

As stated, the three main approaches to model a thruster entirely have been to either model it in separate parts[74], to model the entire thruster with a hybrid model[40], or to separate the entire thruster according to the relevant regimes, but strongly couple together the fluid and kinetic models applied on these regimes[9]. This third approach is referred to as a coupled multi-regime model in this work. The first approach is de facto the separate use of previous discussed models. The results or input from or for a fluid or kinetic model are fed into or obtained from another model, often a simple global one. In this case the accuracy and validity of the found solution depends heavily on the assumed boundary conditions (BCs) of each separated model.

The second, hybrid approach is where multiple separate models are used at the same point in space and time, but for different species. As there are no boundaries that are crossed with differently imposed assumptions, the fundamentals such as continuity should hold here, and discontinuities should not appear in the middle of the entire thruster. Heavy particles might be simulated as a fluid while electrons are simulated as kinetic[72]. The opposite can also be done. A division between energy levels of the same species is also possible. These divisions are made based on regime considerations, geometric considerations or computational considerations.

The third, coupled multi-regime approach is where the separate models used are separated by location in space or time into domains, the considerations for which are the same as for the hybrid approach. While a hybrid model can present a great balance between accuracy and computational cost, the coupling schemes, especially when employing a kinetic PIC method, can be quite complex. The coupled multi-regime approach is in essence a higher fidelity version of employing a fluid and kinetic model with more considerations to preserving continuity and preventing any discontinuities. It can present a simpler modular scheme, as different fluid or kinetic models can be swapped out inside of the same coupling framework. This can present benefits for future iterations and improvements to specific models, both in terms of fidelity and numerical performance.

6.5. Relative comparison

It must be noted that the accuracy and computational cost associated with any model depends heavily on the case on which they are applied. Should a case consist of a plasma that is entirely in the fluid domain, the accuracy of the modeling predictions will be high and with a low cost, while the kinetic model predictions will not be significantly more accurate but achieving these results will be associated with a very high, or even unreasonably high, computational cost. On the other hand, should the case be fully kinetic, the fluid model will not be accurate enough. This means that any comparison between these models is heavily dependent on the case on which they are applied. To allow a rough comparison, the performance for some models which were considered in the literature study preceding this thesis will only be given depending on its intended area of application. This is done because, unless stated otherwise, their use outside of said area is either unpractical due to large computational costs (kinetic models) or due to inaccurate modeling of involved physics and thus poor results (fluid models). The expected performance of these models is showcased in table 6.1. Finally, it is important to realize that due to the large number of interlinked parameters, decisive models with levels of predictive accuracy approaching those found in models for chemical propulsion have yet to be achieved. Furthermore, due to the challenges in taking accurate measurements, validation data for these models often has large uncertainties, and errors between predictions and measurements are often in the order of a few percent, for all types of models.

6.6. Coupled multi-regime model limitations: 3DVIRTUS-Starfish

To more accurately approach the modeling of a system in which plasma transitions between different regimes, the limitations of the assumptions made in coupled multi-regime models and their respective separate models have to be reviewed. That way, an assessment can be made as to which assumptions may be held in place and for which assumptions more faithful solutions should be considered when coupling the separate models to form the coupled multi-regime model.

The following review and analysis of assumptions and solution methods in a coupled multi-regime model will use as a baseline the numerical suite by Magarotto *et al*.(2021), referred to as the 3DVIRTUS-Starfish model. This numerical suite consists of a fluid module which is applied in the source chamber and a kinetic module which is applied in the plume region. The fluid module consists of the 3D-VIRTUS[2] fluid model which is run in the OpenFOAM software. OpenFOAM is an open-source C++ software in which numerical solvers for 3D computational fluid dynamics problems can be developed, executed and pre-/post-processed[78]. Inputs and outputs are field data files for specific instances in time. These files contain the field values for any predefined variables or local flow properties such as the pressure, density or velocity fields. Meanwhile the kinetic module consists of a PIC model which is run in the Starfish software. Starfish is a Java simulation software for 2D plasma and rarefied gas problems which utilizes kinetic or fluid solvers[73]. Like OpenFOAM, it is open-source[79] and provides output as value fields for any predefined variables or local flow properties at a specific instance of time. Unlike OpenFOAM, the required inputs are, in general, average values from which uniform starting fields are initialized.

The reason for choosing the 3DVIRTUS-Starfish coupled multi-regime model as the baseline for this thesis work is that it attempts to couple accurate numerical models for the fluid and kinetic regimes, considering the plasma as one coupled whole while still only applying the fluid and kinetic models on their respective regime domains. By considering all species in the magnetic nozzle to behave kinetically, it is believed to perform better than hybrid models when the boundaries of the plume are placed further away, where all species are very rarefied. Furthermore, due to the large availability in literature of separate models for each region, improving the coupling in this numerical suite, which currently maintains the standard region-division, provides a modular framework which may provide important insights and practices for generalized multi-regime model coupling for the APT modeling field beyond this specific set.

The main limitations of the assumptions used in this numerical suite are presented in the following subsections. The proposed improvements to these limitations, presented in chapter 2, form the starting point of those coupling methods considered in this thesis work, and are implemented physically and numerically in chapter 7.

6.6.1. Assigning physical domain to geometric domain

One of the strongest criteria considered for the transition from the fluid regime to the kinetic regime is the large potential drop or flow rarefaction observed between the regimes, as described in section 5.3. Currently, rather than identifying where this transition occurs, the numerical suite imposes this transition at the source chamber boundary, or the throat, of the thruster. By grounding this boundary's potential and setting the Mach number to $M = 1$, the geometric definition of the two thruster sections is imposed over the definition of the physical regimes; spatial location takes precedence over local plasma characteristics. It is however known that the potential drop can occur earlier or later downstream of the thruster[41], [80] and that the Mach number encountered at the throat can be different from unity, observed both in models and experiments[39], [40], [81]. Neither assuming sonic flow velocities at the throat in both models[9], nor sonic flow velocities in a chamber model with slightly supersonic conditions in a subsequent nozzle model[52] gives clean results, showing the need for improvement in the coupling methodology.

6.6.2. Violation of continuity in the fluid module

Investigation in the total mass flow throughout the thruster as modeled by the numerical suit shows a violation of continuity across the coupled models, caused by the fact that the source model does not consider the back flow of plasma species entering the source chamber from the plume again. This is a severe shortcoming, especially as the fluid module depends heavily on the continuity equation. Fur-

thermore, the back-flow of electrons to the thruster source boundary is not simply a numerical necessity for maintaining the current balance in the kinetic model, but it is a real physical phenomenon where electrons with too little kinetic energy to escape the plume potential will become trapped. Hence the fluid module should be adapted to be able to take this back flow phenomenon into account.

6.6.3. Oversimplification of plasma profiles at outlet

In the regular setup, the kinetic part of the coupled model only takes a single average number density, temperature and velocity for each species as input for the injection algorithm. Meanwhile however, the fluid model provides a full 2D profile for each of these values for each species, except for the temperature of the heavy species. Thus, the variation of these variables across the entire border between the two models, the domain interface, is now neglected, causing a loss of information: the actual distribution is lost, decreasing the fidelity of the simulation.

6.6.4. RF power deposition beyond the source chamber

It has been shown that while the RF power deposited into the plasma is mainly restricted to within the source chamber, the power deposited into the plume is non-negligible[42]. The kinetic model, however, does not consider any power coupling from antennas. The EM-code Adamant[76] which is responsible for power coupling in the fluid code could be separately applied to the kinetic code. Another simpler approach to increase the amount of RF power accounted for is to extend the fluid model as far outside of the source chamber as the fluid regime allows, thus increasing the region in which RF power is accounted for. In any case, the fields only continue until an Electron Cyclotron Resonance surface is reached. This surface always exists downstream of the thruster, and thus the fields do not continue until infinity[42]. Which solution and domain to include as feasible and computationally warranted, is open to investigation.

7

Multi-Regime Solver

In the previous chapter, mention was made in section 6.6 of a numerical suite which modeled the thruster as a whole, applying a fluid model in the OpenFOAM code to the source chamber and a kinetic model in the Starfish code to magnetic nozzle. Building upon this early work by the universities of Bologna and Padova, this chapter addresses the first sub-question of the research question: ”What coupling methods will or can be tested?” It covers the development strategy as well as the physical and numerical coupling methodologies that have been considered during this thesis work. The development and methodologies are presented in the framework of MUPETS, the MUlti-Regime Plasma Equilibrium Transport Solver that has been developed as the final result of this thesis. When relevant, alternative methodologies that have also been tested will be discussed in preparation for the verification, validation and comparison of these methods in chapter 8. The development of the solver is described in section 7.1 and details the intended improvements to be included. The physical methodology is then covered in section 7.2, describing the theoretical methods to carry out the chosen improvements. The numerical implementation of the theoretical methodology is explained in section 7.3, showcasing the interfacing of the MUPETS code with the OpenFOAM and Starfish codes.

7.1. Coupling methods

In order to introduce different coupling methods into the coupled model in an orderly method, maintaining good control of the implemented methods as well as of the scope of the work, the improvements are addressed in steps. The work process is conducted as follows: For each step, first the physical methodology is defined or updated. After this, the physical methodology is numerically implemented. Following this, the resulting coupled model from that step is verified. Finally when this is done, work proceeds to the next step, starting with updating the physical methodology. After all steps have been implemented and verified, or when new steps cannot be included anymore within the thesis time-frame due to problems encountered in the methodology or implementation, the final resulting coupled model is validated.

The level of impact of the coupling method on the model’s methodology will increase in each step, such that a complicated method is only applied after the easier methods have been successfully incorporated and verified. This shall isolate potential issues and thus reduce the risk of either running overtime, or ending up with an unfinished model. Furthermore, lessons learned or insights gained from the implementation or verification of earlier steps can be used in defining or streamlining the physical methodology, numerical implementation or verification of later steps.

The steps shall each address one of the limitations presented in section 6.6 through implementing an improvement. The intended improvements have already been covered at the start of this report in section 2.1. The total sum of the methods used to achieve these improvements shall form the coupling methodology. Certain improvements can be achieved through different methods themselves, thus leading to a few different final coupling methods to test for verification and validation.

The problem of RF power deposition beyond the source chamber, described in section 6.6.4, shall not be included in the step approach. This thesis focuses on the coupling of the plasma fluidic model to

the plasma kinetic model, and the coupling of the RF-wave propagation and power deposition into any coupled plasma flow model requires interfacing or coupling with an EM-model which lies outside of the thesis scope. It has also been shown that while not negligible, the power deposited outside of the source chamber remains a mere fraction[42] of the total deposited power. Furthermore, any extension of the fluidic domain outside the source chamber, relevant to the mapping of the numerical domains as covered in section 7.1.3, will increase the amount of RF-power deposited outside of the source chamber taken into consideration[42], [46].

Thus, the coupled model shall be built up in three (3) steps, in increasing order of complexity. The steps and the intended improvements are the following:

Step 0: Achieve higher fidelity coupling of plasma properties across the domain interface.

Step 1: Preserve continuity and self-consistent coupling in both directions through an iterative looped model.

Step 2: Obtain higher fidelity and optimized fluidic domain utilization by defining numerical domains based on automated regime mapping.

The steps will be further explained in the following subsections.

7.1.1. Step 0: Higher fidelity coupling plasma properties across domain interface

The Starfish solver is initialized each time it is run by a uniform plasma profile at the transition boundary, with all species having a Maxwellian VDF. However, to reach an accurate coupling of the fluid and kinetic model, the assumption of a uniform plasma profile over the entire boundary must be removed. It is known that the profile will vary radially[46], hence this variation should be respected. OpenFOAM already does so and provides a plasma profile that can vary spatially over the boundary surface. Instead of averaging over the surface and taking those averaged properties to be uniform over the entire initialization at the transition boundary of Starfish, the local properties should be mapped between model meshes. For this, a numerical mapping strategy is required to match the meshes such that the following equation can be employed:

$$n^n_{k,kin}(\mathbf{x},t) = n^n_{k,fld}(\mathbf{x},t) \tag{7.1}$$

This shall require the use of mesh interpolation and altering the Starfish code such that it can accept spatially varying inputs, removing the assumption of uniform profiles at its injection source.

7.1.2. Step 1: Iterative loop

To address the issue of electron back-flow, the OpenFOAM and Starfish codes should be solved iteratively, with OpenFOAM updating its BCs at the thruster outlet boundary or other transition boundary to reflect the kinetic state there. As the PDF inside the fluidic solver maintains a Maxwellian distribution regardless of any additional back-flowing particles with negative velocities, it is not possible to update the PDF in the fluid domain to that of the kinetic domain. Instead, the following BC at the transition boundary can be set:

$$n^{n+1}_{k,fld}(\mathbf{x},t) = \int f^{n+1}_{k,fld}(\mathbf{x},\mathbf{v},t)d\mathbf{v} = n^n_{k,kin}(\mathbf{x},t) \tag{7.2}$$

Where $n^{n+1}_{k,fld}(\mathbf{x},t)$ and $n^n_{k,kin}(\mathbf{x},t)$ are the number density of species k at the transition boundary in the fluidic model in the next iteration and the number density at the transition boundary in the kinetic model in the current iteration respectively. It is important to note that just setting the densities is not the goal; the goal is to correct the fluidic PDF in a manner that upholds its Maxwellian distribution, but at the same time corrects it such that the correct density, that of the kinetic model which acknowledges back-flow, is present at the boundary. This is important because other macroscopic values that we wish to correct such as the temperature or energy are also depending on the PDF itself, therefore correcting the PDF is still the main method of including the back-flow. The condition for updating the number density of the fluidic model to that of the previous iteration of the kinetic model, achieved by a correction of the PDF, can be achieved through the following iteration scheme:

$$a(\mathbf{x},t) = \frac{n^n_{k,kin}(\mathbf{x},t)}{n^n_{k,fld}(\mathbf{x},t)} \tag{7.3}$$

$$f_{k,fld}^{n+1}(\mathbf{x},\mathbf{v},t) = a(\mathbf{x},t) f_{k,fld}^{n}(\mathbf{x},\mathbf{v},t) \tag{7.4}$$

Now equation (7.2) can be written as:

$$n_{k,fld}^{n+1}(\mathbf{x},t) = \int a(\mathbf{x},t) f_{k,fld}^{n}(\mathbf{x},\mathbf{v},t) d\mathbf{v} = a(\mathbf{x},t) \int f_{k,fld}^{n}(\mathbf{x},\mathbf{v},t) d\mathbf{v} = a(\mathbf{x},t) n_{k,fld}^{n}(\mathbf{x},t) = n_{k,kin}^{n}(\mathbf{x},t) \tag{7.5}$$

An alternative approach is to not correct the densities directly, but one of the other fundamental variables in the fluid model, most notably the plasma potential. Changing the plasma potential gradient will change the resulting charged particles distribution and vice versa. The choice of which approach to take depends on the balance between what is physically more accurate and what is numerically possible or efficient.

7.1.3. Step 2: Regime mapping

Two possible methods for accurately mapping the regimes have been considered: The first method entails finding the transition surface by searching for specific behavior of the transition-parameters described in section 5.3. The second method consists of creating an artificial buffer region around or near the throat in which both regimes are solved for, following the method described by Dimarco, Mieussens and Rispoli(2014)[82].

Transition parameter search method

By pre-modeling the entire thruster in the fluidic model first, the transition surface can be mapped by searching in the solution for the occurrence of a plasma potential drop and/or the Knudsen value approaching unity. After this, the solver can be set up to run the fluidic model up to this transition and to run the PIC module at and downstream of this transition. This minimizes computational cost by maximizing the area in which the fluidic model is truthfully applied at its corresponding regime, while ensuring the PIC model is applied where the kinetic regime occurs and necessitates it. After the initial iteration has been completed, the total solution of the plasma flow can be investigated again for an updated location of the transition, after which the domains are updated again and the new iteration starts.

The challenges in this method are two-fold. The first challenge is to define the correct transition criteria: a specific value of ϕ, denoting large enough potential drop, and the threshold value where K_n is said to approach unity. Another method to define the correct transition criteria is to identify indicator functions that look at transition effects instead of causes. For example, indicator functions have been defined by the ratio between kinetic and fluidic models' sum of terms, as the number of corrective terms differ per model, in the momentum or energy equation[82]. The second challenge is to set the correct BCs, especially for the pre-modeling fluidic mapping simulation, such that the location of the transition surface can be predicted with an adequate degree of accuracy. After this, care must be taken that the used BC's are consistent with the regimes in which they take place, that the solution does not contradict the findings of the initial mapping-simulation.

Transition buffer region method

This method is based on the ideas presented by Dimarco, Mieussens and Rispoli(2014). This method sets a buffer region in which a transition from the fluid to kinetic solution gradually takes place. This buffer zone removing the need of interface conditions[82]. However, as the coupling scheme of Dimarco, Mieussens and Rispoli(2014) works on one total set of governing equations that is applied throughout the entire domain with only a cut-off function determining any difference between kinetic, fluidic or both models. Thus, there is only one set of equations that is solved over one common time step and made numeric in one code. For the OpenFOAM-Starfish suite however, there are two distinct codes, which cannot be easily coupled to be run at exactly the same time step and summate to a total PDF before moving to the next spatial node.

Hence, the models would need to be run iteratively, each time initializing themselves with an updated plasma profile in the buffer zone that is the result of a newly combined PDF.

7.2. Physical coupling methodology

With the division of improvements into steps, the critical question is how these couplings can be carried out from a physical point of view, not violating the laws of physics whilst requiring as few assumptions

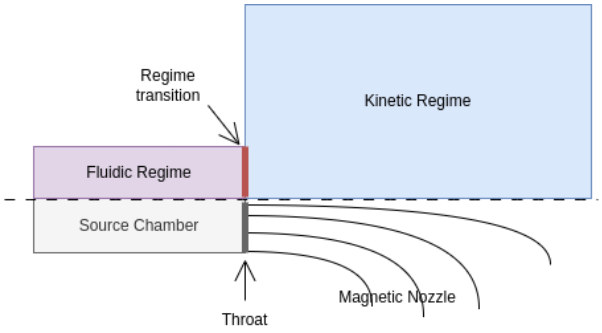

Figure 7.1: Model of HPT geometry showing the location of the source chamber, magnetic nozzle and the assumed locations of fluid and kinetic regimes

as possible. To ensure the physical soundness of the coupling, a logical approach is to base the coupling methodology on the models own physical methodology. The separate models' own physical methodologies are therefore presented before the physical coupling methodology itself is covered.

7.2.1. Separate Models

The MUlti-regime Plasma Equilibrium Transport Solver (*MUPETS*) consists of a fluid model run in OpenFOAM, based on the 3D-VIRTUS code[2], coupled together with a kinetic PIC model based on the Starfish code[32], [73]. figure 7.1 shows the modeled thruster geometry, including the regime region definition. The model is a 2D axisymmetric representation of an APT. The entire source chamber is considered to be in the fluid regime, denoted in purple. In the simplest coupling scheme the fluid domain fills the entire source chamber, extending radially from the center-line of the thruster to the source chamber walls and axially from the back-wall to the outlet. The expansion plume of the plasma flow into the free space surrounding the plasma is considered to be in the kinetic regime, denoted in blue. In the simplest coupling a portion of this infinite free space, starting from the outlet, is modeled in the kinetic domain. How these numerical domains are placed and coupled to each other will be explained further in section 7.3.4. The modeled thruster is assumed to operate under steady state conditions for both the fluid and the kinetic model.

Fluid model

The fluid model used inside the source chamber has been developed by the universities of Padova and Bologna [2], [9], [83]. It considers as separate species the neutral atoms, excited atoms in the lumped 1Sr, 1Sm and 2P states[49], single positive ions and negative electrons, all denoted with the subscripts 0,$1Sr$,$1Sm$,$2P$,i and e respectively. When the excited state species are grouped together, the subscript ex is used instead. The governing equations for the plasma dynamics in the fluid model are the conservation of mass equation (7.6) for each species number density n_I where subscript I denotes the species and the conservation of energy equation (7.7) for the electron energy density n_ε. Poisson's equation (7.8) completes this set for solving the plasma potential ϕ and obtaining the internal electric field.

$$\frac{\mathrm{d}n_I}{\mathrm{d}t} + \nabla \cdot \Gamma_I = R^I_{chem} \tag{7.6}$$

$$\frac{\mathrm{d}n_\varepsilon}{\mathrm{d}t} + \nabla \cdot \Gamma_\varepsilon - \nabla\phi \cdot \Gamma_e = Pw - P_{chem} \tag{7.7}$$

$$\nabla^2\phi = -q\left(\frac{n_i - n_e}{\varepsilon_0}\right) \tag{7.8}$$

q is the electric charge and ε_0 is the free-space permittivity, while R^I_{chem}, Pw and P_{chem} are respectively the source/sink term for the species plasma reactions, the power coupled to the plasma and the power lost or gained through plasma reactions. Finally, Γ_I itself denotes the flux of the species and the electron density, and is modeled through the Drift Diffusion (DD) approximation shown in equation (7.9).

$$\Gamma_I = -D_I \nabla n \cdot \hat{n} \pm \mu_I E \cdot \hat{n} n \tag{7.9}$$

Here, D_I and μ_I are the diffusion and mobility coefficients of the species respectively while E is the electric field. These coefficients and the R^I_{chem}, Pw and P_{chem} terms are expanded upon in[9]. The sign in $\pm$ is chosen accordingly to the charge of the species.

The uncoupled fluid model is completed by a set of BCs for the source inlet and walls[35], while the treatment of the outlet is covered in section 7.2.2 as it functions as the interface between the fluid and kinetic model. Both the inlet and walls are assumed to be grounded and thus have zero potential [83] as shown in equation (7.10)

$$\phi_{inlet,wall} = 0 \tag{7.10}$$

For the species, three different BCs are imposed upon their fluxes Γ_I at the wall and inlet. The light electron transport at the wall is modeled through the Bohm sheath criterion[49], [83], imposing the Bohm velocity[44], $v_B = \sqrt{\frac{qTe}{M_i}}$ as shown in equation (7.11).

$$\Gamma_{e_{inlet,wall}} = v_B n_e \tag{7.11}$$

Here, the electron temperature T_e is used in conjunction with the ion mass M_i. The electron energy density is linked to the electron density and temperature as $n_\varepsilon = \frac{3}{2} n_e T_e$. its fluxes at the boundaries are set according to the Bohm sheath criterion[49], [84] as shown in equation (7.12)

$$\Gamma_{\varepsilon_{inlet,wall}} = \frac{2}{3}\left(\frac{1}{2}\left(1 + \ln\left(\frac{M_i}{2\pi M_e}\right)\right) + 2\right) \cdot \sqrt{\frac{qTe}{M_i}} n_\varepsilon \tag{7.12}$$

The heavy ions and excited neutrals are modeled through the Hagelaar conditions[85]. For the single positively charged ions considered in the model, this results in the BC[83] given by equation (7.13).

$$\Gamma_{i_{inlet,wall}} = \mu_i E + \frac{1}{2} n_i v_{th_i} \tag{7.13}$$

For the excited but charge-less neutrals, $1Sr, 1Sm, 2P = ex$, this equation simplifies[83] to equation (7.14).

$$\Gamma_{ex_{inlet,wall}} = \frac{1}{2} n_{ex} v_{th_{ex}} \tag{7.14}$$

Finally, at the wall and inlet, neutrals in the ground state are assumed to be gained through recombination of ions and electrons impinging on the wall, as well as excited neutrals falling back to their ground state[83]. Thus, the flux of ground state neutrals at the wall equals the negative sum of the impinging fluxes of ions and excited neutrals as shown in equation (7.15), while at the source inlet an additional term is included to reflect the incoming flux resulting from the injected mass-flow of neutral gas[83], shown in equation (7.16).

$$\Gamma_{0_{wall}} = -\Sigma_{k=i,ex} \Gamma_k \tag{7.15}$$

$$\Gamma_{0_{inlet}} = -\Sigma_{k=i,ex} \Gamma_k - \frac{\dot{m}}{A_{inlet} M_0} \tag{7.16}$$

Here, $\dot{m}$ denotes the injected massflow of neutral gas into the modeled thruster, A_{inlet} the surface area of the inlet boundary and M_0 the mass of the neutral particles.

Kinetic Model

The kinetic model has been developed by the universities of Bologna and Padova[32]. The macro-particle motion is solved through equation (7.17) while the Poisson's equation equation (7.8) again solves the plasma potential ϕ.

$$\frac{\mathrm{d}\vec{v_p}}{\mathrm{d}t} = \frac{q_p}{m_p}\left(\vec{E} + \vec{v_p} \times \vec{B}\right) \tag{7.17}$$

The set BCs at the free-space limits of the modeled domain are as follows: The potential is assumed to behave as $\phi \approx 1/r$ for $r \to \infty$ and thus the gradient across the external boundary is modeled as equation (7.18) where k is the direction normal to the external boundary, r is the total distance between the centre of the thruster and the boundary and ϕ_∞ the potential at an infinite distance from the thruster outlet[4].

$$\frac{\mathrm{d}\phi}{\mathrm{d}k} = \frac{1}{r}\left(\phi_\infty - \phi\right) \tag{7.18}$$

Ions are removed from the simulation domain when they reach any of the boundaries[4]. For electrons however, this only holds for the casing and thruster outlet. At the external boundary, a special energy-based criterion is used to model electrons that become trapped or are free to leave the modeled domain, to maintaining a current-free plume[4]. This is governed by a value of ϕ_∞ that reflects sufficient electrons with a too low energy for escaping the exhaust plume, trapping them. The total energy of electrons reaching the external boundary is first calculated as:

$$E_{tot} = \frac{1}{2} m_e v^2 - q_e \phi \tag{7.19}$$

Then, if $|E_{tot}| > |q\phi_\infty$ the electrons will escape and be removed. If not, they are trapped and their velocity will be mirrored ($\mathbf{v} = -\mathbf{v}$). ϕ_∞ is self-consistently updated to enforce the global current-free plasma condition[86] shown in equation (7.20).

$$J_{i-} + J_e = -\sum_{i+} J_{i+} \tag{7.20}$$

Here, J_{i-} and J_e denote the current across the external free space boundary due to negative ions and electrons respectively, while J_{i+} denotes the current due to any ions with single, double or higher positive charge.

7.2.2. Coupling

The physical coupling scheme of the fluid and kinetic models is shown in figure 7.2. It also denotes what each step adds to the scheme. A complete coupled model, with all steps included, would consist of the following:
To start, the distribution of the model domains onto the full thruster geometry, including the free space around it, is defined, together with the appropriate BCs for all the separate domain boundaries, including those at the interface between the domains. Both the BCs and the domains are coupled at the interface. The methods of BC coupling are described in this subsection and the methods of domain coupling are described in section 7.3.4. After the case to be modeled is set up in this way, the fluid case will be run first. It runs its own n sub-iterations according to the SIMPLE method until convergence. After convergence, the resulting, spatially varying, species number density, velocity and temperature at the interface are taken and transferred across the interface as input for the kinetic model. After the kinetic model has run its own m sub-iterations, its output at the interface too is obtained and interpolated onto the fluid model's mesh to correct the appropriate BCs. Now, after this initial parent-iteration $h = 0$ of the coupled model, a new parent-iteration $h+1$ is started in which the fluid code is run first again, using corrected BCs. Before a new parent-iteration $h+1$ is started, the Knudsen value is calculated as a field value over the entire domain, and it is used to map the fluid and kinetic regime. These mappings then determine the numerical domains on which each sub model will be run in the subsequent iteration, as well as the location of the domain interface between them.

Separating this process back into the step-wise approach, each step can be summarized as follows:
Step 0 concerns only the first parent-loop $h = 0$ and does not include any interpolation of the kinetic solution onto the fluid domain yet. It ensures that the spatially varying plasma properties at the domain interface are used to construct the PDF and VDF of the kinetic model with the same spatial variation across the domain interface.
Step 1 includes the interpolation of the kinetic solution onto the fluid domain to correct the initially assumed BCs at the domain interface, and includes the iterative loop to subsequent parent-iterations $h \geq 1$, though without any regime mapping and domain changing.
Step 2 adds to the iterative loop the mapping of the regimes and the subsequent redrawing of the numerical domains before each new iteration.

Step 0

When coupling the models, special care must be taken that the coupling of BCs at the domain interface is sound from a physical standpoint, and effective from a numerical standpoint.
For all species in the fluid model, except the electrons, the BC at the domain interface given by equation (7.21) with k being the normal to the boundary:

$$\frac{\mathrm{d}n_{i,0,ex}}{\mathrm{d}k}_{interface} = 0 \tag{7.21}$$

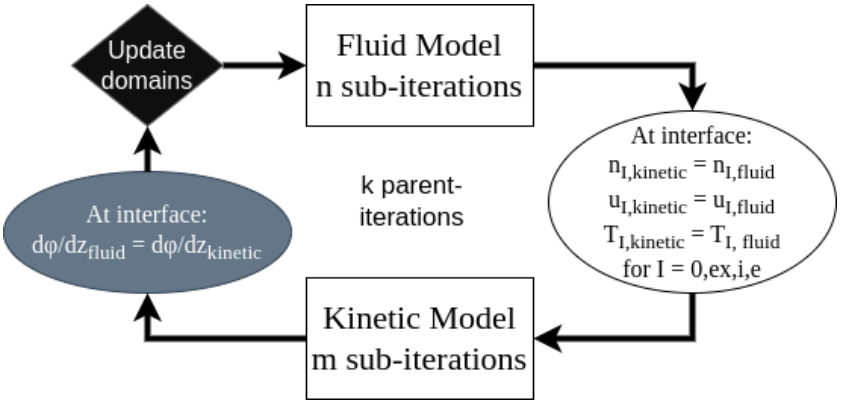

Figure 7.2: Solver physical methodology scheme. Actions are colored for each step. Step 0 has a white background, Step 1 has a gray background and Step 2 has a black background

The ions and neutrals are thus assumed to have reached developed flow state at the outlet.
During Step 0's single simulation, $h = 0$, the electrons are modeled in the fluid model through the Bohm sheath criterion as shown in equation (7.22), as is also done for the inlet and walls.

$$\Gamma_{e_{interface,h=0}} = v_B n_e \tag{7.22}$$

The electron energy density follows the electron density flux in the same manner as with the other boundaries, and equation (7.12) holds for the interface as well. As to the condition imposed to solve the Poisson's equation, it stems from the necessity to enforce, in a HPT, the current-free assumption at the interface[83].

$$\Gamma_{e_{interface}} = \Gamma_{i_{interface}} \tag{7.23}$$

This condition is then rewritten for the initial plasma potential BC in equation (7.24)

$$\frac{\mathrm{d}\phi}{\mathrm{d}k}_{interface} = \frac{\Gamma_i + D_e \frac{\mathrm{d}n_e}{\mathrm{d}k}}{n_e \mu_e} \tag{7.24}$$

Here Γ_e has been rewritten as its DD formulation in which the electric field E is substituted with $-\nabla\phi$. For the coupling of the kinetic model's BCs, a more straightforward flow of information is required to be transferred across the interface. As the kinetic model directly simulates the species as their own macro-particles, it requires the number density and the drift velocity, as well as the temperature of the species to construct both the PDF and velocity distribution function (VDF). These are then used to inject macro-particles at the interface into the numerical kinetic domain. The PDF is constructed assuming the average values of n_e and T_e provided by the fluid code[32].

At the interface, the kinetic model balances the injected electron flux from the fluid model against the charge balance of the fluxes going out of the external free-space boundary, in order to adhere to equation (7.20)[4].

Step 1

Step 1 introduces self-correcting iterations, $h \geq 1$. After the kinetic model has solved the plasma potential in h, the BCs on the fluid model's side can be corrected for subsequent iteration $h + 1$. First, equation (7.23) is used directly as the BC of the electron species at the interface, removing local assumption of the Bohm condition and letting the particles outflow to evolve self-consistently. Second, the potential gradient obtained from the kinetic domain is imposed to solve the Poisson's equation in the fluid model. Thus in all iterations after the initial solution, the BC in equation (7.25) is used.

$$\frac{\mathrm{d}\phi}{\mathrm{d}k}_{interface_{fluid_{k+1}}} = \frac{\mathrm{d}\phi}{\mathrm{d}k}_{interface_{kinetic_k}} \tag{7.25}$$

Thus, the coupling of the fluid model's interface BCs to the kinetic model only requires the plasma potential gradient from the kinetic model across the interface, as well as the assumption of net-neutral

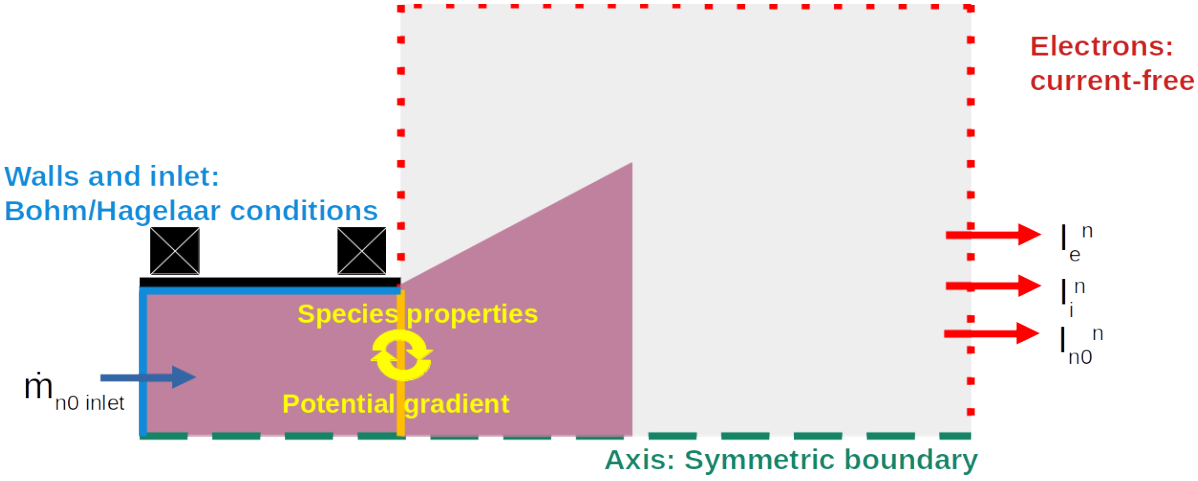

Figure 7.3: Relevant boundary conditions applied upon the axi-symmetrical thruster domain following Step 0 and Step 1

flux across the interface, which follows from the assumption of steady state. These change only the BCs imposed upon ϕ and n_e. All other species are assumed to be fully developed through a zero-gradient condition imposed upon their density gradients, as their drift/convection velocity-term, is usually much larger than their diffusion velocity-term[2]. Notably, the proposed set of BCs does not constrain the particle's speed at the interface to a pre-determined value (e.g., Bhom speed[2]), instead this value is computed self-consistently. Specifically, the ions flux is driven by the assumed electric field at the interface[2] which, in turn, determines the electrons' response, because of the current-free assumption. The physical model resulting from the implementation of Step 0 and Step 1 is shown in figure 7.3, showcasing the applied boundary on the full thruster domain.

Step 2

As stated in section 7.1.3, the higher fidelity and more efficient distribution of the numerical domains can either be conducted through a transition-parameter driven regime mapping, or through the use of a set buffer region in which a transition from fluid to kinetic solution gradually takes place. To start from a simple, and more modular framework that allows the swapping out of different fluid and kinetic models, the choice was made for the first method to be investigated first. Furthermore, as described in section 7.1.3, the transition-parameters can be the Knudsen value K_n, the plasma potential ϕ or an indicator function that looks at the transition effects instead of causes. As ϕ is already a tracked plasma property, and K_n can be easily obtained through post-processing, the use of any indicator functions is left for future work should the ϕ or K_n approaches not yield consistent or numerically stable results.

As dictated by the step-wise approach, before the physical methodology and numerical implementation of Step 2 would be conducted, the methodology and implementation of Step 1 should first be finished and verified. During this verification of the results obtained through Step 1, covered in chapter 8, which yielded the axial ϕ profiles shown in figures 8.4b and 8.12b, it was observed that the potential drop is spread out over a significant spatial distance, and not occurring at a distinct location spread over just the Debye length as early HPT theory suggested[80]. This has important implications for the methodology of Step 2; it will be difficult to find a single, distinct and thin border across which the ϕ drop takes place, which can then be used for the regime transition border. Therefore, having identified this problem during Step 1's verification, it is decided for Step 2's methodology that instead of ϕ, the Knudsen number will be used with a specific value set as the limit for the fluid regime. Specifically, to denote the breakdown of the fluid regime, the Gradient Length Local Knudsen Number will be used, which has already been successfully used in other experiments[87]:

$$Kn_{GLL-Q} = \frac{\lambda}{Q}\left|\frac{dQ}{dx}\right| > 0.05 \tag{7.26}$$

Here, Q is one of the following plasma flow properties: density, temperature, or velocity. As stated in section 5.2, the breakdown of the fluid assumptions generally already takes place before the $K_n = 1$ limit. Therefore, the maximum of Kn_{GLL-Q} values is checked against a limit value of 0.05. This

value was experimentally found to accurately predict the breakdown of continuum for rarefied flows[87]. Should the local value be above this limit, that location shall be in the kinetic regime, else-wise it shall be in the fluid regime. If K_n is then tracked as a field value across the entire thruster domain, the regime map can be made.
During the course of the thesis work, it became clear that while a valid physical methodology existed for Step 2, the numerical implementation and subsequent verification and validation would not be possible within the remaining time-frame of the thesis, especially considering the fact that multiple iterations per verification and validation case would need to be investigated carefully to pass verdict on the actual performance of the regime mapping, requiring long run times. Therefore, mapping the regimes through different parameters, re-defining of numerical domains, or eventually comparing the parameter-search method against a transitional buffer-zone method are left for future work.

7.3. Numerical Coupling Methodology

Having discussed the physical coupling methods implemented in each step to create the coupled model, the final step required to be able to use this model is to numerically implement it. Both the fluid and kinetic models, and therefore also the coupled model, presented in section 7.2 are complex and multidimensional. They require solving many linked differential equations and keeping track of many different particles. Hence, they are solved through numerical codes. The fluid and kinetic models are solved through their own distinct codes, while the coupling between these two is carried out through the over-arching MUPETS code[88] written for this thesis in Python. Key aspects of the separate codes will be presented, together with and overview of the MUPETS code and mention of any specific approaches that warranted consideration in numerically implementing the physical coupling methods, including the handling of the iterative loop and the numerical domains.

7.3.1. Separate Codes

The fluid model is solved through a custom-written solver in the open-source code OpenFOAM[78], while the kinetic model is solved through an adapted version of the open-source PIC code Starfish[73]. The benefit of having the coupling framework being handled by the MUPETS code instead of inside the solvers themselves, is that it allows for a modular coupled model in which the solvers themselves can be replaced by other models which may be updates, higher fidelity models or more numerically efficient. This can however either over-complicate the coupling, or reduce the physical or numerical performance. Hence, careful verification and validation of each resulting coupled model is still required, as well as proper consideration of the efficient utilization of the resulting model.

Fluid Code: OpenFOAM

As mentioned in section 7.2.1, the fluid physical model is based on the fluid module of the 3D-VIRTUS code[2] which is run in OpenFOAM.
To run a simulation case in OpenFOAM, three directory groupings of user-defined information are required:

1. 0-directory: starting and BCs.
2. constant directory: constant values.
3. system directory: simulation instructions, solver parameters and mesh definition.

The starting conditions depend on the propellant used and the simulated setup. The BCs follow the physical methodology and thus use Neuman, Dirichlet, and Robin BCs as specified in section 7.2. The constant values follow from physical constants, propellant properties and chemistry. Finally, the simulation instructions are defined in OpenFOAM dictionaries. These include the specific solver to use, time-step details, the numerical domain and mesh definition, the schemes used to linearize derivatives in equations or interpolations into one matrix equation, and what linear solver is to be used for solving the matrix equation.
When a simulation case is run in OpenFOAM, the solver to be used defines the set of equations and variables necessary to solve the problem, as defined by the physical, fluid model in section 7.2.1. The variables are obtained from the 0-case, in which every required variable, be it scalar or vector, has been defined for every cell volume of the mesh, including boundary surfaces. The equations of the solver are then linearized according to the numerical schemes defined in the system directory, and the collective

numerical schemes	
time derivatives	backward 2nd order, implicit
gradients	Face limited, 2nd order, Gaussian integration with linear interpolation
divergence	Gauss interpolation with MUSCL interpolation
interpolation	linear
surface normal gradient	Explicit non-orthogonal correction
distance to wall	meshWave calculation
matrix solver	
phi	GAMG
pressures	GAMG
transonic pressures	PBiCGStab
electron densities	PBICGStab
neutral densities	PCG
ion density	PBiCGStab
velocities	PBiCGStab
algorithm	SIMPLE, 3 correctors, 1 outer corrector

Table 7.1: OpenFOAM simulation system settings

set of linearized equations is placed in an equation matrix, thus linking all equations and variables of the case. This equation matrix is then solved through a numerical solver and algorithm, again defined in the systems directory. When convergence to a solution has been reached, the simulation marches forward in time according to the defined time-step, and iterates to a solution again, until the defined end-time has been reached or steady state has been achieved. The final solution is then saved at its corresponding time in the same format as the initial conditions, being all the cell-center and boundary face-center values of all fundamental physical variables, as well as all derived quantities. An example of the input and output format of OpenFOAM field values of the plasma potential variable can be found in appendix B. In table 7.1 the chosen time step, cell size, specific numerical schemes, matrix-solver and convergence algorithm used for this model can be found.

Kinetic Code: Starfish

The kinetic PIC model is handled by Starfish[73], adapted by the universities of Bologna and Padova[32]. As opposed to OpenFOAM, the required input format differs from the output format. Instead of defining an existing starting field, plasma particles are injected at a source surface into an empty domain, and these particles are tracked across iterations until a convergence has been reached. The amount of injected particles is determined by the density, temperature and drift velocity of the corresponding species. Once the simulation has converged, the solution is averaged over many additional iterations, to remove the noise that is commonly observed with PIC methods. The output then consists of the field values of the macroscopic properties of the plasma, which are found from interpolating the effect of the macro-particles at every mesh node. The model assumes the injection source surface, which coincides with the domain interface, to be arbitrarily set at 0 potential and thus follows equation (7.10) at the interface as well. The particle motion described in equation (7.17) is solved through the standard leap-frog Boris algorithm, while the collision processes are modeled through Direct Simulation Monte Carlo (DSMC) and Monte Carlo Collision (MCC) methods. 7 types of collisions are considered[4]:

1. electron-electron Coulomb scattering
2. electron-ion Coulomb scattering
3. electron-neutral elastic scattering
4. ionization
5. ion-neutral elastic scattering
6. ion-neutral charge exchange
7. neutral-neutral elastic scattering.

The expansion of neutral particles is handled separately from that of charged ions and electrons to decrease the run time. Interactions between charged and neutral particles are therefore calculated

through setting the solution of the neutral plume expansion as a background for the charged species to be modeled over. Surface reactions are handled through a surface interaction module and the interactions at this surface can either result in:

1. absorption: incident particles are deleted from the simulation
2. specular reflection: the angle of reflection is equal to the angle of incidence
3. diffusive reflection: incident particles are reflected with a random angle and velocity depending on an accommodation coefficient

In the plume model, surfaces are placed behind the injection surface to prevent species going around the injection surface and arriving behind it. These surfaces absorb the incident particles. In the numerical domain overlap method, part of the source walls are also modeled as a diffusive surface, where the reflected particle is changed into a recombined neutral. The surfaces can also be used to model a physical expansion cone when the neutral thrust is of interest, though this is not done in the current coupled model. The rest of the domain boundaries formulate the free space boundaries, made to resemble the free space at an infinite distance away from the thruster.

7.3.2. MUPETS Code

All the coupling methods are implemented numerically through the MUPETS Python code, and through slight adaptions in the OpenFOAM and Starfish codes to allow interfacing. The OpenFOAM and Starfish codes are responsible for:

1. Receiving a simulation case in their respective standard formats
2. Solving their respective numerical models through sub-iterations on their own solution, n and m respectively
3. Storing their converged solutions as fields values for each quantity.

The MUPETS code is then responsible for:

1. Pre-processing simulation cases for each model:
   (a) For $h = 0$, to set up the starting case with any imposed starting values
   (b) For $h > 0$, to set up or update a case with new BC values obtained from the other model's simulation case
2. Command the run of each case with the relevant solver and run parameters
3. Post-process the stored solutions of each simulation case to a common data structure after their respective solutions have converged
4. Using the obtained simulation case solutions, alter, derive, inter- or extra-polate these to find the conditions required to impose upon the next simulation. The method of how and what follows from the physical coupling methodology. The imposing then happens in the pre-processing step again.
5. Control the looping of the parent-iteration of the code per Step 1: after the solution of the kinetic model has been found, the code can loop back to pre-processing of the fluid model, where it will use the solution of the kinetic model to continue the loop. This loop must stop when a convergence criterion is met.
6. Control handling of numerical domain division and location of the domain interface. This is required for both a smooth carry-over of plasma properties between models in case of numerical noise near the domain interface, as well as for any methods utilized in Step 2.
7. Post-processing the final solutions through plotting and calculation of thruster performance.

Based on these tasks, the MUPETS code can be divided in 4 modules, run in a loop:

- Fluid module (pre-process, run and post-process OpenFOAM)
- FoamFish module (couple post-processed OpenFOAM results to setup of next Starfish case)
- Kinetic module (pre-process, run and post-process Starfish)

- FishFoam module (couple post-processed Starfish results to setup of next OpenFOAM case)

The functioning of the fluid and kinetic modules lies simply in updating any of the initial condition files for each respective code, giving the run command with any parameters such as the number of processors, and afterwards constructing a python dataframe or csv file with, for each and every cell and boundary surface, the spatial coordinates and all other variable values. The running of each separate code has already been covered in section 7.3.1 and the updating and dataframe construction concern only simple scripts which read or write data to different files. The FoamFish and FishFoam modules however employ the actual coupling described in section 7.2.2. Finally, to determine when the iterative loop must be terminated, a convergence criterion is checked for in the FishFoam module. This criterion is defined in section 7.3.3. The detailed numerical flow diagrams of the MUPETS code as a whole, the FoamFish and FishFoam modules, and the Postprocessing code which exists outside of the loop are shown in figures 7.4 to 7.7. The FoamFish and FishFoam modules are explained in the following subsections.

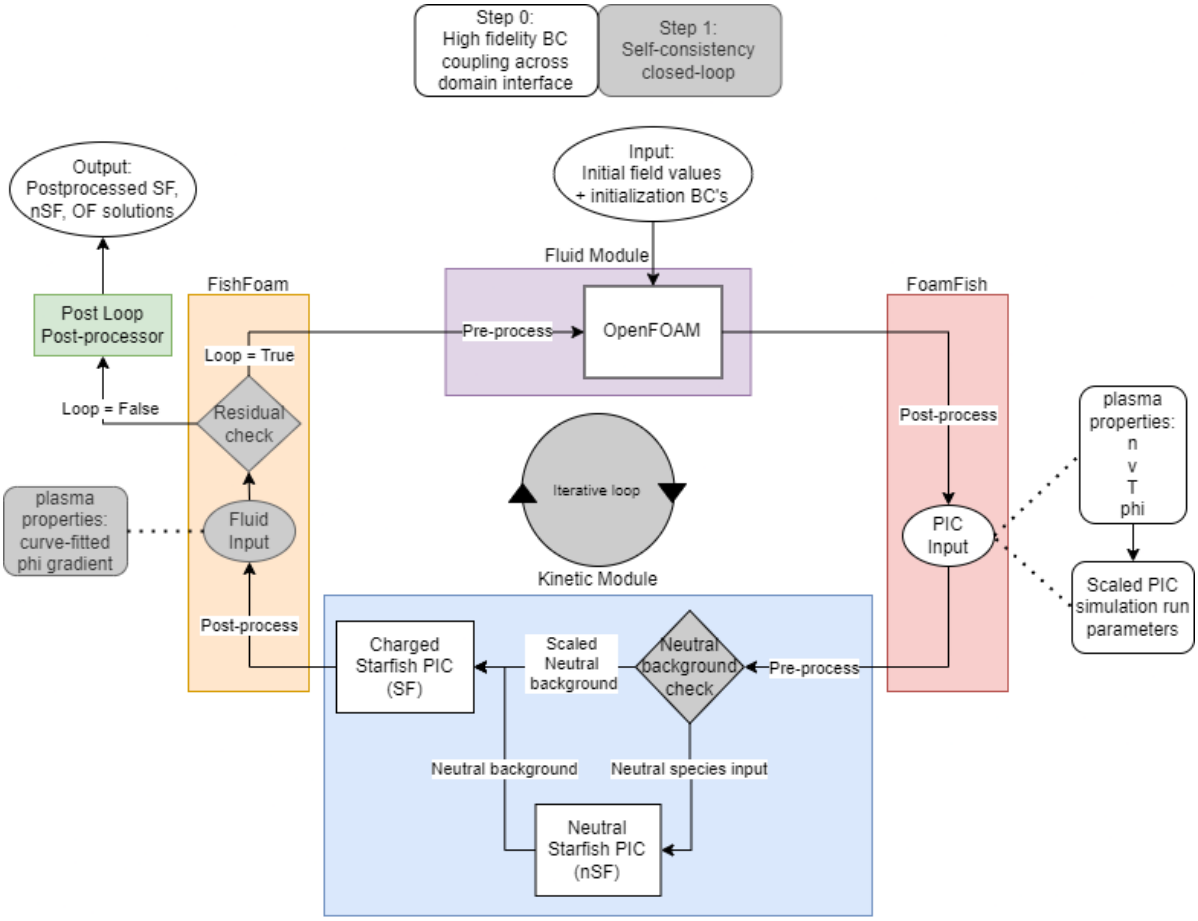

Figure 7.4: MUPETS code flow-diagram. Functions included in Step 0 are white, functions included in Step 1 are gray. The four modules and the Post Loop Post-processor are denoted by the following grouping colors: The Fluid module in purple, the FoamFish module in red, the Kinetic module in blue, the FishFoam module in orange and the Post Loop Post-processor in green.

FoamFish

After the Fluid module has reached convergence and found a steady state solution, all field values are obtained. From these, the values of the species number density n_I, species drift velocity normal to the domain interface (the domain interface, until mapped, is assumed to lie on the azimuthal-radial plane), u_I, and the species temperature T_I are of interest. Here, subscript I denotes the different species $I = 0, 1Sm, 1Sr, 2P, e, i$. These variables are used to determine the number of particles to be injected and their velocity according to the following methodology[4]: the density profile is passed as a sampling function to Starfish by performing an inverse transform sampling on the distribution provided by

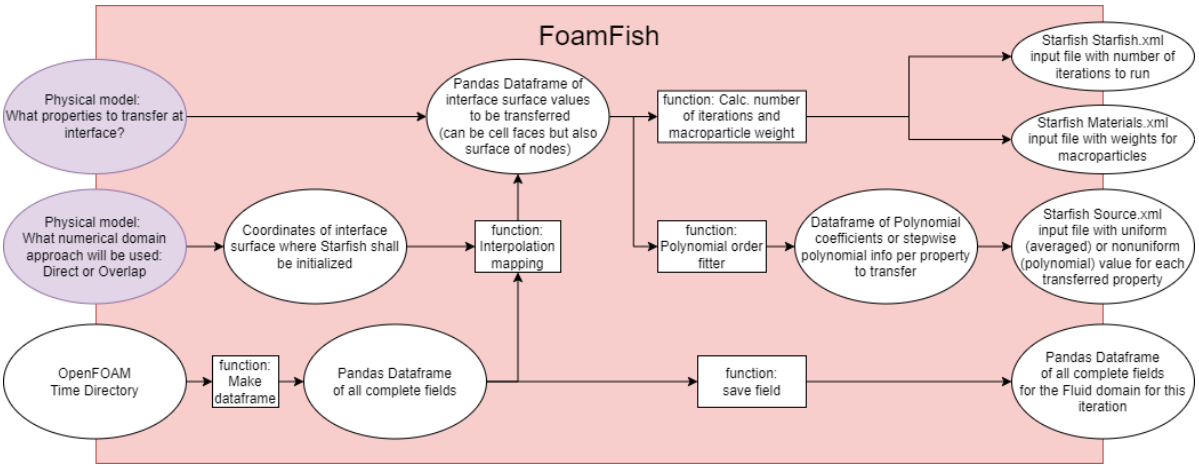

Figure 7.5: Detailed flow-diagram of the FoamFish module. Items in purple flow from the general physical model used. There is no difference between Step 0 and Step 1 implementation here.

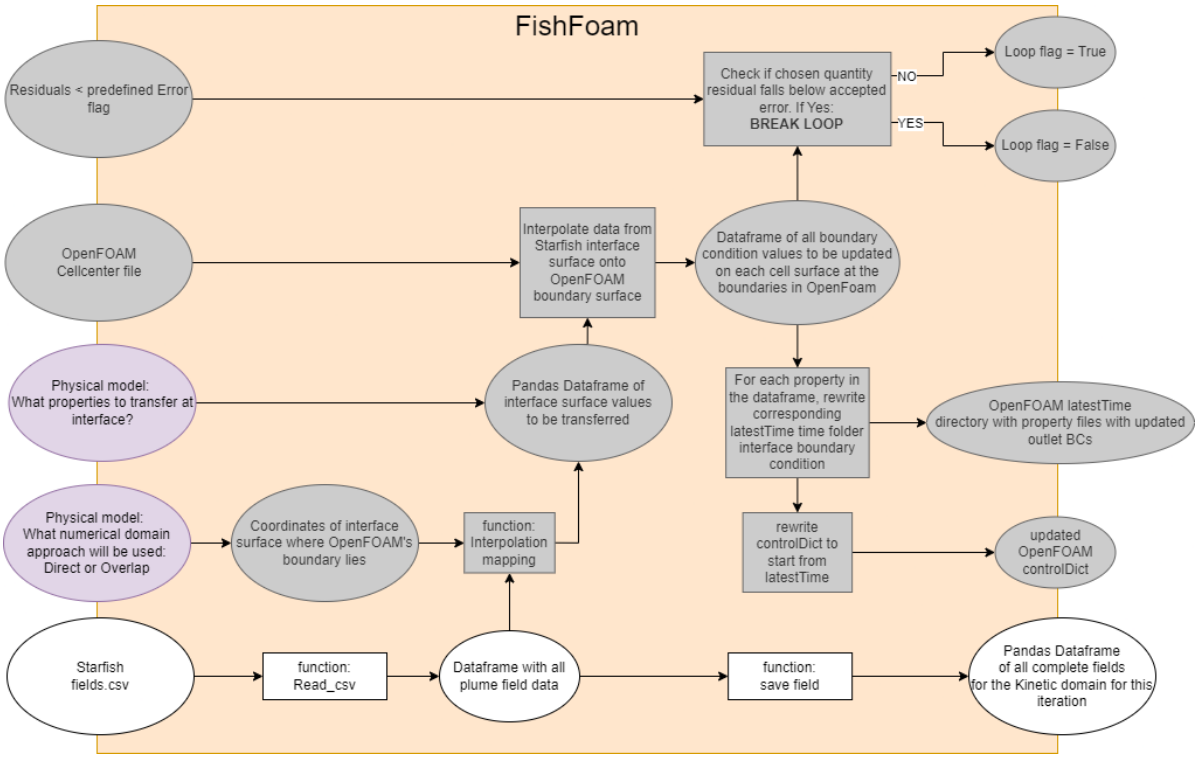

Figure 7.6: Detailed flow-diagram of the FoamFish module. Items in purple flow from the general physical model used. Items or functions in gray are implemented within Step 1, whereas items or functions in white are already implemented in Step 0.

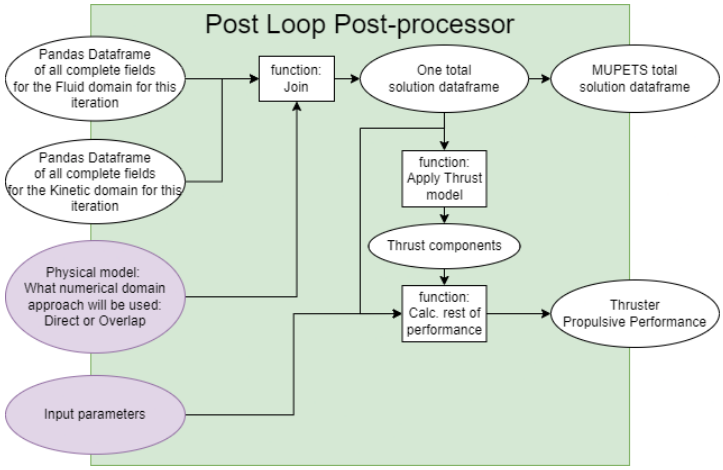

Figure 7.7: The flow-diagram of the Post-processor that is run at the end of the MUPETS code. Items in purple flow from the general physical model used. There is no difference between Step 0 and Step 1 implementation here.

OpenFoam. Particles are then randomly sampled and injected at the boundary. The speed with which they are injected is sampled from the VDF of the species. This VDF is assumed to be a Maxwellian distribution function at the species temperature $k_B T_I$[73] and offset by the species drift velocity u_I. T_I and u_I are taken as the area-averaged species properties at the domain interface. The assumption of a Maxwellian distribution for the initial velocity should still be a close enough approximation as it concerns species that are on the border of the fluid and kinetic regimes, thus still being in (near) thermal equilibrium. After the particles are injected, their motion is governed by equation (7.17) and collisions as described in section 7.2.1.

FishFoam

As described in section 7.2.2, when using the kinetic solution in an iterative loop to remove assumptions on species velocity at the domain interface, the BCs on the potential and on the electron density are changed after each iteration h. Thus equations (7.23) and (7.24) need to be implemented in the new starting conditions of OpenFOAM before a new simulation is run. To converge to the new solution of $h+1$ faster, rather than correcting the initial conditions of h with the new BCs, the converged solution of h is corrected instead by including the new BCs. As the old solution is likely closer to the new solution than the initial conditions, this should result in a faster convergence. equation (7.23) is carried out by rewriting the equation formulation of the BC for electrons. Prior to the correction, its formulation was following the Bohm criteria, which was also equation-based. Now instead, the velocity is no longer assumed to be the Bohm velocity, rather the already used assumption of charged flux equality at the interface is used directly to set the electron flux equal to that of the ion flux. This removes one assumption from the coupled model. Meanwhile, equation (7.24) is carried out by directly setting the potential gradient from the kinetic model at each domain interface boundary surface center in OpenFOAM. For this, both model meshes are obtained at the interface to interpolate the values from the kinetic model on the mesh of the fluid model. In addition, due to the noise of PIC modeling, a derived quantity such as the electric field, which stems from the negative gradient of the potential (which itself depends on the distribution of charged macro-particles), will be very noisy and unstable as shown in figure 7.8. Therefore, curve-fitting of an exponential function is applied to each axial potential profile on the kinetic domain, at each radial position of the fluid mesh. The gradients of these fitted profiles at the interface then are used directly as the plasma gradients to be set as the BC for the fluid model at each respective surface center. As already explained in section 7.2, passing more direct field values has been attempted but has not yet led to a stable solver. If a stable coupling for more field values can be achieved, the electron density should also be passed back to the fluid model as that would remove the dependency on the assumption of net neutral flux at the domain interface. This assumption would then only remain present at the free space boundaries of the kinetic domain.

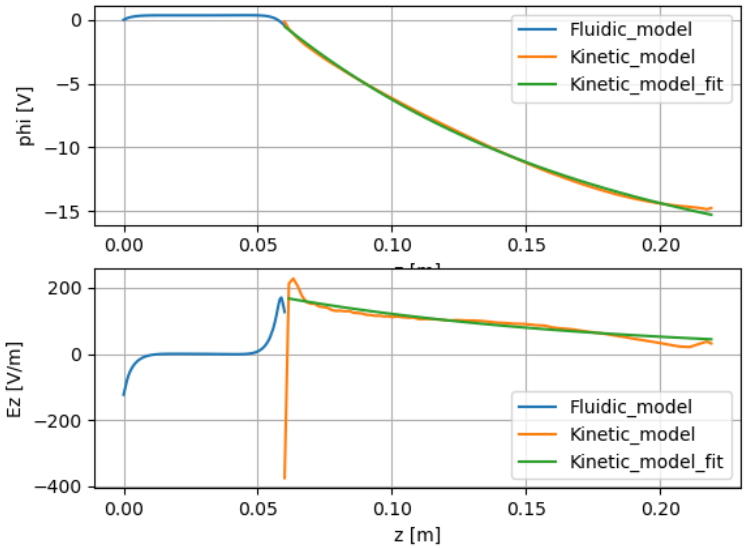

Figure 7.8: Average kinetic electric field profile along the axial length of the thruster, including the profile of the negative derivative of the curve-fitted potential line. Note that the first very negative value of the Kinetic Ez value stems from a virtual cell that is placed before the injection source in the kinetic domain, and therefore is non-physical.

7.3.3. Iterative loop

The iterative loop is simply conducted by linking the FishFoam module back to the Fluid module, hence updating the final BCs of the plasma potential at the domain interface. This is continued until a convergence criterion is met. This criterion shall be related to the convergence of a certain plasma flow property, ideally one which strongly drives the solution. That way, it can reasonably be expected that when this property converges to a stable solution, meaning the change in the solution between its current and previous iteration is below a certain threshold, any future iterations shall likely not yield a solution differing more than this threshold.
The chosen plasma flow property on which the criterion shall be placed is the electron density, as this property strongly drives the solution of the model. The criterion itself shall be that the difference in the axial electron density profiles between iterations should be lower than the general measuring uncertainty of the electron density current in experiments, which is 10%[10], [11].

Results of earlier iterations can be extracted from the MUPETS code while it is still running. This allows inspection of the run and model performance, as well as preliminary analysis of results before the end of a run.

7.3.4. Numerical Domains

The numerical domains on which either the kinetic or fluid model are applied each represent the region in which the plasma behaves according to a specific regime, kinetic or fluid. They are distributed over the modeled thruster geometry, consisting of the source chamber and the magnetic nozzle, as well as the surrounding free space. The distribution is governed by the location of the kinetic and fluid regime themselves, separated by the regime transition boundary across which the plasma transitions from the fluid regime into the kinetic regime. For Step 0 and 1, This transition is assumed at the outlet of the source chamber, coinciding with the throat of the magnetic nozzle. At this location, previous numerical analyses usually assume the Bohm condition[80], [89] although different velocities have been observed as well[81], and Step 1 removes this assumption. Step 2 would include the mapping of this transition boundary upon the full thruster domain based on the value of the Gradient Length Local Knudsen Number as explained in section 7.2.2, and the re-meshing of the numerical domains between parent-iterations. Step 2 however could not be implemented numerically in time and hence has been left for future work.
The simplest way to couple the numerical domains is to couple the domains directly at the domain

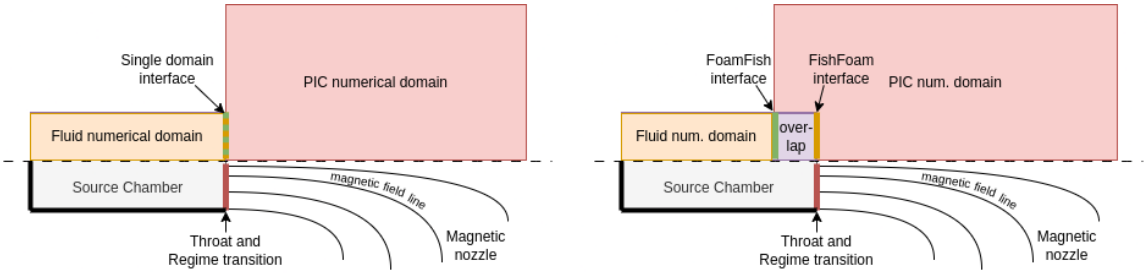

(a) Direct domain coupling method

(b) Domain overlap region coupling method

Figure 7.9: Numerical domains coupling schemes

interface, at the boundary of each numerical domain. However, due to the necessity to contain the computational cost of the PIC simulation within the kinetic model, the minimum kinetic cell size approaches the Debye limit for PIC simulations[86]. When this is combined with neglecting collisions in the plume, again to reduce computational cost, a numerical instability in the first cells adjacent to the particle injection source is observed, which resolves itself after a few cells.
In order to resolve this, an additional numerical domain coupling method was considered as an alternative: the overlap method. Overlapping numerical domains is possible, as long as the solutions in a kinetic regime are obtained through the kinetic model. Solutions in the fluid regime can be obtained from either model, as the fluid model is a simplification of that of the kinetic model[47], although utilizing a fluid model is preferred for lowering the computational burden.
This allows for a second coupling method, which overlaps the kinetic domain onto the fluid domain, giving the kinetic flow more space to stabilize. These numerical domain coupling methods are separate from those considered in Step 2, and only exist for the sake of numerical stability and not for the sake of the higher regime-fidelity striven for in Step 2. Each method will be elaborated upon in the rest of this section.

Method 1: Direct coupling with a field shift

If collisions in the plume are included in the simulation, as will be done for the validation of the coupled model, no numerical instability occurs near the domain interface. The domain interface simply lies at the outlet of the fluid domain and at the injection surface of the kinetic domain. The direct domain coupling scheme is shown in figure 7.9a. If however, in order to reduce the computational cost, as will be done for the verification of the coupled model, collisions in the plume are neglected and the numerical instability in the first cells occurs. the PIC results will then need to be shifted along its domain for the first 10 cells. This removes the dependency on these unstable cells while introducing a small spatial error into the values in the plume.

Method 2: Overlap region

The overlap region is created in front of the regime transition by extending the kinetic numerical domain across it into the fluid numerical domain. This splits the domain interface into two parts. The FoamFish module spatially starts at the outside boundary of this overlap, while the FishFoam module will start on the border that is aligned with the regime transition. This second method allows the kinetic module to mature its flow solution in a region where the flow is still in the fluid regime, meaning the total solution can be taken from the fluid module, and is therefore nowhere in the model dependent on the initially unstable solution of the PIC code, as the fluid code covers for it. The potential gradient is passed to the fluid model only at the boundary of the overlap region which aligns with the regime transition. The domain overlap coupling scheme is shown in figure 7.9b. Furthermore, this allows the PIC model to inject particles not only at a single source surface, but instead use the overlap region as a source volume. This could further help reduce instabilities. It is important to note that this is a different coupling method from the buffer-region suggested for the regime mapping in section 7.1.3, as no shared solution would be used. The overlap region exists solely to better initialize Starfish. However, both methods can be implemented together.

8

Results: Verification, Validation and Comparison

The previous two chapters defined the model both physically and numerically and proposed two variations for coupling the numerical domains, direct numerical domain coupling and overlapping region numerical domain coupling. Before further use, the model now has to be verified and validated. This chapter will address the research question's second sub-question, "How can the coupling methods be compared?" and present the methods of verification, validation and accuracy comparison employed in this thesis. The verification thruster has simple, generic geometry which has been previously used in the development and verification of other RF thruster solvers at the universities of Padova and Bologna as the simple setup guarantees a smooth convergence for most solvers. A separate real thruster geometry and set of operating parameters is considered later in the validation case, which is based upon a recent laboratory thruster of the university of Padova, the Regulus thruster[90], [91]. A few non-APT cases were simulated as well during the verification and validation of MUPETS to test its applicability to a broader use-case. These cases can be found in appendix A.

The MUPETS code tracks a large amount of plasma flow properties, such as the densities of all species, the electron temperature, the fluxes of the species, the velocities, and much more. In order to compare differences and observe trends across simulation cases, a selection of the most important properties must be made which will be used as the metrics for comparison and discussion. The coupled model is most sensitive to the properties that form the principle inputs and boundary conditions of the fluid and kinetic models. Of these, the species densities and the plasma potential drive the physical coupling as described in section 7.2.2 and the fluid model has specifically shown itself to be most sensitive to the plasma potential and the electron density. This is because these, by virtue of the electron's low mass and therefore speed, are prone to rapid changes over the time-steps of the model. Therefore, the discussion of the plasma properties shall focus primarily on the profiles of the electron density and plasma potential.

8.1. Verification experiments

Verification of the two variations of the coupled model, have been carried out through numerical experiments that are then compared with theory and other modeling results. Three verification cases have been considered, each with the same thruster geometry and operating parameters, but with different applied magnetic fields.

The simulated verification thruster has a source chamber radius and length of $10\,\mathrm{mm}$ and $100\,\mathrm{mm}$ respectively. At one end, the inlet, a constant mass flow rate of $100\,\mu\mathrm{g\,s^{-1}}$ neutral Argon atoms is injected into the thruster. The simulation case operates at an input power Pw of $50\,\mathrm{W}$. These values are chosen to closely resemble those of earlier simulations and experimental measurements on laboratory thrusters operating on Xenon at the university of Padova[9] to allow for relative comparison. The use of Argon instead of Xenon was carried over from previous verification efforts by the university of Padova,

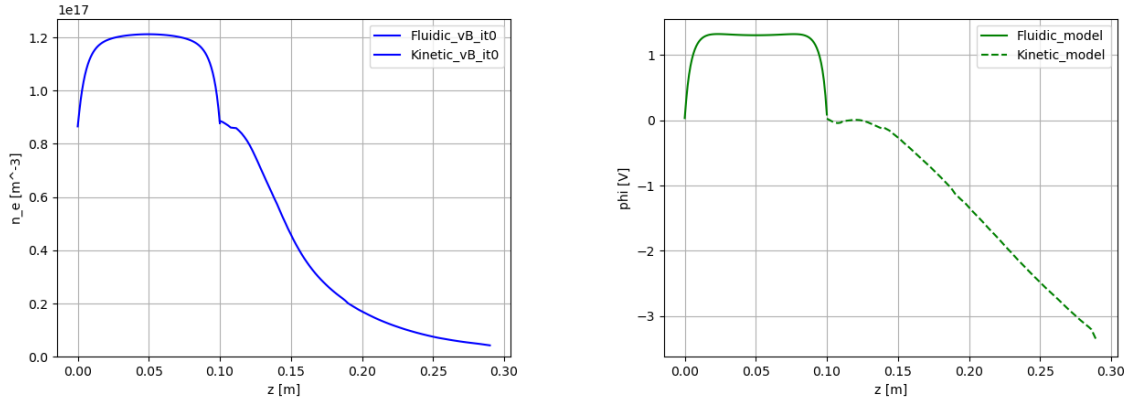

(a) Electron density n_e

(b) Plasma potential ϕ

Figure 8.1: Case 0: No magnetic field applied. Area-averaged plasma property profiles along the axial thruster length z. Results are from Step 0.

with the necessary chemistry coefficients[92]–[96] already having been implemented in the used fluid model. The chemistry coefficients for Xenon[96]–[102] are only introduced into the model during the validation process, as described in section 8.2. For the verification cases, collisions in the rarefied plume are neglected to reduce the extended run-time of each case. These collisions have, however, been included in the validation case for increased fidelity. The cases are divided according to their magnetic field strength and topology in the following manner:

Case 0: No magnetic field (NoB)

Case 1: Uniform B field in source chamber (UniB)

Case 2: Realistic B field in source (Coiled)

The specifics of each case will be explained in the following sections.

8.1.1. Case 0: No magnetic field (NoB)

This case refers to the condition in which there is no magnetic field applied in the thruster domain: neither in the source chamber nor in the magnetic nozzle. With no magnetic field to reduce diffusion to the source walls or guide the expansion of the plume, ambipolar diffusion is expected to dominate. This case is used for early verification of the first instances of the coupled model with only Step 0 included. This allowed easy functionality testing of Step 0 in a simple configuration before upgrading the model to Step 1 and conducting the standard verification tests with Case 1, the UniB case. The results of the Case 0 simulation can be seen in figures 8.1 and 8.2. Of main interest, and of importance to the successful verification, is the traditional, diffusion-expanded round plume seen outside the source chamber in figure 8.2a, as well as the lower plasma densities in figure 8.1a due to larger losses at the wall. Both these phenomena agree with the expected behavior and performance of the plasma source and plume when no containing and guiding magnetic field is applied. Comparing the low maximum plasma density obtained here with the higher densities later obtained in Cases 1-3, will show the benefits of applying a magnetic field to the thruster.

8.1.2. Case 1: Uniform B field in source chamber (UniB)

After verifying the basic functioning with the very simple NoB case, further verification is done with a case which, although still a simplification, approaches a realistic thruster. Benefits of this UniB case are that not only that the plasma profiles can be verified against other numerical results and be compared to theory, but also the obtained thrust can be used as an order-of-magnitude validation when compared to general APT performance.

For the UniB case, the magnetic field B inside the source chamber has the simplified value of an ideal, uniform field in the axial direction with a value of $0.05\,\mathrm{T}$. Outside the source chamber, the B field diverges as a realistic magnetic nozzle. This magnetic field is shown in figure 8.3.

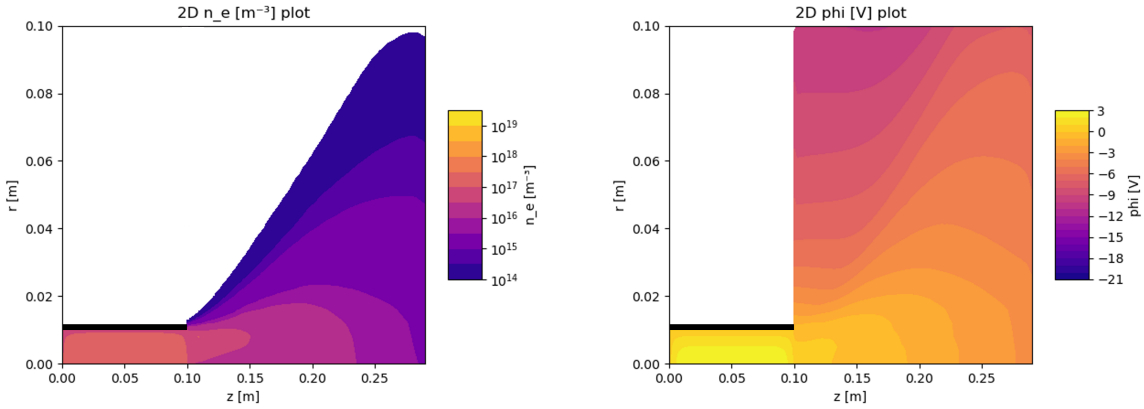

(a) Electron density n_e

(b) Plasma potential ϕ

Figure 8.2: Case 0: No magnetic field applied. Plasma properties on the full 2D $z-r$ thruster domain. z and r are the thruster domain's axial and radial length respectively. Results are from Step 0.

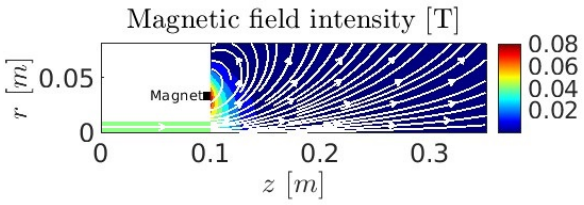

Figure 8.3: Case 1 (UniB) Applied magnetic field strength and topology throughout the whole thruster, including a representative magnet for the field of the magnetic nozzle. In the source the magnet is virtually extended all the way to the back plate ($z = 0$).

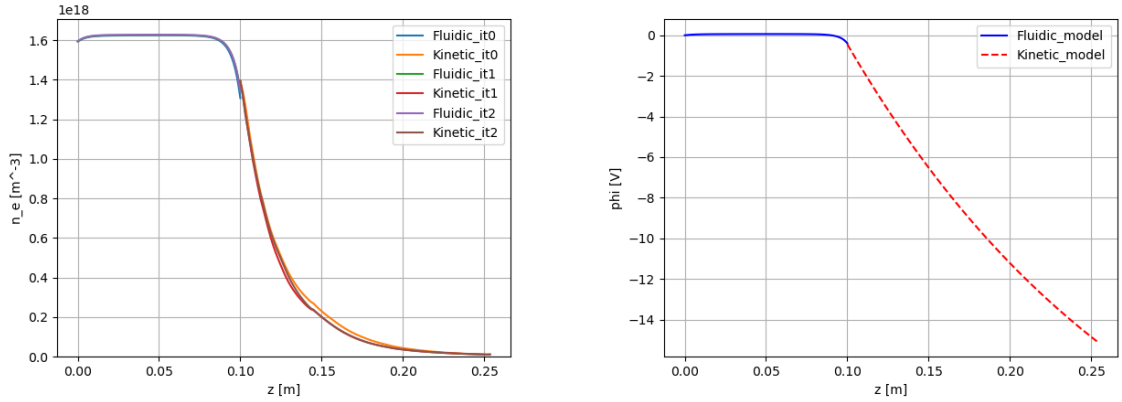

(a) Average electron density n_e

(b) Final converged average potential ϕ

Figure 8.4: Case 1: Axial area-averaged plasma property profiles along the thruster length z

Coupled model results

The average ion and electron densities as well as the plasma potential are plotted along the thruster's axial direction in figure 8.4. Specifically, figure 8.4a shows the solution of the coupled model for three macro-iterations. It is clear that the profiles do not change much during these iterations, suggesting rapid convergence. Looking at the convergence plots in figure 8.6, it can be seen that indeed after the second iteration the electron density profile differs less than 10% everywhere, meeting the convergence criteria. The largest differences exist in the kinetic plume.

After the 0th iteration, all BCs placed at the interface in the initial simulation setup that are not consistent with respect to the full thruster domain are now updated. This will be shown in more detail later. Comparing the plasma density in this case with that of the NoB case, it is seen that the magnetic field significantly decreases plasma diffusion to the walls and associated losses. The maximum electron density reached in the source increases tenfold.

The plasma densities and potential have also been plotted over the full 2D domain in figure 8.5. Comparing these results with the NoB case, it can be seen that the expansion plume now strongly follows the diverging magnetic field lines, rather than the free diffusion in absence of a magnetic nozzle. The plasma potential shows a good match in its 2D profile with other PIC simulations[4], [103].

Interesting to note is that the total plasma potential drop of case 1, shown in figures 8.4b and 8.5b is much larger than the plasma drops of cases 0, 2 and 3 shown in figures 8.1b, 8.2b, 8.10b and 8.11b. This is explained by the larger charged density present in the source which disperses in the plume to infinity. While the axial plasma potential profiles all show slightly different behavior in the near-outlet region of the plume, eventually the ions and electrons each expand in their own distinct manner in the downstream region of the magnetic nozzle, the electrons staying more attached to the magnetic field lines. This causes a drop in the potential when moving away from the outlet. If there are more charged particles, the total magnitude of this charge drop is enhanced. The total charge drop therefore follows the same trend as the source chamber plasma density between cases. Case 0 has no magnetic field applied, causing both electrons and ions to expand more similarly and evenly, resulting in the very small potential drop predicted in figures 8.1b and 8.2b.

Stability of results with different initialization

The great benefit of the iterative coupling is that BC values at the interface have been computed in the previous iteration rather than being assigned assumed values. The performance and numerical robustness of this approach is explored by examining whether the model still converges to a same solution regardless of the initial assumed interface BCs: instead of assuming the electrons to have the Bohm speed at the outlet, as is frequently done[89], a different velocity is imposed as a BC for the initial iteration. Although this value can be chosen arbitrarily, a value of half the Bohm speed, thus $v_e = 0.5\sqrt{\frac{qT_e}{M_i}}$, is chosen to reduce the risk of non-convergence in the fluid model and equation (7.22) is modified accordingly. The profiles resulting from this different initial interface condition are shown in figure 8.7. They demonstrate convergence from this differently assumed interface condition to nearly

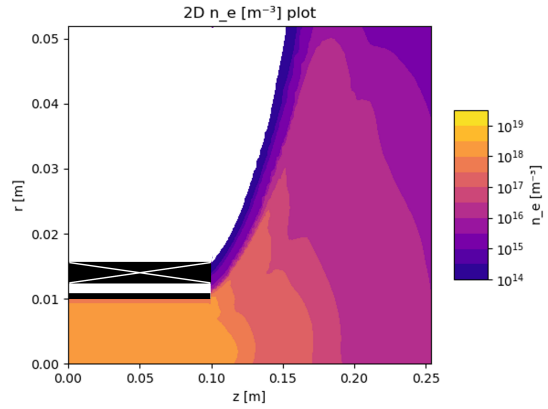

(a) Electron density n_e 2D profile.

(b) Plasma potential ϕ 2D profile. Note the larger potential drop.

Figure 8.5: Case 1: Plasma electron density and potential on the full 2D thruster domain. z and r are the thruster domain's axial and radial length respectively. Note that the representative virtual magnet extends along the entire source chamber to create the uniform B field.

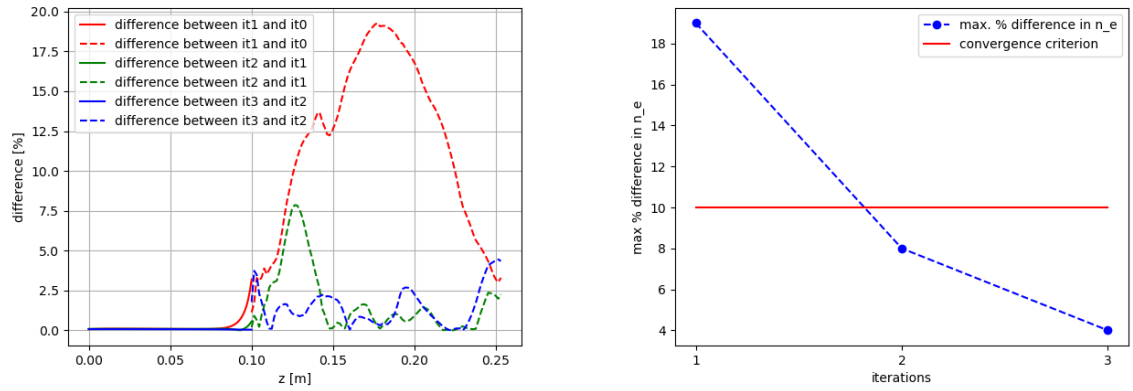

(a) Relative differences of the axial profiles between iterations

(b) Convergence of maximum difference of each iteration.

Figure 8.6: Case 1: electron density profiles converging to below the convergence criterion of 10% difference between iterations, shown as the red solid line in (b).

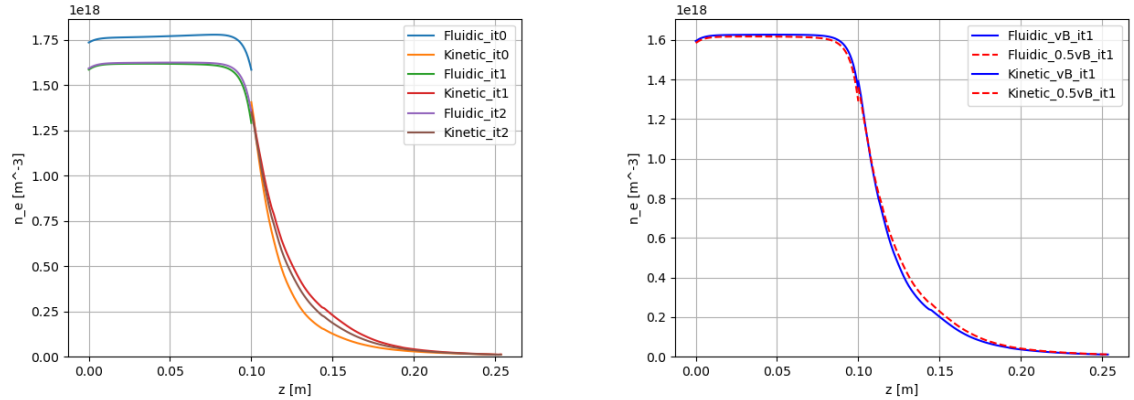

(a) Perturbed initial solution of the area-averaged electron density n_e converging to stable solution within 3 iterations

(b) Final area-averaged electron density n_e profiles of baseline simulation case (blue) and disturbed case (red)

Figure 8.7: Case 1: Axial area-averaged electron densities n_e along the thruster length z, initialized with half the Bohm speed at the domain interface to showcase the stability of the coupled model.

exactly the same steady solution as in the UniB case. Specifically, figure 8.7b illustrating the results of the second iteration of both simulation cases, shows that despite the initial perturbation, the coupled model converges to a stable solution through its iterations. Notably, the two solutions converge at values differing less than 5% in the source chamber and less than 20% in the magnetic nozzle. Furthermore, the magnitude of the final electron velocity at the outlet was found to be just 10% higher than the Bohm velocity at the thruster axis. This agrees with earlier detailed studies into the exact speed at the outlet reporting $v_e = 1.08 v_B$[36] and also shows that the assumption of the Bohm sheath criterion at the outlet, though not exact, is indeed a good first guess. More importantly, this shows that the implemented coupling method has been successful in removing the model's dependency on imposed assumptions at the domain interface, and instead solves the condition at this interface self-consistently for the full thruster domain.

Discontinuities at Source-Plume interface

Earlier attempts at coupling kinetic and fluidic models in the 3DVIRTUS-Starfish numerical suite have encountered non-negligible discontinuities at the interface in the profiles of several plasma properties, most notably the electron density [9]. These have been attributed to the back-flow of electrons being incompatible with the fluid models[4]. When considering the average density profiles near the interface, shown in figure 8.8, it is seen that the kinetic model does still predict slightly higher electron densities than the fluid model at the interface. However, the differences across the interface have been reduced to 1% for ions and 4% for electrons, showing better continuity of the species flow with this method when compared with the area-averaged electron density difference of 7%, obtained with the baseline 3DVIRTUS-Starfish numerical suite[35]. The back-flow is still not successfully accounted for and it is believed that this could be due to the assumptions still in place at the domain interface. Resolution of this issue is one of the improvements that can be made to the BC coupling of the coupled model in the future.

Comparison with overlap method

For the method of creating an overlap region when linking the numerical domains, the same UniB case is run, but with the plasma properties of the fluid model being evaluated at the start of the overlap region, 15 cells before the end of the fluid domain. The kinetic model is then initiated with those properties at that location before the end of the fluid domain. At the same time, the plasma potential gradient used for the solution is taken at the points in the kinetic domain that line up with the end of the fluid domain, such that they can be used as a BC for the kinetic model, as shown in figure 7.9b. It is clear from figure 8.9 that although the electron density gradient seems to agree between models, the solver is not working correctly, as the discrepancies between the fluidic and kinetic absolute values are too great. The initial 0-density value observed in the kinetic profile is due to a virtual cell placed before the injection

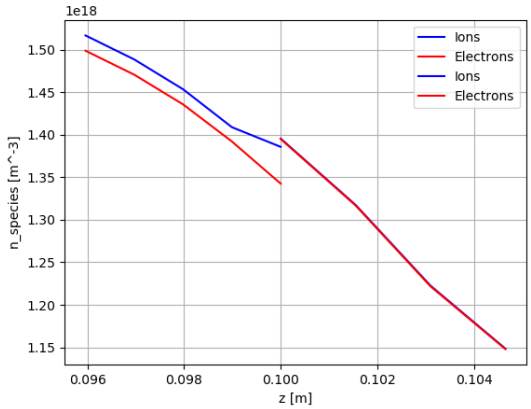

Figure 8.8: Area-averaged ion and electron densities n_i,n_e profiles along the thruster axial length z close to the domain interface. At the domain interface at $0.1\,\mathrm{m}$, a discontinuity exists in both profiles.

source for numerical stability, but the $\approx 1e18m^3$ difference of n_e also indicates an error with the kinetic solver. One hypothesis is that whilst the kinetic solver expects a species velocity in the neighborhood of the Bohm velocity, the velocities taken further inside the source differ too much from this value, causing issues with the incoming flux calculations. Regardless, in its current state the domain overlap method cannot be used for the coupling of fluid and kinetic models. Further work is required to verify the initialization of the kinetic solver. Injecting particles across the entire volume rather than only at the overlap boundary could also be investigated in the future. For now, however, this method will be set aside and the thesis work shall continue with the other method, that of a direct linking of the fluid and kinetic numerical domains at a single domain interface.

8.1.3. Case 2: Realistic B field in source (Coiled)

A more complicated magnetic field with multiple cusps, stemming from the use of coils to generate the field, can also be simulated[9]. Due to the long run-time of each iteration and limited time available to conduct all the numerical experiments in, this case has been tested for just one iteration, thus it can only confirm the expected behavior of Step 0 to test whether complex magnetic fields can be handled in the source and whether the resulting plasma densities, which radial variance shall be more severe, are correctly passed to the kinetic solver. As case 1 has shown that the plasma density profile meet the convergence criteria within the 1st iteration and stably remains under this criteria for multiple iterations thereafter, it was deemed that this expectation could be extended to case 2 as long as the initial density and potential profiles in the near vicinity of the domain interface, where the coupling occurs, is comparable to that of case 1. The results of this simulation can be seen in figures 8.10 and 8.11. As expected, the expansion of the plume in figure 8.11a follows the magnetic field lines as also observed in the UniB case. When looking at the source density in figure 8.10a, it is seen that increased losses at the wall lead to a maximum plasma density that is roughly only 30% of that of the UniB case. This aligns with expectations, as a realistic magnetic field, stemming from a coil, is not perfectly uniform in the source. In these non-uniform regions, the plasma diffusion to the walls is greater than in other regions where the magnetic field restricts diffusion, leading to losses of plasma at the walls which translates to losses in plasma energy. As stated, this case has only been tested for the initial iteration and it can thus not be verified whether the solution would converge afterwards in subsequent iterations. As only the potential gradient is passed from the kinetic to the fluid model, and the gradients at the interface differ little, the general expectation is that the profiles shall remain relatively unaffected, resulting in convergence in subsequent iterations. However, there is no substantial proof for this nor was there sufficient time to run more iterations within this thesis work. Thus, the running of multiple iterations on case 2 has been left for future work.

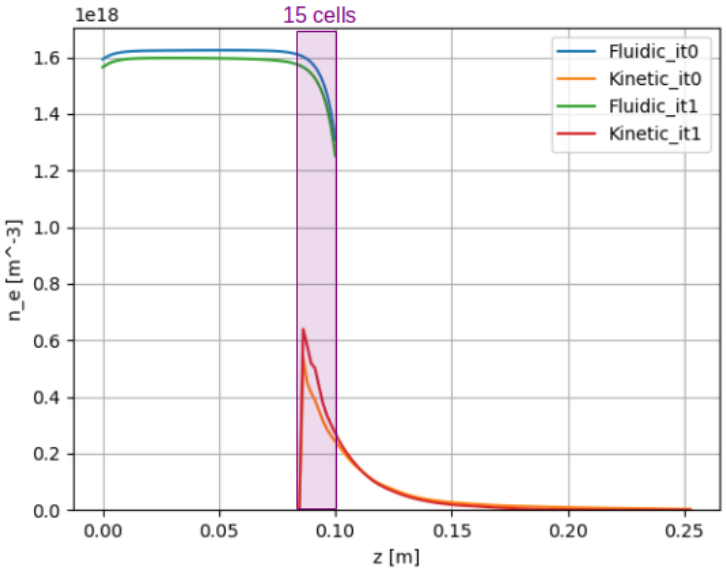

Figure 8.9: Case 1 domain overlap method: Axial area-averaged electron density n_e profiles along the thruster length z. The overlap region spans from $0.085\,\mathrm{m}$ to $0.1\,\mathrm{m}$ and contains 15 cells.

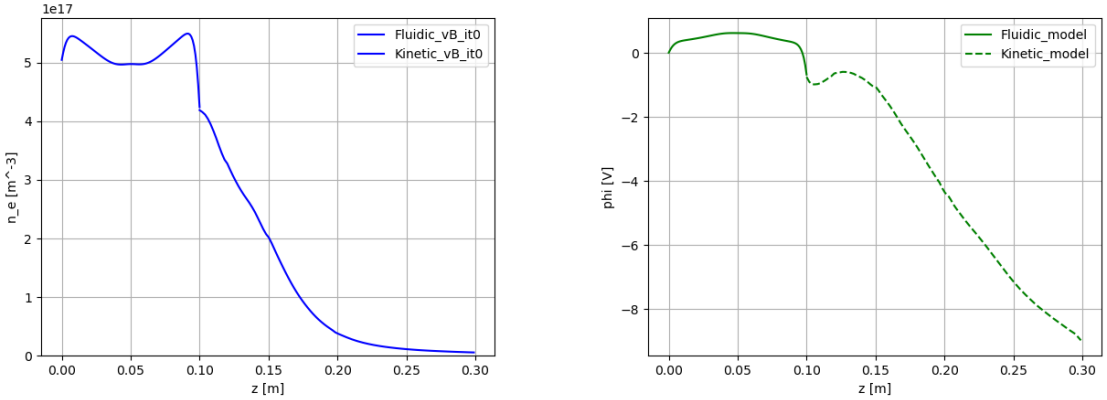

(a) Electron density n_e

(b) Plasma potential ϕ

Figure 8.10: Case 2: Realistic magnetic field applied. Area-averaged plasma property profiles along the axial thruster length z. Results are from Step 0.

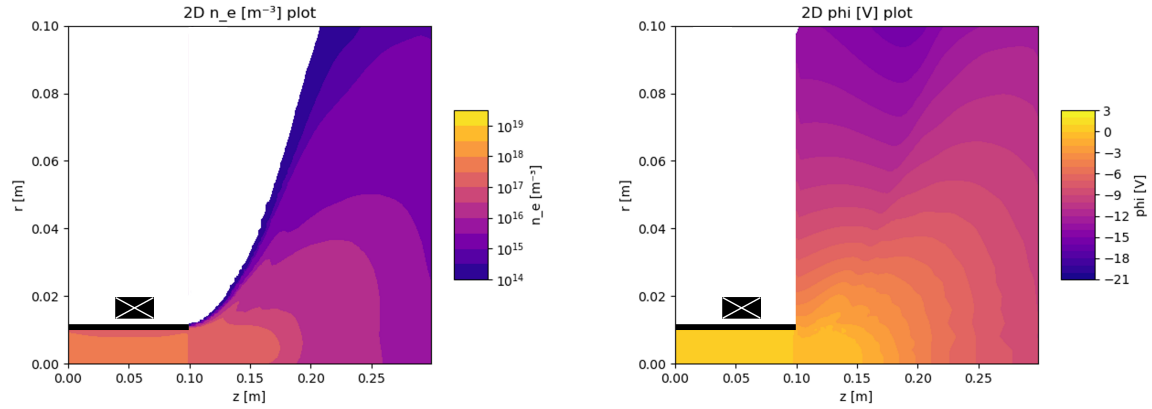

(a) Electron density n_e

(b) Plasma potential ϕ

Figure 8.11: Case 2: Realistic magnetic field applied. Plasma properties on the full 2D $z-r$ thruster domain. z and r are the thruster domain's axial and radial length respectively. Results are from Step 0.

8.2. Validation experiments

Validation of the direct numerical domain coupling method is carried out through the comparison of the model's predicted propulsive performance with the experimentally obtained performance of the tested experimental Regulus laboratory thruster made by the university of Padova. This thruster has previously been modeled by employing the fluid and kinetic models separately[75]. These earlier results shall act as a baseline against which the prediction accuracy of MUPETS can be compared.

8.2.1. Laboratory thruster setup

Reproducing the Padova Regulus laboratory thruster, the simulated thruster has a source chamber radius and length of $7\,\mathrm{mm}$ and $60\,\mathrm{mm}$ respectively. At the inlet, a constant mass flow rate of $150\,\mu\mathrm{g\,s^{-1}}$ neutral Xenon atoms is injected into the thruster[9], [90], [104]. Comparing this validation thruster to the verification thruster, the higher injected mass flow rate and smaller source chamber volume are expected to increase the plasma and neutral density, as well as their respective fluxes. Although the outlet area shall decrease, the thruster performance is expected to still increase due to the higher density and mass flow rate of the propellant.
The Padova experimental thruster used for comparison had been tested at multiple power settings across the low-power range. Therefore the simulated total power P_w deposited into the plasma is tested for this thesis at both ends of the experimental range, at $15\,\mathrm{W}$ and at $57\,\mathrm{W}$. This provides the opportunity to compare the coupled model's performance directly against the previous numerical attempts at $57\,\mathrm{W}$ while also investigating the low-power range more. With the latter functioning as a parameter sweep of the input power, part of the propulsive envelope of the thruster is thus also analyzed.

Two simplifications remain in the laboratory setup. Firstly, the magnetic field's topology and strength were simplified to only have a uniform, axial component. This will however lower the plasma losses to the wall, resulting in an overestimation of the plasma density in the chamber and therefore the predicted thrust. Secondly, as the neutral particles do not gain any energy from the RF antenna, and are not sped up through any potential field, their component of the thrust generally becomes negligible when the ionization ratio lies above 10% as explained in section 4.3. At the considered power range of the laboratory thruster (15W-57W) the ionization ratio lies around 20%[32]. Neglecting the neutral thrust simplifies the setup but results in an underestimation of thrust. Overall the thrust will be overestimated because the contribution of the thrust from neutral propellant is of at least one order of magnitude less than the contribution from the plasma density. For the sake of completeness, a conservative estimation for the resulting total overestimation of the thrust stemming from these two simplifications will be made in section 8.2.3.

8.2.2. Laboratory Thruster results and comparison

When inspecting the plasma profiles, both the axial and 2D profiles for both cases on the low-power range plotted in figures 8.12 to 8.14, the $15\,\mathrm{W}$ and the $57\,\mathrm{W}$ case profiles both align with expectations from theory: the plasma density peaks in the middle of the source chamber, and drops rapidly after the outlet as it expands along the magnetic field lines, where also the plasma potential is seen to drop, all in the same manner as already observed during the verification. The axial profiles in figure 8.12, presenting the area-averaged properties along the thruster's axial length z, show good continuous behavior and the 2D profiles in figures 8.13 and 8.14 show the source chamber and the expansion plume with a similar shape as in Case 1. This is to be expected given the applied magnetic field. More importantly, it can be seen that the plasma density of the $57\,\mathrm{W}$ case has increased significantly, obtaining an area-averaged maximum density of $n_e \approx 2e19$ in the source, as opposed to the $n_e \approx 4e18$ for the $15\,\mathrm{W}$ case.

The 2D simulation profiles can also be compared with other PIC simulations performed by Zhou et al.(2022) shown in figure 8.15. Although the numerical experiment of Zhou et al. (2022) was conducted at a higher power ($300\,\mathrm{W}$), the relative profile shapes can still be used for comparison. Comparing the electron density profiles, the same trends and general shapes appear: a peak in the source chamber, separated from the walls, and a plume diffusion shape which is not governed by classical diffusion (which would be more rounded, as seen in figure 8.2a of verification case 0) but by the magnetic field lines (shown in figures 8.13 and 8.15a by the contour lines showing a stronger radial divergence as their radial position increases).
Additionally, comparing the potential profiles, it is seen in the MUPETS results, which model a larger area of the plume domain than the cone-shape plume domain of the results of Zhou et al. (2022), that two local maxima in plasma potential exist: one in the source chamber and one at a region just radially-outward of the outlet. This is explained as follows: when the plasma exits the outlet, at the start, at short axial distance away from the outlet, the ions will more readily diffuse radially outward than the electrons as the electrons are more attached to the magnetic field lines which do not yet sharply diverge radially. This creates an area of local positive charge, which is seen in the MUPETS results. Due to this, close towards the thruster, the contour lines are shaped by the existence of two local maxima. However, at a distance further away from the thruster, at the edges of the plume domain, these two local maxima will appear to be roughly in the same location. At this distance, the contour lines will be shaped as if there is only one positive charge maxima, and they will behave as $\phi = \frac{1}{\mathbf{r}}$ where **r** is the total distance away from the thruster outlet, not the radius. This transition from the potential field being shaped by two maxima to only one maxima causes a change in the shape of the contour lines when moving away from the thruster. This shape-change is observed both in the results of MUPETS in figure 8.14 and the results of Zhou et al. (2022) in figure 8.15b: The lines start out with a negative tangent shape, $r = -tan(z)$, but about halfway the plume, this shape has turned into a positive tangent shape $r = tan(z)$. Even further away the shape is expected to round off further to a generic arc shape. Thus, the findings of MUPETS agree with both other high-performance models and general plasma physics theory.

Predicted propulsive performance

Neglecting the neutral propellant contribution to thrust, equation (4.12) shall then be used for the calculation of thrust, in which F_{loss} is also considered negligible[5].
Two further assumptions will be made. First, equation (4.14) is rewritten to directly use the azimuthal current density, given by $J_\theta = -qn_e(u_{e\theta} - u_{i\theta})$. Due to the much larger ion mass, the ions gyrate much slower in the magnetic field than the electrons. Therefore $u_{i\theta} << u_{e\theta}$ and the ion contribution to this azimuthal current density is neglected, leading to the simplified formulation of F_{mag}:

$$F_{mag} = \int_V J_\theta B_r dV \tag{8.1}$$

Second, equation (4.13) is approximated by $F_{cham} \approx 2\pi R^2 n_{e*} q T_{e*}$[57] where n_{e*}, T_{e*} and R are the average electron density and temperature at the outlet, as well as the throat radius. The resulting thrust equation is then:

$$F = 2n_{e*} q T_{e*} \pi R^2 + \int_V J_\theta B_r dV \tag{8.2}$$

The predicted thrust from the coupled model is plotted against the experimental measurements of this thruster as well as against the earlier modeling attempts[9] in figure 8.16a. As expected from the higher

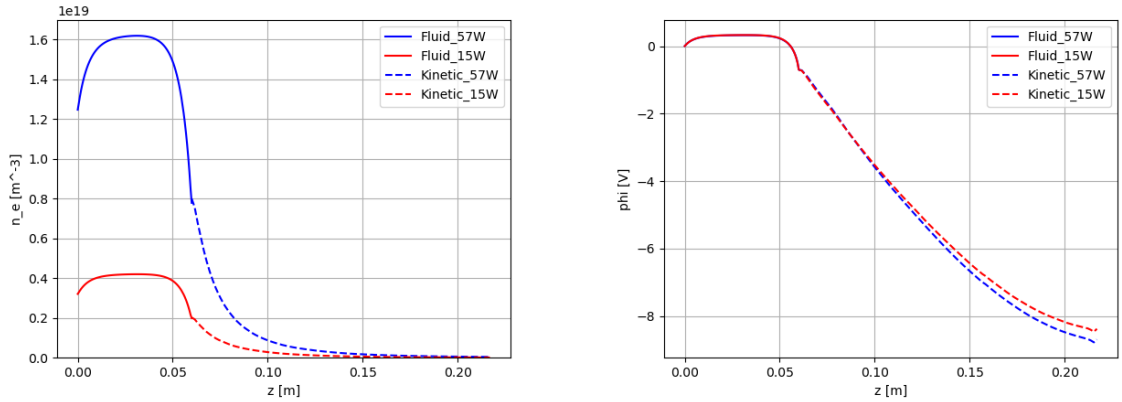

(a) (b)

Figure 8.12: Area-averaged plasma property profiles of the (a) electron density n_e and (b) plasma potential ϕ along the axial thruster length z for the $15\,\mathrm{W}$ and $57\,\mathrm{W}$ cases.

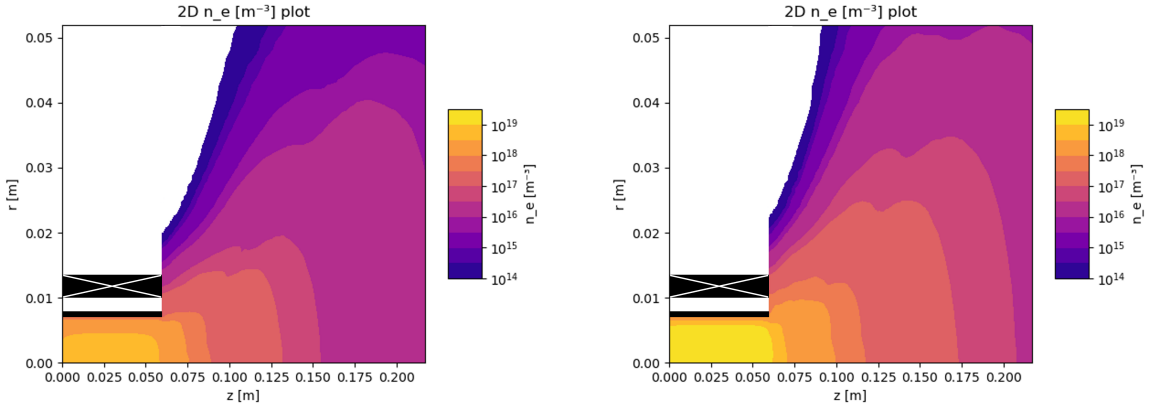

(a) (b)

Figure 8.13: Plasma electron density n_e on the full 2D $z-r$ thruster domain for the (a) $15\,\mathrm{W}$ case and (b) $57\,\mathrm{W}$ case. z and r are the thruster domain's axial and radial length respectively. The representative virtual magnet extends along the entire source chamber to create the uniform B field.

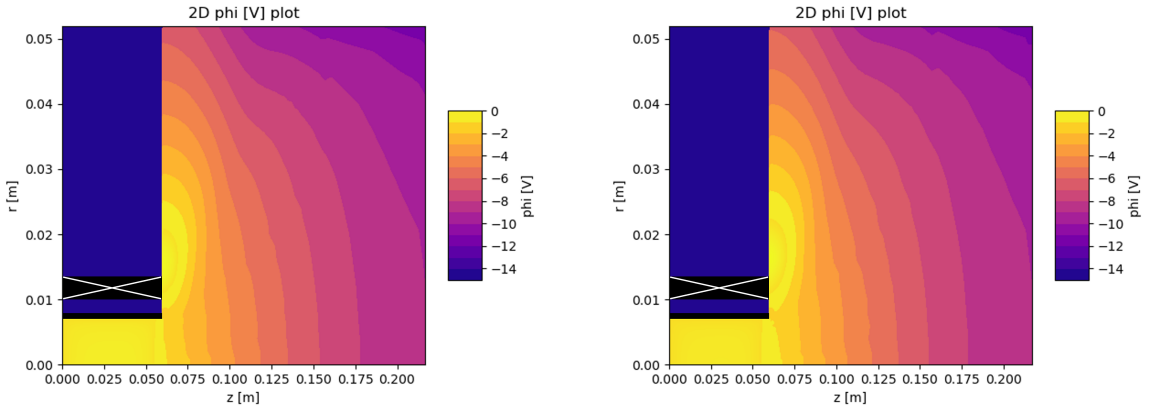

(a) (b)

Figure 8.14: Plasma potential ϕ on the full 2D $z-r$ thruster domain for the (a) $15\,\mathrm{W}$ case and (b) $57\,\mathrm{W}$ case. z and r are the thruster domain's axial and radial length respectively. The representative virtual magnet extends along the entire source chamber to create the uniform B field.

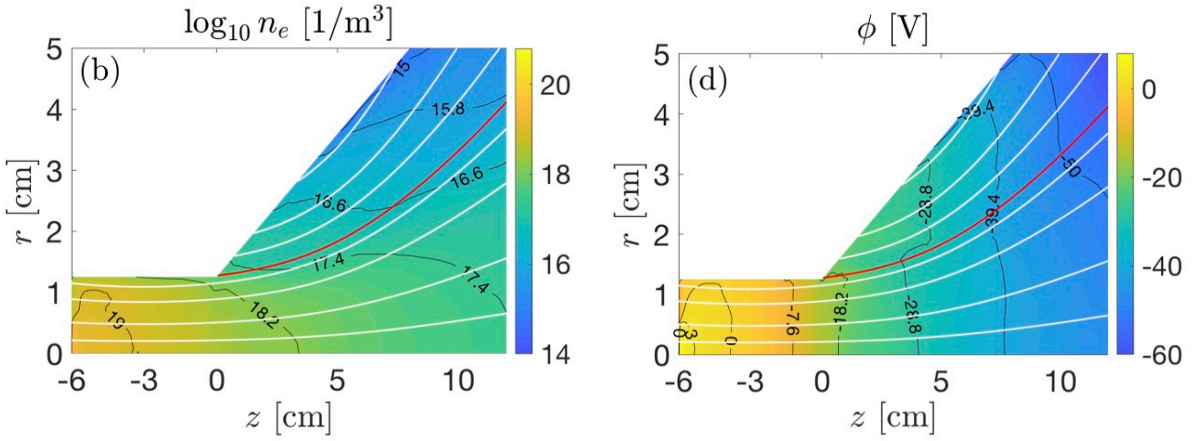

(a) Electron density n_e

(b) Plasma potential ϕ

Figure 8.15: PIC results obtained for an APT by Zhou et al.(2022) for $300\,\mathrm{W}$. The red line represents the most external magnetic field topology line from the source chamber.

plasma density and equation (8.2), the $57\,\mathrm{W}$ case produces a higher thrust level than the $15\,\mathrm{W}$, $1.05\,\mathrm{mN}$ instead of $0.27\,\mathrm{mN}$. More interesting to the validation of the coupled model, however, is the difference between the experimentally measured thrust and the predicted thrust at those power settings. At both $15\,\mathrm{W}$ and $57\,\mathrm{W}$, this difference lies just under 19%. In figure 8.16a both MUPETS points lie above the experimental curve. Compared to previous attempts, where the minimum difference between numerical and experimental results was just below 20% at $57\,\mathrm{W}$[9], the 19% differences of the MUPETS results fall in the same range of accuracy. The validation of the MUPETS performance has now also been extended to the low end of the low-power HPT operating range, showcasing the model's stability and fidelity across the power-range, instead of operating simply at one singular point. This validation is however limited to the use of a simplified magnetic field in the source.

8.2.3. Thrust correction

Two simplifications caused an expected net overestimation of thrust, as previously mentioned in section 8.2.1. The first simplification was made to reduce the complexity of the first validation case to be run. It involved assuming the magnetic field in the source chamber to be uniform whilst the magnetic field in the plume was modeled realistically. This simplification was made with the intent of following up with the more complex magnetic field case should no issues with the initial validation be found. However, at the end of the validation of this first case, the computers on which these cases were run had to undergo maintenance. This made it impossible to run and complete the validation of the realistic magnetic field case within the time-frame of the thesis. Therefore this has had to be left for future work. The magnetic field is therefore assumed to only have an axial, uniform component of $0.05\,\mathrm{T}$ (figure 8.3). This shall cause an overestimation of the plasma density in the chamber as with a realistic magnetic field the plasma losses towards the walls would be larger than those for a uniform axial field, as has been shown in the verification case with a realistic magnetic field applied in section 8.1.3. The second simplification was made in order to compare the thrust predictions against the baseline of the 3DVIRTUS-Starfish model. The contribution of neutral propellant to the thrust was neglected, leading to an underestimation of thrust which is expected to be one order of magnitude smaller than the overestimation due to the uniform magnetic field.

To conservatively estimate the total overestimation of thrust, the following was considered.
First, the neutral thrust component is estimated. Taking this component as $F_n = m_n n_n u_{nz}^2$, the current modeling case cannot be used as the physical nozzle was neglected. Instead, two data-points from another literature simulation case which calculates the neutral thrust component separately are used[37]. These thrust levels are $0.070\,\mathrm{mN}$ and $0.055\,\mathrm{mN}$ for the $15\,\mathrm{W}$ and $57\,\mathrm{W}$ cases respectively. However, this literature case uses argon as a propellant, so to use the neutral thrust estimates, the thrust component is scaled with the ratio of the xenon to argon neutral mass $\frac{m_{Xe}}{m_{Ar}} \approx 3.3$. Therefore, the neutral thrust components for the $15\,\mathrm{W}$ and $57\,\mathrm{W}$ cases are approximately $0.231\,\mathrm{mN}$ and $0.182\,\mathrm{mN}$.

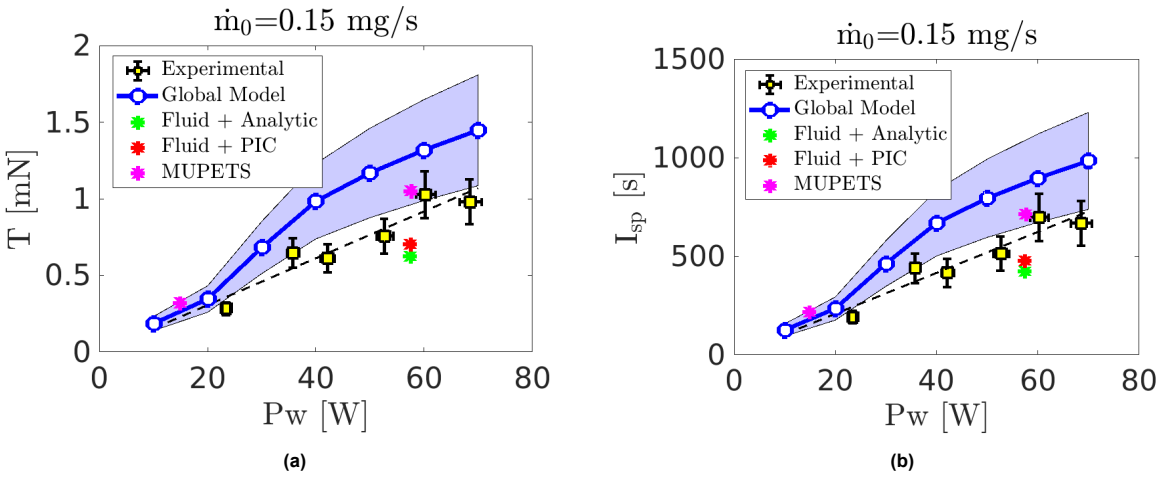

Figure 8.16: Numerically predicted (a) thrust (T) and (b) specific impulse I_{sp} compared against measures, as a function of the coupled power (Pw). Shown are the MUPETS results obtained in this thesis, and the baseline results of previous numerical experiments[9]

Table 8.1: Predicted propulsive performance metrics of the thruster for the preliminary low-power (below $1\,\mathrm{kW}$) parameter sweep against laboratory measurements of the modeled Regulus thruster[7], [9], [16] and other experimental thrusters in the low-power range from literature[5] for reference.

Data	P_w [W]	T [mN]	I_{sp} [s]	η [%]
MUPETS	15	0.27	186	1.7
MUPETS	57	1.05	714	6.4
Regulus lab.	23	0.28	193	1.1
Regulus lab.	60	1.03	698	5.8
Siddiqui et al. (2017)[105]	100	5	146	3.6
Harle et al (2013)[5]	400	1.1	187	0.25
Williams and Walker (2013)[106]	600	6	136	0.67

Based on the results of verification cases 1 and 2, an estimation can be made to the degree of overestimating the thrust due to the uniform magnetic field. Looking at figures 8.4a and 8.10a, it can be seen that the electron density in the uniform magnetic field case is about 3 times as high as in the realistic magnetic field case. As a first order approximation, equation (4.5) is taken to be linearly dependent on the plasma density $n_i \approx n_e = n_p$. Then, it can be expected that the plasma thrust may be overestimated by as much as 3 times the actual value. This shows the need for running the validation case also with the realistic magnetic field, to get a much more representative thrust value to compare to the real thruster data. However, as stated, this was not possible within the time-frame of the thesis and is left as future work.

8.2.4. Propulsive performance over coupled power parameter sweep

In addition to predicting the thrust, the MUPETS code can also predict the propulsive performance metrics defined in section 4.3. The thruster's specific impulse I_{sp}, thruster efficiency η, production efficiency η_p, and propellant utilization η_u are found using equations (4.4) and (4.16) to (4.18). As the validation of the model consisted of two power settings on both ends of the low power regime, this presents a preliminary parameter sweep for the coupled RF power. It is interesting to investigate whether any trends are observed for propulsive performance metrics across the two power settings. The propulsive performance metrics are gathered in table 8.1. It is again clear that the design of APTs is still in its infancy, with very small thrust efficiencies in the power range below $1\,\mathrm{kW}$. For higher power, thrust efficiencies are higher[5], although still limited, with a record of 30% recently being obtained by Takahashi (2023)[8].

It can be seen that an increase in deposited power P_w increases both the thrust T and specific impulse I_{sp} with the same factor. This is to be expected as the propellant mass flow remains the same

at both power settings. Furthermore, the thruster efficiency η and propellant utilization η_u grow with roughly the same factor. As only two data-points have been tested, it cannot be concluded whether the dependency on P_w follows a linear trend or otherwise, but observing the fitted relation of the experimental measures in figure 8.16 it is reasonable to assume a linear relation holds within this power-range, which was also concluded in earlier laboratory experiments[7]. Should this be the case and $T \propto P_w$, then following equation (4.18), $\eta \propto P_w$ which would suggest that the thrust efficiency increases with increasing coupled power, which in general has been observed for efficiencies up to 30%[8]. However, continuing this linear relation implies that the thruster efficiency would eventually surpass 100%, which is not possible. Hence, it is expected that T, and therefore η, only locally depends linearly on P_w. It would be interesting to extend the range of the coupled power sweep to higher powers to investigate how the predicted propulsive performance behaves further away from the investigated range. Note that attention should be given to the realistic amount of power that can be deposited in the plasma. For this, the ADAMANT[76] module has previously been coupled to OpenFOAM[54]. If possible, including this additional coupling into MUPETS could provide additional insight when performing power parameter sweeps. For other parameter sweeps the MUPETS code is deemed most suitable for design parameters which influence the regime transition, such as the physical geometry at the outlet and the magnetic field topology at the magnetic nozzle 'throat'. As the run time is rather long, around four to five days per iteration, the most value is gained from its detailed results and lack of imposed conditions at the throat region. Preliminary effects of other general design parameters which are not expected to significantly impact the regime transition, such as general sizing of the thruster, or injected propellant, could most likely be studied more efficiently through global models.

8.3. Results Summary

An extensive verification and validation campaign was conducted in which multiple test cases were run. For the verification, a generic thruster geometry was considered and was run i) without magnetic field, ii) with an ideal magnetic field, and iii) with a realistic magnetic field applied to it. For the validation, a real laboratory thruster was modeled such that the performance could be compared. This was done with a simplified uniform magnetic field applied to the source chamber, due to time restrictions.

The MUPETS code has shown it can predict accurate axial and 2D profiles, aligned with expected theoretical trends and numerical results. It's improvement over other multi-regime coupled models lies in that initial assumptions made at the domain interface between the fluid and kinetic domains are self-consistently corrected through the iterative loop.

As a result of the novel coupling, the discontinuity of the electron density at the source outlet, identified in earlier coupling attempts[9], has been reduced from 7% to 4%. Using a convergence criteria of electron density remaining within 10% between iterations, the coupled model converges after 2 iterations.

Then, using a simplified simulation case, the predicted performance is compared to real experimental values and other thrusters. The accuracy in predicting the propulsive performance, when compared to the experimental trend, lies in the same accuracy range ($\approx 20\%$ error) as earlier modeling attempts[9] but is overestimated, as opposed to underestimated, due to the simplifications applied. Therefore, the model will have to be run using a more accurate B field case, for which there was not enough time within the thesis (due to the unplanned unavailability of the required computers). It is important that this case is still run accurately in the future, to quantify the actual performance prediction. Based on the outcomes, further work to improve the accuracy of the model may be identified. Two such suggestions could be the inclusion of the EM module ADAMANT[76] that was integrated into the baseline, and the adaption of a more complete thrust equation.

9

Conclusion

9.1. Conclusion

Triggered by the observation that there are several limitations in current models for APTs, it was conceived that several of these limitations and inaccuracies could be reduced or removed altogether through the development of an improved, coupled model. These observations stimulated researching the subject of this thesis paper. The main research question (RQ), the associated sub-research questions (SRQs) and their respective sub-sub-research questions were the following:

RQ. What physically appropriate numerical coupling method between the plasma fluidic and kinetic solvers can provide more accurate results in a multi-regime APT model when compared to APT experimental results?

SRQ1. What coupling methods will or can be tested?

1.1 What are the most important coupling methods between fluidic and kinetic plasma models, applicable to an APT?

1.2 Which of these are physically appropriate?

1.3 How can these be made numerical?

SRQ2. How can the coupling methods be compared?

2.1 What metric will be used to evaluate accuracy?

2.2 How can the coupling methods be verified?

2.3 How can the resulting MUPETS code be validated?

In order to answer the main research question RQ, SRQ1 and SRQ2 must be answered, together with their own sub questions. This will be done below.

What coupling methods will or can be tested? To couple the fluid 3DVIRTUS model[2] and kinetic Starfish[32] model, the coupling methodology, consisting of several methods, has to be chosen. First a choice of which methods to focus on must be made, after which the question of how the methods can be integrated into the physical frameworks used by both models must be answered. Finally these methods must also be numerically implemented into the MUPETS code in order to yield results.

What are the most important coupling methods between fluidic and kinetic plasma models, applicable to an APT? The coupling methods relevant to addressing the limitations in the coupling of the baseline 3DVIRTUS-Starfish APT numerical suite can be grouped into distinct categories. These are: i) methods to increase the fidelity of the state of the plasma that is coupled between models, ii) methods to maintain the continuity of the plasma transport and the self-consistency of it's solution across the models domain interface, iii) methods to more correctly and efficiently distribute the numerical domains onto the full thruster domain and iv) methods which extend the

power coupling to the entire thruster domain. This last method lies outside the scope of this thesis due to it being a EM-wave problem.
For evaluating the suitability of the first three coupling methods they were implemented in a stepwise approach: Step 0 corresponding to method i, Step 1 to method ii and Step 2 to method iii.

Which of these are physically appropriate? It was found that all three methods investigated through the stepwise approach were physically appropriate. Step 0 is made appropriate by transferring radially varying boundary conditions across the domain interface between models. Step 1 loops back the plasma potential from the kinetic to the fluid solver thereby removing boundary condition assumptions made in the initial iteration. Step 2 redistributes the domains based on regime mapping following from the Knudsen value to ensure that the domains accurately represent their respective regimes.

How can these be made numerical? The physical coupling methods described can be made numerical almost exclusively through the post- and pre-processing of the outputs and inputs of the numerical fluid code *OpenFOAM*[2] and the numerical kinetic code *Starfish*[32], [73]. A custom overencompassing python code has been written for this, the MUlti-regime Plasma Equilibrium Transport Solver (MUPETS). It numerically implements Step 0 and Step 1, while Step 2 could not be implemented within the time-span of this thesis.
MUPETS exists of 4 modules: A fluid module which pre- and post-processes, and runs OpenFOAM, a FoamFish module which couples the results to the setup of the next Starfish case, a Kinetic module which pre- and post-processes and runs Starfish and finally a FishFoam module which couples those results to the setup of a next OpenFOAM case. The coupling of the numerical domains follows the two possible methods previously described: either a set surface can be used as a single domain interface, lying at the boundaries of the fluid and kinetic numerical domains, or the kinetic domain overlaps onto the fluid domain, creating one domain interface at the boundary of the kinetic domain which lies inside the fluid domain, where FoamFish is run, and one domain interface at the boundary of the fluid domain which lies inside the kinetic domain, where FishFoam is run.
For the implementation of Step 2, regime mapping could be used to redefine the numerical domains before the pre-processing of OpenFOAM occurs between iterations. This mapping has been left for future work.

How can the coupling methods be compared To find a best coupling method, chosen methods need to be compared. This needs to be done according to a clear metric, after the methods have been verified and validated to ensure that they are behaving as intended.

What metric will be used to evaluate accuracy? When considering the metrics to investigate the performance of the model in terms of continuity and self-consistency, several of the driving variables can be considered. The driving variables of the models are the plasma species densities, energies and plasma potential. The coupled model is most sensitive to the plasma potential and the electron density, which both can change much faster than the high-inertia heavy species densities. Therefore, the profiles of the electron density and plasma potential, both for the average quantities along the axial z length as well as for the full axial and radial z, r profile, have been compared against theory and expectations based on other models. Furthermore, when comparing against the baseline 3DVIRTUS-Starfish numerical suite, accuracy shall be considered in terms of difference between numerical prediction and experimental measurement of the propulsive performance.

How can the coupling methods be verified? Four Argon-fed thruster test cases were defined for the verification, each with an increasingly complex magnetic field. Each of these was simulated using the MUPETS code and trends in the resulting plasma profiles were analyzed and compared to profiles previously obtained in other research. While the first coupled model, with a singular domain interface, could be verified against theory and other numerical experiments, the second coupled model, with an overlap region and two domain interfaces, failed the verification. On account of this failure to verify, the remaining work of the thesis focused on the first coupled model. With the direct domain numerical coupling implemented, it was also shown that the velocity at the domain interface was self-consistently corrected through the iterative loop, removing the assumed velocity imposed there.

How can the resulting MUPETS code be validated? Validation was conducted through comparison of the predicted propulsive performance with measured experimental performance of a laboratory thruster at the university of Padova. This thruster, using Xenon as propellant, had been tested at multiple power settings across the low-power range. The numerical code was tested at both ends of this low-power range, at $15\,\mathrm{W}$ and $57\,\mathrm{W}$ respectively. Using a simplified, uniform magnetic field topology in the source chamber and neglecting the neutral gas thrust, the predicted thrust errors fell below 19% at both ends of the low-power operating range, showing similar accuracy as the 20% errors found by previous models which had simulated the same thruster[9], [104]. However, to obtain a true validation of the accuracy of the predicted performance, a non-simplified magnetic field case needs to be simulated, without neglecting the neutral gas thrust. Furthermore, the obtained results acted as a preliminary coupled power parameter sweep which showed, as expected from theory and experimental results, an increase of the thruster performance in terms of thrust T, specific impulse I_{sp}, thruster efficiency η and propellant utilization η_u with an increase in RF power coupled into the plasma.

RQ: What physically appropriate numerical coupling method between the plasma fluidic and kinetic solvers can provide more accurate results in a multi-regime APT model when compared to APT experimental results?

Returning to the main research question the thesis work yields a single, clear result:
the method of coupling the distinct models, their BCs and domains directly across a single domain interface inside of an iterative loop more accurately models the plasma behavior throughout the whole APT thruster than other coupling methods researched, especially across the thruster's outlet. However, further investigation into the thrust model is required if the propulsive performance predictive capability is to be improved, especially when considering complex source chamber magnetic field topologies.
The resulting MUlti-regime Plasma Equilibrium Transport Solver, MUPETS, presents a novel improvement in APT modeling. The strength of MUPETS lies in its high accuracy and faithful representation of the thruster's outlet section. This has been achieved by reducing the amount of assumptions imposed at this location, such as the condition of sonic velocity for the plasma and neutral gas. It can be used for the further study of electric propulsion or other plasma applications where it is important to consider multiple regimes, or specifically a transition between these regimes.
The numerical implementation of this coupling method in the MUPETS code has been successfully verified for both simplified and complex magnetic field topologies, and has been validated with experimental results obtained from a laboratory thruster for a simplified magnetic field topology in the source chamber. MUPETS shows improved accuracy for the plasma profiles throughout the thruster through the higher fidelity-coupling at the domain interface. The macro-iterations that are run in MUPETS have a long run time of roughly five days but the iterative loop rapidly converges, in general after its second iteration.
For the simplified source chamber magnetic field topology, it also shows similar accuracy in predicting the propulsive performance compared to earlier models. The model has yet to be validated with more complex source chamber magnetic field topology however, and preliminary estimations show that the predicted thrust is currently overestimated.
This coupled model can act as a framework for future improvements on the coupling as well as the fluid and kinetic models themselves. Due to the minimal alteration of the separate models, they can be swapped out with higher-fidelity models or numerically better performing models as required, without altering the required physical methodology. Only the numerical methodology may need to be adapted to interface with potential new solvers. Due to this, many previously developed and validated models from literature could also be compared in this framework to investigate their suitability for describing the plasma flow across the regime change.

9.2. Future Work and Recommendations

Below is a gathering of future work already in progress, planned, or actions recommended.

Realistic Laboratory Thruster Validation

As shown in section 8.2.2 the validation of the thruster performance has been conducted while neglecting the neutral thrust component and with a simplified, uniform magnetic field inside the source

chamber. Conservatively estimating the difference between the simplified magnetic field and a realistic magnetic field, it was found that the thrust could be as much as three times lower from the found values. To remove this uncertainty, it is therefore required that the realistic thruster case is simulated fully, with the complex magnetic field topology stemming from the use of coils modeled accurately and the neutral thrust included. While this was planned to be conducted within the scope of this thesis, long run times and unavailability of the computers on which the model was run at the end of the validation prevented this simulation case from finishing in time, thus leaving only the simplified predicted propulsive performance for validation. Therefore, the realistic case must still be run and validated before continuing work on other improvements in the future, to identify any other shortcomings that may still be hidden in the model's performance.

Thrust Prediction Accuracy

Tying into the previous point, one question that would have been beneficial to investigate is that of the accuracy of the method of predicting the thrust in the MUPETS code. Using equation equation (8.2) neglects the neutral thrust and separates the plasma pressure of the source chamber from the plasma pressure on the magnetic field. Instead, one can also calculate the total momentum and pressure terms of the general thrust equation at the edges of the domain using the following equation[4]:

$$F = \int \int_{S_B} \sum_k (n_I m_I v_{Iz} \mathbf{v}_I + p_I \hat{\mathbf{z}}) \cdot \hat{\mathbf{n}} dS_B \tag{9.1}$$

S_B denotes the open domain boundaries of the kinetic domain. $I = i, e, 0$ denotes the species, including the neutral species. This equation thus does not neglect the neutral thrust. While this equation was considered for use, earlier work with it had shown more numerical noise[4]. Therefore the equation was not further implemented. This equation however follows directly from the general thrust equation, equation (4.1), which should always hold and therefore does not impose any simplifications upon the simulation. Comparing obtained thrust results with this formulation after full implementation would give insight into the severity of the assumptions made in equation (8.2) and should yield a more accurate model.

Full fluid momentum modeling

A higher-fidelity version of the fluid model and code is being developed by the university of Bologna which will model the full momentum equations, rather than assuming the DD assumption. This is done to approach the plasma profiles observed in the helicon piglet reactor[3], [107] in appendix A.0.2 more closely. While the fluid model will thus become more detailed, the updated numerical solver will still be run in the OpenFOAM code with the same input/output structure and handling.The numerical coupling methodology does not need to change for the coupled model. This new fluid solver can be seamlessly integrated into this framework in place of the old fluid solver, in the future.

Integration of an EM-module into the fluid-module

An additional improvement to the accuracy of the fluid module can be obtained through the inclusion of a model for the antenna-plasma power coupling. Instead of assuming a uniform power deposition profile throughout the souce chamber, or any other supposed profile for that manner, the power deposition profile can be self-consistently solved for through the use of an EM-module integrated into the fluid-module. The 3D-VIRTUS code[2] does this with the ADAMANT code[76]. The 3D-VIRTUS code has been developed by the university of Padova and its own fluid model is nearly the same version as the fluid code used in this thesis work. Therefore, integrating the ADAMANT code into MUPETS should be relatively straightforward.

Propulsive envelope study and detailed design modeling

Now that the MUPETS code has been developed, it can be used to study the propulsive envelope of APTs through multiple parameter sweeps. A preliminary sweep of the power deposited into the plasma, P_w, has already been conducted in section 8.2.2. This sweep can be extended to higher power levels to investigate if the propulsive performance continues to scale in a linear fashion, or if the model itself already identifies different behavior at higher power levels. This should be combined with a study into the antenna-plasma power coupling. As suggested in the previous recommendation, this can be done through the coupling of the ADAMANT code into the fluid solver as has previously been accomplished

with the 3D-VIRTUS model.
The coupled solver should lend itself well for detailed studies, especially concerning the design of areas of transition, such as this throat section. To validate this idea, it would be interesting to see if literature exists of experimental studies into different outlet designs appropriate for testing by MUPETS.

Numerical implementation of Step 2

As stated in section 7.3, neither of the coupling methods of Step 2 could be numerically implemented and tested within the time frame of the thesis. Based on ease of implementation, it is recommended that the regime mapping following the Knudsen number is attempted first, as much of the framework already exists. It is possible that problems may arise with the numerical re-structuring of the meshes of both the fluid and kinetic model. Likely a careful numerical strategy of interpolating previous values onto new meshes will be required, together with a strategy to define simplified domain shapes depending on the general regime maps obtained. Should these issues persist, the advantage of the regime buffer method is that this buffer can be made static, thus never requiring any re-structuring of the meshes. However, this will require a more complicated scheme of handling the shared solution in this buffer region.

Investigation of numerical domain overlap method

As discussed during the verification of the different methods of coupling the numerical domains in section 8.1, the method of numerical domain overlap could not be verified as it showed clear and significant discontinuities in the order of $\approx 1e18m^3$ in the electron density axial profile. However, the method's possibility of injecting the kinetic macro-particles across the entire overlap volume, instead of across the single domain interface, holds promise of reducing numerical instabilities in the first cells of the kinetic solution. Hence, a study into the cause of this discontinuity is underway at the university of Bologna. When this problem has been removed and the method can be verified and validated, a comparison can be made between both numerical domain coupling methods in terms of not only accuracy, but also ease of adaptation, for example in the case of including of Step 2.

More efficient simulation case planning

It is recommended for future work that more consideration is given to the purpose and use of each simulation case in the scope of a study. Due to the heavy computational cost of the PIC code, any iteration of MUPETS costs roughly four to five days. Furthermore the PIC code is not optimized for multi-core processing beyond 4 cores. This means that on a single computer, any simulation case takes roughly two weeks to obtain at least a few iterations. It would have been more time-efficient in this thesis if the verification was already conducted on the geometry and operating conditions of the Padova laboratory thruster immediately, or after a bare minimum of early verification cases, rather than after the verification was complete. Then, for example, the realistic magnetic field case in the verification could also have directly been used for validation afterwards with the experimental thruster data.

Numerical optimization of PIC code

Besides better simulation case planning, the optimization of the PIC code to run more computationally efficient would simply reduce the amount of time required per iteration. This allows for more efficient simulation studies where more simulation cases can be run in the same time. Especially when actively developing the coupled model further, the longer the code needs to run, the more time delay there is between when different versions of the code can be tested. This either results in less changes and fewer different versions to be tested, or testing being done in bigger steps, increasing the risk of bugs or mistakes. Improving the code to be efficiently run in parallel on more than 4 cores would already significantly increase the usability of the code, as modern day computers often have 8 cores, and multi-core clusters are available at many universities.

More contingency planning for additional experiments during final writing and validation

During the final reporting of the thesis work, especially during the final post-processing and reporting of the validation work, it was realized that certain simulation cases, such as using a more realistic magnetic field, as well as additional test points in the power range, could have significantly added to the value of the validation and could have given a better basis for more useful conclusions on the value of the model. However, by that time, the computers on which the MUPETS code could be run, were undergoing

maintenance, which was planned to take until after the handing in of the thesis. This prevented the testing of those additional simulation cases, as finding other available computers and setting these up with the required solvers would not leave sufficient time for running the cases themselves. While initially it had not been deemed a problem to have the maintenance start after all intended validation cases were finished, it would have been better to postpone this until the thesis report was fully finished to allow the running of any final cases deemed beneficial.

Clear and Detailed Definition of Baseline Methodology and Implementation

While it was beneficial for the progress of the thesis that a baseline attempt at coupling the fluid and kinetic solvers already existed, the numerical implementation of the methodology was not entirely documented. This caused uncertainties when comparing the MUPETS results to the baseline results, as it was not clear how the thrust exactly had been obtained numerically. This made it difficult to ensure that the MUPETS code utilized the same assumptions, outside of those resolved through improved coupling, and therefore made it difficult to determine whether differences in the results were purely due to the new coupling methods implemented, or due to differences in the thrust equation used or numerical setup. While many parameters can be tweaked for the simulation, and many other field variables need to be set up for initialization, it is important that these are all documented such that one can ensure that they are running the exact same case. To this end, The exact MUPETS code scripts, settings and initialization files used for the $57\,\mathrm{W}$ and $15\,\mathrm{W}$ can be requested from the author at wvlynden@gmail.com

References

[1] E. Dale, B. Jorns, and A. Gallimore, "Future directions for electric propulsion research," *Aerospace*, vol. 7, 9 Sep. 2020, ISSN: 22264310. DOI: 10.3390/AEROSPACE7090120.

[2] M. Magarotto, M. Manente, F. Trezzolani, and D. Pavarin, "Numerical model of a helicon plasma thruster," *IEEE Transactions on Plasma Science*, vol. 48, pp. 835–844, 4 Apr. 2020, ISSN: 19399375. DOI: 10.1109/TPS.2020.2982541.

[3] N. Souhair, M. Magarotto, F. Ponti, and D. Pavarin, "Analysis of the plasma transport in numerical simulations of helicon plasma thrusters," *AIP Advances*, vol. 11, 11 Nov. 2021, ISSN: 21583226. DOI: 10.1063/5.0066221.

[4] S. Andrews, S. D. Fede, and M. Magarotto, "Fully kinetic model of plasma expansion in a magnetic nozzle," *Plasma Sources Science and Technology*, vol. 31, no. 3, p. 035 022, Mar. 2022. DOI: 10.1088/1361-6595/ac56ec. [Online]. Available: https://doi.org/10.1088/1361-6595/ac56ec.

[5] K. Takahashi, "Helicon-type radiofrequency plasma thrusters and magnetic plasma nozzles," *Reviews of Modern Plasma Physics*, vol. 3, no. 1, pp. 1–61, 1 Dec. 2019. DOI: 10.1007/s41614-019-0024-2.

[6] T. Ziemba, J. Carscadden, J. Slough, J. Prager, and R. Winglee, "High power helicon thruster," American Institute of Aeronautics and Astronautics (AIAA), Jul. 2005. DOI: 10.2514/6.2005-4119.

[7] N. Bellomo, M. Magarotto, M. Manente, *et al.*, "Design and in-orbit demonstration of regulus, an iodine electric propulsion system," *CEAS Space Journal*, vol. 14, pp. 79–90, 1 Jan. 2022, ISSN: 18682510. DOI: 10.1007/s12567-021-00374-4.

[8] K. Takahashi, "Thirty percent conversion efficiency from radiofrequency power to thrust energy in a magnetic nozzle plasma thruster," *Scientific Reports 2022 12:1*, vol. 12, pp. 1–13, 1 Nov. 2022, ISSN: 2045-2322. DOI: 10.1038/s41598-022-22789-7. [Online]. Available: https://www.nature.com/articles/s41598-022-22789-7.

[9] M Magarotto, S. D. Fede, N Souhair, *et al.*, "Numerical suite for magnetically enhanced plasma thrusters," in *Proceedings of the 72 nd International Astronautical Congress*, 2021.

[10] D. L. Brown, M. L. Walker, J. Szabo, W. Huang, and J. E. Foster, "Recommended practice for use of faraday probes in electric propulsion testing," *Journal of Propulsion and Power*, vol. 33, pp. 582–613, 3 2017, ISSN: 15333876. DOI: 10.2514/1.B35696.

[11] R. B. Lobbia and B. E. Beal, "Recommended practice for use of langmuir probes in electric propulsion testing," *Journal of Propulsion and Power*, vol. 33, pp. 566–581, 3 2017, ISSN: 15333876. DOI: 10.2514/1.B35531.

[12] R. G. Jahn, *Physics Of Electric Propulsion*, H. S. Selfert, Ed. McGraw-Hill, 1968.

[13] S. Mazouffre, "Electric propulsion for satellites and spacecraft: Established technologies and novel approaches," *Plasma Sources Science and Technology*, vol. 25, 3 Apr. 2016, ISSN: 13616595. DOI: 10.1088/0963-0252/25/3/033002.

[14] I. Levchenko, S. Xu, S. Mazouffre, *et al.*, "Perspectives, frontiers, and new horizons for plasma-based space electric propulsion," *Physics of Plasmas*, vol. 27, 2 Feb. 2020, ISSN: 10897674. DOI: 10.1063/1.5109141.

[15] D. M. Goebel and I. Katz, *Fundamentals of Electric Propulsion: Ion and Hall Thrusters*, I. J. W. Sons, Ed. John Wiley & Sons, Inc., Oct. 2008, pp. 1–507, ISBN: 9780470436448. DOI: 10.1002/9780470436448. [Online]. Available: http://doi.wiley.com/10.1002/9780470436448.

[16] M. Manente, F. Trezzolani, R. Mantellato, *et al.*, “Regulus: Iodine fed plasma propulsion system for small satellites,” in *The 36th International Electric Propulsion Conference IEPC-2019-417*, 2019.

[17] F. Cannat, T. Lafleur, J. Jarrige, P. Chabert, P. Q. Elias, and D. Packan, “Optimization of a coaxial electron cyclotron resonance plasma thruster with an analytical model,” *Physics of Plasmas*, vol. 22, 5 May 2015, ISSN: 10897674. DOI: 10.1063/1.4920966.

[18] M. D. West, C. Charles, and R. W. Boswell, “Testing a helicon double layer thruster immersed in a space-simulation chamber,” *Journal of Propulsion and Power*, vol. 24, no. 1, pp. 134–141, 2008.

[19] D. Pavarin, F. Ferri, M. Manente, *et al.*, “Helicon plasma hydrazine combined micro project overview and development status,” in *Proceedings of the 2nd Space Propulsion Conference SP2010-1842379*, San Sebastian, E, 2010.

[20] F. Trezzolani, M. Manente, A. Selmo, *et al.*, “Development and test of an high power rf plasma thruster in project sapere-strong,” in *The 35th International Electric Propulsion Conference IEPC-2017-462*, Atlanta, GA, USA, 2017.

[21] M. Manente, F. Trezzolani, M. Magarotto, *et al.*, “Regulus: A propulsion platform to boost small satellite missions,” *Acta Astronautica*, vol. 157, pp. 241–249, Apr. 2019, ISSN: 00945765. DOI: 10.1016/j.actaastro.2018.12.022. [Online]. Available: https://linkinghub.elsevier.com/retrieve/pii/S0094576518310488.

[22] *T4i - Technology for propulsion and innovation official*, https://www.t4innovation.com/.

[23] F. R. C. Díaz, “The vasimr rocket,” *Scientific American*, vol. 283, pp. 90–97, 5 Nov. 2000, ISSN: 0036-8733. DOI: 10.1038/scientificamerican1100-90. [Online]. Available: http://www.nature.com/doifinder/10.1038/scientificamerican1100-90.

[24] A. V. Arefiev and B. N. Breizman, “Theoretical components of the vasimr plasma propulsion concept,” vol. 11, May 2004, pp. 2942–2949. DOI: 10.1063/1.1666328.

[25] M. Ruiz, V Gomez, P Fajardo, *et al.*, “Hipatia: A project for the development of the helicon plasma thruster and its associated technologies to intermediate-high trls,” in *71st International Astronautical Congress (IAC)*, Washington, DC, USA, 2020.

[26] M. Ruiz, V Gómez, P Fajardo, *et al.*, “Hipatia: A project for the development of the helicon plasma thruster and its associated technologies to intermediate-high trls,” 2020.

[27] F. Romano, Y.-A. Chan, G. Herdrich, *et al.*, “Rf helicon-based inductive plasma thruster (ipt) design for an atmosphere-breathing electric propulsion system (abep),” *Acta Astronautica*, vol. 176, pp. 476–483, 2020.

[28] K. Takahashi, “Magnetic nozzle radiofrequency plasma thruster approaching twenty percent thruster efficiency,” *Scientific reports*, vol. 11, no. 1, pp. 1–12, 2021.

[29] O. V. Batishchev, “Minihelicon plasma thruster,” *IEEE Transactions on plasma science*, vol. 37, no. 8, pp. 1563–1571, 2009.

[30] J. Sheehan, T. A. Collard, F. H. Ebersohn, and B. W. Longmier, “Initial operation of the cubesat ambipolar thruster,” in *34th International Electric Propulsion Conference, IEPC-2015-243*, Hyogo-Kobe,J, 2015.

[31] R Winglee, T Ziemba, L Giersch, J Prager, J Carscadden, and B. Roberson, “Simulation and laboratory validation of magnetic nozzle effects for the high power helicon thruster,” *Physics of Plasmas*, vol. 14, no. 6, p. 063 501, 2007.

[32] S. Andrews, R. Andriulli, N. Souhair, *et al.*, “Coupled global and pic modelling of the regulus cathode-less plasma thrusters operating on xenon, iodine and krypton,” *Acta Astronautica*, Jun. 2023, ISSN: 00945765. DOI: 10.1016/j.actaastro.2023.03.015.

[33] N. Souhair, M. Magarotto, R. Andriulli, and F. Ponti, “Prediction of the propulsive performance of an atmosphere-breathing electric propulsion system on cathode-less plasma thruster,” *Aerospace*, vol. 10, p. 100, 2 Jan. 2023, ISSN: 2226-4310. DOI: 10.3390/aerospace10020100. [Online]. Available: https://www.mdpi.com/2226-4310/10/2/100.

[34] G Gallina, M Magarotto, M Manente, and D. Pavarin, “Enhanced bidimensional pic: An electrostatic/magnetostatic particle-in-cell code for plasma based systems,” *Journal of Plasma Physics*, vol. 85, no. 2, 2019.

[35] M. Magarotto, S. Di Fede, N. Souhair, S. Andrews, and F. Ponti, “Numerical suite for cathodeless plasma thrusters,” *Acta Astronautica*, vol. 197, pp. 126–138, 2022, ISSN: 0094-5765. DOI: https://doi.org/10.1016/j.actaastro.2022.05.018. [Online]. Available: https://www.sciencedirect.com/science/article/pii/S0094576522002144.

[36] M. Martinez-Sanchez, J. Navarro-Cavallé, and E. Ahedo, “Electron cooling and finite potential drop in a magnetized plasma expansion,” *Physics of Plasmas*, vol. 22, 5 May 2015, ISSN: 10897674. DOI: 10.1063/1.4919627.

[37] M. Guaita, M. Magarotto, M. Manente, D. Pavarin, and M. Lavagna, “Semi-analytical model of a Helicon plasma thruster,” *IEEE Transactions on Plasma Science*, vol. 50, no. 2, pp. 425–438, 2022.

[38] W. van Lynden, “A review of coupling techniques for the modelling of helicon plasma thrusters,” Unpublished Literature Study, 2022.

[39] S. Correyero, J. Jarrige, D. Packan, and E. Ahedo, “Plasma beam characterization along the magnetic nozzle of an ecr thruster,” *Plasma Sources Science and Technology*, vol. 28, p. 095 004, 9 Sep. 2019, ISSN: 0963-0252. DOI: 10.1088/1361-6595/AB38E1. [Online]. Available: https://iopscience-iop-org.tudelft.idm.oclc.org/article/10.1088/1361-6595/ab38e1https://iopscience-iop-org.tudelft.idm.oclc.org/article/10.1088/1361-6595/ab38e1/meta.

[40] J Zhou, A Domínguez-Vázquez, P Fajardo, and E Ahedo, “Magnetized fluid electron model within a two-dimensional hybrid simulation code for electrodeless plasma thrusters,” *Plasma Sources Science and Technology*, vol. 31, p. 16, 2022. DOI: 10.1088/1361-6595/ac64bc. [Online]. Available: https://doi.org/10.1088/1361-6595/ac64bc.

[41] N. Singh, “Current-free double layers: A review,” *Phys. Plasmas*, vol. 18, p. 122 105, 2011. DOI: 10.1063/1.3664321. [Online]. Available: https://doi.org/10.1063/1.3664321.

[42] P. Jiménez, M. Merino, and E. Ahedo, “Wave propagation and absorption in a helicon plasma thruster and its plume,” *Plasma Sources Science and Technology*, vol. 31, p. 045 009, 4 Apr. 2022, ISSN: 0963-0252. DOI: 10.1088/1361-6595/AC5ECD. [Online]. Available: https://iopscience-iop-org.tudelft.idm.oclc.org/article/10.1088/1361-6595/ac5ecdhttps://iopscience-iop-org.tudelft.idm.oclc.org/article/10.1088/1361-6595/ac5ecd/meta.

[43] J. A. Bittencourt, *Fundamentals of Plasma Physics*. Springer New York, 2004, ISBN: 978-1-4419-1930-4. DOI: 10.1007/978-1-4757-4030-1. [Online]. Available: http://link.springer.com/10.1007/978-1-4757-4030-1.

[44] F. F. Chen, *Introduction to Plasma Physics and Controlled Fusion*. Springer International Publishing, 2016, ISBN: 978-3-319-22308-7. DOI: 10.1007/978-3-319-22309-4. [Online]. Available: http://link.springer.com/10.1007/978-3-319-22309-4.

[45] M. A. Lieberman and A. J. Lichtenberg, *PRINCIPLES OF PLASMA DISCHARGES AND MATERIALS PROCESSING*, 2nd ed. Wiley-Interscience, 2005, pp. 43–82.

[46] F. F. Chen, “Helicon discharges and sources: A review,” *Plasma Sources Science and Technology*, vol. 24, no. 1, p. 014 001, Jan. 2015. DOI: 10.1088/0963-0252/24/1/014001. [Online]. Available: https://doi.org/10.1088/0963-0252/24/1/014001.

[47] A. R. Choudhuri, *The Physics of Fluids and Plasmas*. Cambridge University Press, 1998, ISBN: 9780521555432. DOI: 10.1017/CBO9781139171069. [Online]. Available: https://www.cambridge.org/core/product/identifier/9781139171069/type/book.

[48] X.-M. Zhu and Y.-K. Pu, “A simple collisional–radiative model for low-temperature argon discharges with pressure ranging from 1 Pa to atmospheric pressure: kinetics of Paschen 1s and 2p levels,” *Journal of Physics D: Applied Physics*, vol. 43, no. 1, p. 015 204, Jan. 2010, ISSN: 0022-3727. DOI: 10.1088/0022-3727/43/1/015204. [Online]. Available: https://iopscience.iop.org/article/10.1088/0022-3727/43/1/015204.

[49] N. Souhair, M. Magarotto, E. Majorana, F. Ponti, and D. Pavarin, “Development of a lumping methodology for the analysis of the excited states in plasma discharges operated with argon, neon, krypton, and xenon,” *Physics of Plasmas*, vol. 28, 9 Sep. 2021, ISSN: 10897674. DOI: 10.1063/5.0057494.

[50] B. N. Wachs and B. A. Jorns, “Optimization of an ecr thruster using single, two frequency, and pulsed waveforms,” American Institute of Aeronautics and Astronautics Inc, AIAA, 2021, ISBN: 9781624106118. DOI: 10.2514/6.2021-3382.

[51] N. Souhair, F. Ponti, M. Magarotto, and D. Pavarin, “Analysis of different numerical approaches for the simulation of a helicon plasma thruster,” in *Proceedings of the 37th International Electric Propulsion Conference (IEPC)*, 2022. [Online]. Available: https://www.researchgate.net/publication/361585984.

[52] E. Ahedo and J. Navarro-Cavallé, “Helicon thruster plasma modeling: Two-dimensional fluid-dynamics and propulsive performances,” *Physics of Plasmas*, vol. 20, 4 Apr. 2013, ISSN: 1070664X. DOI: 10.1063/1.4798409.

[53] M. A. Lieberman and A. J. Lichtenberg, *Principles of Plasma Discharges and Materials Processing*, II, Wiley, Ed. Wiley, 2005. [Online]. Available: https://books.google.it/books?hl=it&lr=&id=m0iOga2XE5wC&oi=fnd&pg=PR5&dq=M.+A.+Lieberman,+A.+J.+Lichtenberg,+Principles+of+plasma+discharges+and+materials+processing,+II+edition,+Wiley,+(2005)&ots=Hmb6G7G7bL&sig=89CyIIZ0YXaoZcyi-Sx-9XewsI8#v=onepage&q=M..

[54] M Magarotto, D Melazzi, and D Pavarin, “Study on the influence of the magnetic field geometry on the power deposition in a helicon plasma source,” *J. Plasma Phys*, vol. 85, 2019. DOI: 10.1017/S0022377819000473. [Online]. Available: https://doi.org/10.1017/S0022377819000473.

[55] E. Ahedo and M. Merino, “Two-dimensional supersonic plasma acceleration in a magnetic nozzle,” *Phys. Plasmas*, vol. 17, p. 73 501, 2010. DOI: 10.1063/1.3442736. [Online]. Available: https://doi.org/10.1063/1.3442736.

[56] A Fruchtman, “Electric field in a double layer and the imparted momentum,” 2006. DOI: 10.1103/PhysRevLett.96.065002.

[57] T. Lafleur, “Helicon plasma thruster discharge model,” *Physics of Plasmas*, vol. 21, 4 2014, ISSN: 10897674. DOI: 10.1063/1.4871727.

[58] M. Manente and M. Magarotto, “Electric propulsion systems,” in *Next Generation CubeSats and SmallSats*, Elsevier, 2023, ch. 20, pp. 485–517.

[59] A. J. Sheppard and J. M. Little, “Performance analysis of an electron cyclotron resonance thruster with various propellants,” *Journal of Propulsion and Power*, vol. 38, pp. 998–1008, 6 Nov. 2022, ISSN: 15333876. DOI: 10.2514/1.B38698.

[60] C Charles, R. W. Boswell, R Laine, and P Maclellan, “An experimental investigation of alternative propellants for the helicon double layer thruster,” *Journal of Physics D: Applied Physics J. Phys. D: Appl. Phys*, vol. 41, p. 6, 2008. DOI: 10.1088/0022-3727/41/17/175213.

[61] A. Fruchtman, “Neutral depletion in a collisionless plasma,” *IEEE TRANSACTIONS ON PLASMA SCIENCE*, vol. 36, p. 403, 2 2008. DOI: 10.1109/TPS.2008.918777.

[62] K. Takahashi, “Magnetic nozzle radiofrequency plasma thruster approaching twenty percent thruster efficiency,” *Scientific Reports* |, vol. 11, p. 2768, 2021. DOI: 10.1038/s41598-021-82471-2. [Online]. Available: https://doi.org/10.1038/s41598-021-82471-2.

[63] F. Ebersohn, L. Raja, and J. Shebalin, “Resistive magnetohydrodynamic study of magnetic field effects on plasma plumes,” Jun. 2013. DOI: 10.2514/6.2013-2759.

[64] M. D. West, C. Charles, and R. W. Boswell, “Mode transitions in the helicon double-layer thruster prototype operating in xenon,” *IEEE TRANSACTIONS ON PLASMA SCIENCE*, vol. 39, 11 2011. DOI: 10.1109/TPS.2011.2158589.

[65] J Ling, J. Zhu, C Rea, *et al.*, “Thrust measurements in a low-magnetic field mode in the hdlt,” *Journal of Physics D: Applied*, vol. 43, p. 9, 2010. DOI: 10.1088/0022-3727/43/30/305203.

[66] P. Dietz, W. Gärtner, Q. Koch, *et al.*, "Molecular propellants for ion thrusters," *Plasma Sources Science and Technology*, vol. 28, no. 8, p. 084 001, Aug. 2019. DOI: 10.1088/1361-6595/ab2c6c. [Online]. Available: https://dx.doi.org/10.1088/1361-6595/ab2c6c.

[67] F. Diop, T. Gibert, and A. Bouchoule, "Argon ionization improvement in a plasma thruster induced by few percent of xenon," *Physics of Plasmas*, vol. 26, 6 Jun. 2019, ISSN: 10897674. DOI: 10.1063/1.5082904.

[68] J. Yamasaki, S. Yokota, and K. Shimamura, "Performance enhancement of an argon-based propellant in a hall thruster," *Vacuum*, vol. 167, pp. 520–523, Sep. 2019, ISSN: 0042-207X. DOI: 10.1016/J.VACUUM.2018.09.042.

[69] M. R. LaPointe, E. Strzempkowski, and E. Pencil, "High power mpd thruster performance measurements," *40th AIAA/ASME/SAE/ASEE Joint Propulsion Conference and Exhibit*, 2004, ISSN: 2004-3467. DOI: 10.2514/6.2004-3467. [Online]. Available: https://arc-aiaa-org.tudelft.idm.oclc.org/doi/10.2514/6.2004-3467.

[70] E. Y. Choueir and J. K. Ziemer, "Quasi-steady manetoplasmadynamic thruster measured performance database," *34th AIAA/ASME/SAE/ASEE Joint Propulsion Conference and Exhibit*, 1998. DOI: 10.2514/6.1998-3472. [Online]. Available: https://arc-aiaa-org.tudelft.idm.oclc.org/doi/10.2514/6.1998-3472.

[71] L. Cassady, B. Longmier, C. Olsen, *et al.*, "Vasimr performance results," American Institute of Aeronautics and Astronautics (AIAA), Jul. 2010. DOI: 10.2514/6.2010-6772.

[72] A Crestetto, F Deluzet, and D Doyen, "Bridging kinetic plasma descriptions and single-fluid models," *J. Plasma Phys*, vol. 86, p. 825 860 501, 2020. DOI: 10.1017/S0022377820000884. [Online]. Available: https://doi.org/10.1017/S0022377820000884.

[73] L. Brieda and M. Keidar, "Development of the starfish plasma simulation code and update on multiscale modeling of hall thrusters," in *48th AIAA/ASME/SAE/ASEE Joint Propulsion Conference & Exhibit*, American Institute of Aeronautics and Astronautics Inc., 2012, ISBN: 9781600869358. DOI: 10.2514/6.2012-4015.

[74] M. Guaita, M. Magarotto, and M. Manente, "Politecnico di milano semi-analytical mono-dimensional modelling of cathodeless plasma thrusters school of industial and information engineering department of aerospace science and technology msc in space engineering supervisor: Prof. michèle lavagna coadvisors," 2019.

[75] M. Magarotto, D. Melazzi, and D. Pavarin, "3d-virtus: Equilibrium condition solver of radio-frequency magnetized plasma discharges for space applications," *Computer Physics Communications*, vol. 247, Feb. 2020, ISSN: 00104655. DOI: 10.1016/j.cpc.2019.106953.

[76] D. Melazzi and V. Lancellotti, "Adamant: A surface and volume integral-equation solver for the analysis and design of helicon plasma sources," *Computer Physics Communications*, vol. 185, pp. 1914–1925, 7 Jul. 2014, ISSN: 00104655. DOI: 10.1016/j.cpc.2014.03.019. [Online]. Available: https://linkinghub.elsevier.com/retrieve/pii/S001046551400099X.

[77] M. Magarotto and D. Pavarin, "Parametric study of a cathode-less radio frequency thruster," *IEEE Transactions on Plasma Science*, vol. 48, no. 8, pp. 2723–2735, 2020.

[78] "Openfoam." (), [Online]. Available: https://www.openfoam.com/.

[79] P. I. C. C. LLC. (), [Online]. Available: https://www.particleincell.com/.

[80] F. F. Chen, "Physical mechanism of current-free double layers," *Phys. Plasmas*, vol. 13, p. 34 502, 2006. DOI: 10.1063/1.2179393. [Online]. Available: https://doi.org/10.1063/1.2179393.

[81] T. A. Collard and B. A. Jorns, "Magnetic nozzle efficiency in a low power inductive plasma source.," *Plasma Sources Sci. Technol.*, vol. 28, 10 2019. DOI: 10.1088/1361-6595/ab2d7d. [Online]. Available: https://doi.org/10.1088/1361-6595/ab2d7d.

[82] G. Dimarco, L. Mieussens, and V. Rispoli, "An asymptotic preserving automatic domain decomposition method for the vlasov–poisson–bgk system with applications to plasmas," *Journal of Computational Physics*, vol. 274, pp. 122–139, Oct. 2014, ISSN: 0021-9991. DOI: 10.1016/J.JCP.2014.06.002.

[83] M. Magarotto, D. Melazzi, and D. Pavarin, "3D-VIRTUS: Equilibrium condition solver of radio-frequency magnetized plasma discharges for space applications," *Computer Physics Communications*, vol. 247, p. 106 953, Feb. 2020, ISSN: 00104655. DOI: 10.1016/j.cpc.2019.106953. [Online]. Available: https://linkinghub.elsevier.com/retrieve/pii/S001046551930308X.

[84] I. G. Mikellides, I. Katz, D. M. Goebel, and J. E. Polk, "Hollow cathode theory and experiment. II. A two-dimensional theoretical model of the emitter region," *Journal of Applied Physics*, vol. 98, no. 11, p. 113 303, Dec. 2005, ISSN: 0021-8979. DOI: 10.1063/1.2135409. [Online]. Available: http://aip.scitation.org/doi/10.1063/1.2135409.

[85] G. J. M. Hagelaar, F. J. de Hoog, and G. M. W. Kroesen, "Boundary conditions in fluid models of gas discharges," *Physical Review E*, vol. 62, no. 1, pp. 1452–1454, Jul. 2000, ISSN: 1063-651X. DOI: 10.1103/PhysRevE.62.1452. [Online]. Available: https://link.aps.org/doi/10.1103/PhysRevE.62.1452.

[86] S. Di Fede, M. Magarotto, S. Andrews, and D. Pavarin, "Simulation of the plume of a magnetically enhanced plasma thruster with SPIS," *Journal of Plasma Physics*, vol. 87, no. 6, p. 905 870 611, 2021.

[87] I. D. Boyd, *Predicting breakdown of the continuum equations under rarefied flow conditions*, 2003.

[88] "Mupets, the multi-regime plasma equilibrium transport solver." (), [Online]. Available: https://github.com/willemvl/MUPETS.git.

[89] T. Lafleur, "Helicon plasma thruster discharge model," *Physics of Plasmas*, vol. 21, no. 4, p. 043 507, 2014.

[90] F. Trezzolani, M. Magarotto, M. Manente, and D. Pavarin, "Development of a counterbalanced pendulum thrust stand for electric propulsion," *Measurement*, vol. 122, pp. 494–501, Jul. 2018, ISSN: 02632241. DOI: 10.1016/j.measurement.2018.02.011. [Online]. Available: https://linkinghub.elsevier.com/retrieve/pii/S0263224118300988.

[91] N. Bellomo, M. Manente, F. Trezzolani, *et al.*, "Enhancement of microsatellites' mission capabilities: Integration of regulus electric propulsion module into unisat-7," in *Proceedings of the 70th International Astronautical Congress (IAC)*, 2019.

[92] M. A. Khakoo, P Vandeventer, J. G. Childers, *et al.*, "Electron impact excitation of the argon 3p54s configuration: Differential cross-sections and cross-section ratios," *Journal of Physics B: Atomic, Molecular and Optical Physics*, vol. 37, no. 1, pp. 247–281, Dec. 2003. DOI: 10.1088/0953-4075/37/1/016. [Online]. Available: https://doi.org/10.1088/0953-4075/37/1/016.

[93] L. L. Alves, K Bartschat, S. F. Biagi, *et al.*, "Comparisons of sets of electron–neutral scattering cross sections and swarm parameters in noble gases: II. Helium and neon," *Journal of Physics D: Applied Physics*, vol. 46, no. 33, p. 334 002, Aug. 2013, ISSN: 0022-3727. DOI: 10.1088/0022-3727/46/33/334002. [Online]. Available: https://iopscience.iop.org/article/10.1088/0022-3727/46/33/334002.

[94] NGFSRDW Database. Available online: https://www.lxcat.net/NGFSRDW (Accessed on 1 January 2021). ().

[95] HAYASHI Database. Available online: https://www.lxcat.net/Hayashi (Accessed on 1 January 2021). ().

[96] H. A. Hyman, "Electron-impact ionization cross sections for excited states of the rare gases (ne, ar, kr, xe), cadmium, and mercury," *Phys. Rev. A*, vol. 20, pp. 855–859, 3 Sep. 1979. DOI: 10.1103/PhysRevA.20.855. [Online]. Available: https://link.aps.org/doi/10.1103/PhysRevA.20.855.

[97] M. Allan, O. Zatsarinny, and K. Bartschat, "Near-threshold absolute angle-differential cross sections for electron-impact excitation of argon and xenon," *Phys. Rev. A*, vol. 74, p. 030 701, 3 Sep. 2006. DOI: 10.1103/PhysRevA.74.030701. [Online]. Available: https://link.aps.org/doi/10.1103/PhysRevA.74.030701.

[98] PHELPS Database. Available online: https://www.lxcat.net/Phelps (Accessed on 1 January 2021). ().

[99] T. J. Sommerer, “Model of a weakly ionized, low-pressure xenon dc positive column discharge plasma,” *Journal of Physics D: Applied Physics*, vol. 29, no. 3, pp. 769–778, Mar. 1996, ISSN: 0022-3727. DOI: 10.1088/0022-3727/29/3/038. [Online]. Available: https://iopscience.iop.org/article/10.1088/0022-3727/29/3/038.

[100] BIAGI v7 Database. Available online: https://www.lxcat.net/Biagi-v7.1 (Accessed on 1 January 2021). ().

[101] COP Database. Available online: https://www.lxcat.net/COP (Accessed on 1 January 2021). ().

[102] Priti, R. K. Gangwar, and R Srivastava, “Collisional-radiative model of xenon plasma with calculated electron-impact fine-structure excitation cross-sections,” *Plasma Sources Science and Technology*, vol. 28, no. 2, p. 025 003, Feb. 2019, ISSN: 1361-6595. DOI: 10.1088/1361-6595/aaf95f. [Online]. Available: https://iopscience.iop.org/article/10.1088/1361-6595/aaf95f.

[103] J. Zhou, A. Domínguez-Vázquez, P. Fajardo, and E. Ahedo, “Magnetized fluid electron model within a two-dimensional hybrid simulation code for electrodeless plasma thrusters,” *Plasma Sources Science and Technology*, 2022.

[104] N. Bellomo, M. Magarotto, M. Manente, *et al.*, “Regulus: Integration and testing of an iodine electric propulsion system,” in *Space Propulsion Conference*, Estoril, Portugal, 2020.

[105] M. U. Siddiqui, C. Cretel, J. Synowiec, A. G. Hsu, J. A. Young, and R. Spektor, *First performance measurements of the phase four rf thruster*, 2017.

[106] L. T. Williams and M. L. Walker, “Thrust measurements of a radio frequency plasma source,” *Journal of Propulsion and Power*, vol. 29, pp. 520–527, 3 2013, ISSN: 15333876. DOI: 10.2514/1.B34574.

[107] T. Lafleur, C. Charles, and R. Boswell, “Plasma control by modification of helicon wave propagation in low magnetic fields,” *Physics of Plasmas*, vol. 17, pp. 073 508–073 508, Jul. 2010. DOI: 10.1063/1.3460351.

A

Other Simulation Cases

A.0.1. Verification Case 3: Complex B field in source for stress-testing (Cusped)

The purpose of the Cusped case, is to stress-test the model, verifying that it can handle complex and sharply angled magnetic field topologies consisting of multiple cusps. As with the Coiled case, the Cusped case, is tested only for Step 0 due to time considerations, to keep the experiment duration within one week. It is expected that the plasma will diffuse towards the walls through these cusps, thus further increasing plasma losses to the walls as compared to Coiled case. Looking at the results shown in figures A.1a and A.2a, it is seen that the maximum plasma density reached in the source is indeed lower than Case 2, and that there is indeed a concentration of plasma diffusing to the wall at the cusp in the magnetic field. Looking at the plume however, a large discontinuity is present. This occurred due to an error in the setup of the kinetic case, causing the solution not to converge before completion. The amount of sub-iterations to be ran for the kinetic model was previously a set, hard-coded, quantity in the solver setup which had to be manually calculated and updated. The calculation is based on the time required for the slowest macro-particle to reach the end of the numerical domain and travel back, which should, in general, account for all paths of motion a macro particle can be expected to make. During this simulation case, the amount of sub-iterations was kept too low, and therefore by the end of these iterations the solution had not yet converged. After this mistake was found, this was mitigated through performing the required calculation automatically in MUPETS. However, by that time, it was deemed more important to start with the validation of the model rather than testing this edge-case further, as the magnetic field is not representative of that normally found in an APT. In the future, this case should be run again to further stress test the entire coupled model and enable it's wider application to non-standard magnetic fields.

A.0.2. Additional Validation: piglet reactor

As the validation with comparison to experimental thrust values depends on the thrust, which itself is a derived value in the model, it is also interesting to directly compare the driving variables of the model, such as the plasma densities or the VDFs. The field of plasma diagnostics is, however, extremely challenging due to the difficulty of placing probes in the extremely hot and charged plasma without negatively affecting the probes or disturbing the flow. This is especially difficult for the high density, high temperature plasma inside the small source chamber. Hence, reliable data-sets for relevant ambipolar thrusters are scarce, especially when considering the properties in the source chamber. To aid the validation, the solver can be used instead to model a different plasma system for which an accurately measured data-set does exists. The plasma system considered is a piglet helicon reactor, an enclosed laboratory plasma reactor designed to create the helicon wave for high density plasma creation and diagnostics. The validation currently concerns only the fluid module of MUPETS, rather than the entire coupled model. Preliminary attempts at setting up the kinetic numerical domain inside the reactor presented challenges with the boundaries, resulting in an unrealistic amount of plasma loss. Modeling the reactor with the entire coupled model is therefore left for future work.

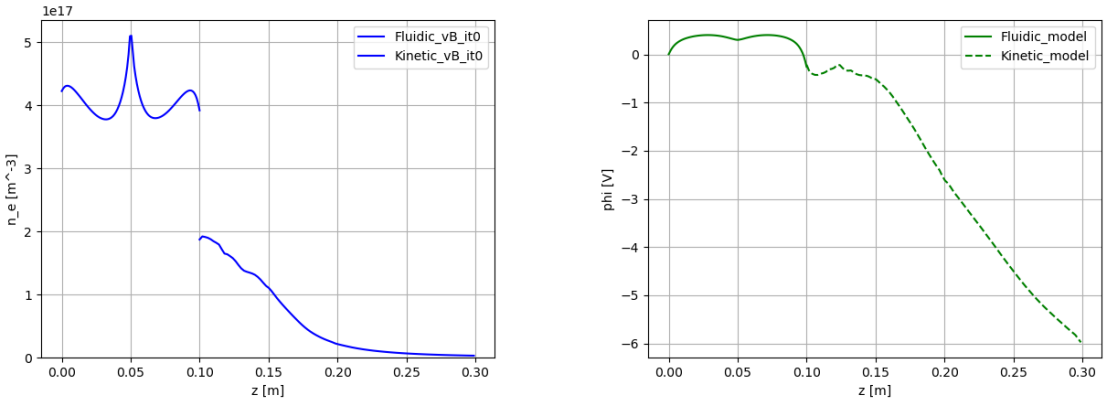

(a) Electron density n_e

(b) Plasma potential ϕ

Figure A.1: Case 3: Complex magnetic field applied. Area-averaged plasma property profiles along the axial thruster length z

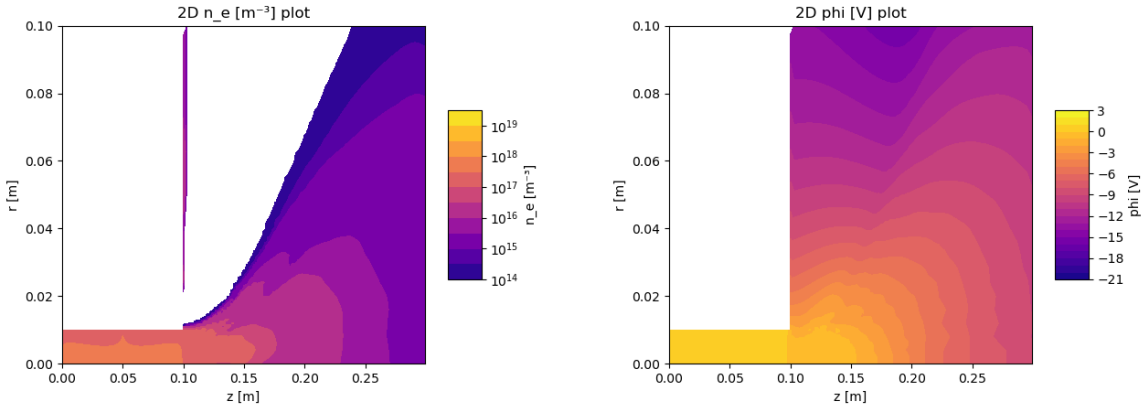

(a) Electron density n_e

(b) Plasma potential ϕ

Figure A.2: Case 3: Complex magnetic field applied. Plasma properties on the full 2D $z-r$ thruster domain. z and r are the thruster domain's axial and radial length respectively.

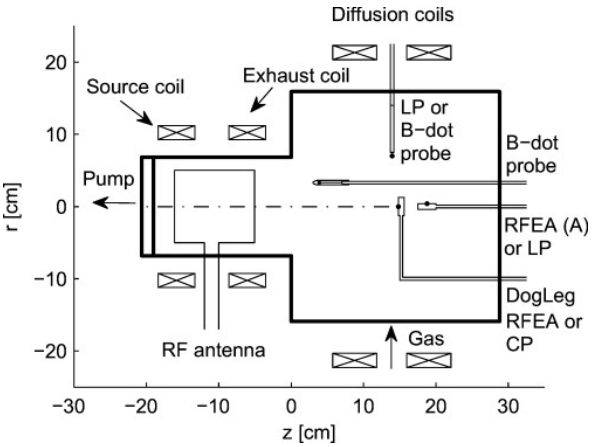

(a) The Piglet helicon reactor, showing the source region (z < $0\,\mathrm{cm}$), diffusion chamber (z > $0\,\mathrm{cm}$), magnetic field coils, and experimental probes. Taken from Lafleur(2010)[107]

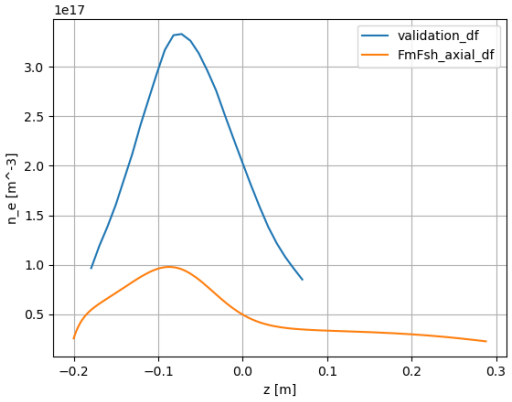

(b) The modeled area-averaged electron density n_e profile along the reactor's axial z axis along with the experimentally obtained values[107]. The predicted values extend to the diffusion chamber.

Figure A.3: The piglet reactor and the comparison between measured and predicted electron densities

Reactor setup

The model setup follows the experimental setup of the reactor itself[107]. A magneto-static field of $2.1\,\mathrm{mT}$ is applied and $250\,\mathrm{W}$ of RF power is induced into the plasma. An important difference between the real reactor and the model is the placement of the pump, taken as the outlet, and the gas inlet. For the coupled thruster model, these are swapped in place, to model the flow as if it were inside a thruster. It is believed that this helps with the convergence of the fluid solver. The piglet reactor setup, with in red and blue the modeled locations of the inlet and outlet respectively, is shown in figure A.3a

Results and comparison

The fluid solver results and the experimental results for the piglet reactor are shown in figure A.3b. Although the general shape is in agreement, the model vastly underestimates the electron density inside the source region. One suspected reason for this is the simplified transport model in the fluid solver, resulting from implementing of the Drift Diffusion assumption instead of modeling the full momentum of all species. Another possible cause is the altered geometry of the modeled reactor, caused by the swapping of the inlet and outlet locations. Besides modeling the full reactor with the full coupled MUPETS code, future work should also include more faithful modeling of the reactor with an improved fluid model, which will account for the full momentum equation.

B

OpenFOAM Variable Field Values

Below is OpenFOAM's volume scalar field dictionary used as input to initialize the plasma potential, denoted in the code as phi instead of ϕ. It contains, besides OpenFOAM specific information, the dimensions of the potential, the initial value for the internal field (set uniform here for all volume cell centers except the surface centers at the domain's boundaries) and the boundary conditions for each defined boundary. Note that these values can be non-uniform as well, in which case they should be defined for each and every volume or surface center, or para-metrically and dependent on other OpenFOAM field values, as is done for the outlet. Regardless, for the first sub-iteration of the OpenFOAM code, the outlet is still initialized with a uniform value.

```
/*--------------------------------*- C++ -*----------------------------------*\
| =========                 |                                                 |
| \\      /  F ield         | OpenFOAM: The Open Source CFD Toolbox           |
|  \\    /   O peration     | Version:  plus                                  |
|   \\  /    A nd           | Web:      www.OpenFOAM.com                      |
|    \\/     M anipulation  |                                                 |
\*---------------------------------------------------------------------------*/
FoamFile
{
    version     2.0;
    format      ascii;
    class       volScalarField;
    object      phi;
}
// * * * * * * * * * * * * * * * * * * * * * * * * * * * * * * * * * * * * * //

dimensions      [1 2 -3 0 0 -1 0];

internalField   uniform 0.0;

boundaryField
{
    walls
    {
        type            fixedValue;
        value           uniform 0.0;
    }

    inlet
    {
        type            fixedValue;
        value           uniform 0.0;
    }

    outlet
    {
        type            groovyBC;
        gradientExpression "gradFakeAlter";
        fractionExpression "0";
```

```
        variables       (
                        "M_ion=2.180e-25;"
                        "q=1.60218e-19;"
                        "T0=300.0;"
                        "N_A=6.022e+23;"
                        "R=8.314472;"
                        "A_cyl=pi*1e-4;"
                        "v_th=sqrt(8*R*T0/(pi*M_ion*N_A));"
                        "Flux_i=(mui*(E&normal())+0.5*v_th)*ni;"
                        "Flux_e=(ne*u_e)&normal();"
                        "gradFake=(0.5*v_th*ni-Flux_e)/(ni*mui);"
                        "gradFakeAlter=-(Flux_e+(Di*grad_rho_i&normal()/q))/(ni*mui);"
                        );
        value           uniform 0.0;
    }

    #include "include/frontAndBackPatches"
}

// ************************************************************************* //
```

The next lines are the first lines of the plasma potential's output file after steady-state convergence. Now, each cell of the 25000 mesh cells of the internal field has it's own center value, after which the boundary conditions which are not set to uniform fixed values also report each boundary surface's value. The selection is limited to the first lines for the sake of brevity, the total file has 25197 lines.

```
/*--------------------------------*- C++ -*----------------------------------*\
| =========                 |                                                 |
| \\      /  F ield         | OpenFOAM: The Open Source CFD Toolbox           |
|  \\    /   O peration     | Version:  2006                                  |
|   \\  /    A nd           | Website:  www.openfoam.com                      |
|    \\/     M anipulation  |                                                 |
\*---------------------------------------------------------------------------*/
FoamFile
{
    version     2.0;
    format      ascii;
    class       volScalarField;
    location    "3.6175e-05";
    object      phi;
}
// * * * * * * * * * * * * * * * * * * * * * * * * * * * * * * * * * * * * * //

dimensions      [1 2 -3 0 0 -1 0];


internalField   nonuniform List<scalar>
25000
(
0.004681252901530055
0.004681394778656467
0.004681706384032572
0.004682177737441171
0.004682804740075279
0.004683583176481657
0.004684507983811809
0.004685572981362399
0.004686770647400929
0.00468809190942674
0.00468952581767052
0.004691059281251691
0.00469267663718357
0.004694359082716995
0.004696084060476634
0.004697824503148713
0.004699547816922554
0.004701214623494916
0.004702777360541897
0.004704178467704457
```